First principles calculations of the properties of earth-metal oxides

Whitehead, Eric Jonathan

Award date:
1993

Awarding institution:
University of Bath

FIRST PRINCIPLES CALCULATIONS OF THE PROPERTIES OF EARTH-METAL OXIDES

Submitted by Eric Jonathan Whitehead
for the degree of
Doctor of Philosophy
of the University of Bath
1993

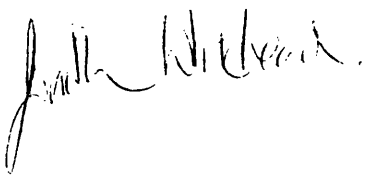

ProQuest LLC
789 East Eisenhower Parkway
P.O. Box 1346
Ann Arbor, MI 48106-1346

ABSTRACT

This thesis is concerned with the calculation of the physical properties of earth-metal oxides. The method chosen to achieve this is a pseudopotential one with a plane wave basis. The only inherent approximation used is that of the Local Density Approximation (LDA) and it is reckoned that this is the most accurate technique available for solid state calculations. To improve the computational efficiency the calculations are made on the large parallel surface at Edinburgh as part of the *Grand Challenge* collaboration.

The equilibrium properties of MgO are the first testing grounds for these calculations. Comparison with the results obtained by other techniques are used to judge the effectiveness of the pseudopotential method. Calculations are then made to establish the behaviour of MgO at high pressure and to investigate its electronic structure. Finally these results are extended to include similar calculations of the properties of other earth-metal oxides.

ACKNOWLEDGEMENTS

There are many people who contributed in large or small ways to the work presented in this thesis. I would like to thank Ivan Štich, Lyndon Clarke, Mike Payne and all the other members of the Grand Challenge collaboration who were responsible for the coding of CETEP. I am also indebted to N Troullier, J L Martins and J S Lin for providing optimised oxygen pseudopotentials and Steve Parker and Alison Wall of the School of Chemistry without whom much of the geophysical work would have been impossible. Thanks are also due to Paul Dale and Martin Saunders with whom I have spent three enjoyable years in the solid state theory group; to David Ladds for sundry computational jiggery-pokery; and to all the members of the School of Physics at the University of Bath.

Most of all, however, I would like to take this opportunity to thank David Bird who has supervised my research project. His patience in explanation and enthusiasm for the subject have been instrumental in the success of this work. David has also spent a great deal of time reading through the first drafts of this thesis for which I am also extremely grateful.

I should also like to thank the School of Physics and the University for the use of computing and other facilities. Finally I would like to thank SERC for their meagre stipend which has kept me on the bread-line for the last three years.

Contents

Chapter 1

INTRODUCTION

The purpose of this thesis is to make first principles calculations of the physical properties of earth-metal oxides using a quantum mechanical method. Although there are a large number of techniques that could be employed for this task it is a pseudopotential one based on the method of Car and Parrinello (1985) that will be used. This method has been modified and enhanced many times over the last few years. The most recent development has been the parallelisation of the code to enable it to utilise the large computing surfaces that are now available. At the present time it is reckoned to be the most efficient and probably the most accurate technique for simulating the behaviour of condensed matter. There are broadly three motives for applying this method to derive the physical properties of magnesium oxide, initially, and eventually the other earth-metal oxides. These are discussed in turn below.

Pseudopotential calculations have been used successfully to predict the properties of semiconductors (see for example Ramchurn *et al*, 1990; Štich *et al*, 1992; or Bird *et al*, 1992) and covalent insulators such as silicon dioxide (see for example Allan and Teter, 1987; Bar-Yam and Pantelides, 1989; or Chelikowsky *et al*,

1990). To obtain confidence in the competence of this technique it is necessary to apply it to as wide a range of different materials as possible. Are predictions made for the properties of metals and ionic crystals as accurate as those already made for silicon? Magnesium oxide is an excellent archetype for this sort of calculation. In the past many different methods have been used to calculate the properties of MgO covering the full range of *ab initio* and empirical techniques. There is, therefore, a great opportunity to make a comparison of the accuracy with respect to the best results obtained by rival methods. It is also a strong test for the formulation of pseudopotentials that are able to accurately reflect the correct scattering properties of the ions. Although it will be shown in chapter 3 that it is relatively easy to simulate magnesium using a pseudopotential, oxygen is considerably more difficult and special optimisation techniques must be used to produce a useful potential.

Magnesium oxide is also of considerable interest in itself. It is a major constituent of the Earth's lower mantle so its properties at the pressures found in this region are important to geologists. Experimental data on the behaviour of MgO at high pressure is difficult to obtain and in its absence calculations must be used instead. Previous attempts to provide this data have been forthcoming only from empirical methods (which are unsatisfying as they are derived by fitting parameters in the calculation) or from theoretical methods that have failed to correctly describe the physics of MgO at equilibrium and are unlikely to achieve better results at high pressure. Accurate *ab initio* calculations of the properties at high pressure would provide a very useful insight into its behaviour in this important region. There is also good reason to study the charge density of MgO. Experiment shows that, unlike NaCl, MgO is not a perfect ionic crystal. In NaCl the pairwise nature of the interaction between the ions leads to the Cauchy condition that the elastic constants C_{12} and C_{44} are equal. Experimental results show that this is not true

for MgO as C_{44} is greater than C_{12}. It is, naturally, expected that this will be reflected in the values of these constants that are predicted in these calculations. It is also hoped that studying the charge distribution in MgO will reveal evidence of the mechanism that produces this violation of the Cauchy condition.

Finally, having studied MgO in great detail, it is instructive to compare its properties with the other earth-metal oxides. There are many similarities between the properties of MgO, CaO, SrO and BaO and these should be shown in the calculated predictions. There are also systematic differences between the properties of these oxides linked to the increasing size of the metal ion and the volume occupied by its core. The Cauchy violation, for example, is present in all of these oxides. Its magnitude, however, is steadily reduced as the series moves down the periodic table. It is at its strongest in MgO, and progressively smaller in CaO and SrO. The trend continues to such an extent that in BaO the sign of the violation is reversed as C_{12} is now greater than C_{44}. Once again the study of the distribution of charge density will illustrate these changes and hint at the mechanisms involved.

The structure of this thesis is as follows. In chapter 2 the basic theory underlying the method will be discussed. The density functional theory and the local density approximation will be derived to transform the problem we face from the (insoluble) many electron Schrödinger equation to the (soluble) single electron Kohn-Sham equation. Pseudopotentials will be briefly introduced and the total energy equation will be developed with plane waves being used as the basis set. The minimisation of this total energy will then be achieved using a method based on that of Car and Parrinello (1985), but which has been considerably refined subsequently. The strategy for parallelisation is finally described to enable use to be made of the large parallel surfaces now available for computing.

Chapter 3 describes in detail the methods that are used to generate pseudopotentials. The two different methods for producing norm-conserving pseudopotentials are introduced and the Kleinman and Bylander (1982) form of the potential is used to retain the efficiency of the energy minimisation. Two rival techniques for optimising the performance of the potentials are then described. The process of generating pseudopotentials is depicted with respect to magnesium and oxygen. Magnesium is an example of an element that requires only a straightforward application of the norm-conserving techniques to produce a useful pseudopotential. The oxygen potential, as mentioned above, needs optimisation before it can be used in any meaningful calculations. Finally the amending of pseudopotentials to apply non-linear core corrections is described.

Chapter 4 contains the results obtained from calculations of the properties of MgO. Initially MgO at equilibrium is investigated and the predictions are compared to those obtained previously by rival methods. This will enable us to establish whether a pseudopotential method will produce results of the same accuracy for MgO as those already reported for, say, silicon. The high pressure properties of MgO will then be calculated to determine the pressure dependence of the elastic constants. Factors of geological importance, such as the various seismic wave velocities, will then be derived from this data. Lastly the charge density patterns of MgO at equilibrium, and strained around this point, are studied in real and reciprocal space to reveal the mechanisms responsible for the behaviour of its physical parameters and their effect on the Cauchy violation.

Chapter 5 broadens the field to include predictions of the properties of the other earth-metal oxides. These predictions are made at equilibrium and are followed by an investigation of the transferability of their pseudopotentials. The core corrected results will then be calculated for the same materials as, unlike MgO,

they are found to have a significant effect on the values of the results predicted. As will be seen in chapter 5 the application of core corrections to the metal pseudopotentials is necessary to ensure their transferability. It does not, however, necessarily result in an increase in accuracy with respect to experiment. The charge distribution patterns will also be studied to gain a greater understanding of the physical processes at work within these oxides that lead to the reversal of the Cauchy violation.

In chapter 6 the major results will be summarised and conclusions will be drawn.

Chapter 2

THEORY

This chapter introduces the theory necessary to calculate the equilibrium total energy of a system by an *ab initio* method using a plane wave basis. The foundation of this is the Density Functional Theorem and the Local Density Approximation. These are described in section 2.2. Following this there is a brief introduction to pseudopotentials which we will use to represent the ions in the system. A fuller account of pseudopotential theory occurs below in chapter 3. Next the plane wave basis is applied to the total energy equation to derive the form which the computer will evaluate. The technique for obtaining the correct ground-state from this total energy equation is described next. Finally the computer implementation of this is discussed. Atomic units are used throughout and the energy is given in Rydbergs.

2.1 Introduction

The aim of this work is to calculate from first principles the ground-state properties of solids. As a starting point we have only the atomic numbers and the

atomic coordinates with no adjustable parameters. From these we wish to evaluate the total energy of a system and then study the forces on the atoms and the dynamics of the solid. At first glance this calculation involving, say, 10^{23} atoms looks totally beyond the limits of even the largest computer. Luckily there are a few short-cuts that we can take along the way.

The first step is the use of the *Density Functional Theorem* (DFT), with the effects of exchange and correlation represented by the *Local Density Approximation* (LDA). By applying the DFT it becomes possible to replace the (insoluble) many-electron Schrödinger equation with a set of single-electron Kohn-Sham equations. The only approximation inherent in this is the employment of the LDA to reproduce the little understood many-body effects felt by electrons in solids. Although this approach is seemingly crude it has proved to be remarkably successful. These measures have reduced our problem to one that is now, at least in principle, soluble by computer.

Secondly, the bare-atom potentials are replaced by pseudopotentials. There are a number of advantages in this. By treating the tightly bound core electrons as being frozen into (and partially screening) the ion core the problem can be reduced to that of the valence electrons only. This is valid as the electrons in the core have little influence over the properties of the solid. By reflecting only the smooth part of the valence electron wave functions and not the highly oscillatory states around the core, the number of plane waves needed to describe the system is reduced considerably. The ability to use a plane wave basis set is a very great advantage in itself, other ways of representing the atomic potentials such as *muffin-tin potentials*, require much more complicated basis-sets. This is important as only with plane waves is it easy to calculate derivatives of energy with respect to position needed to obtain the forces on the atoms. There is also

a large increase in accuracy in the calculation of binding energy when the energy of a solid is compared to that of the ions (nuclei and core electrons) rather than bare nuclei. For example, in the case of tungsten $E_{binding}/E_{total}$ (bare nuclei) $\sim$ 0.6/30000 whereas $E_{binding}/E_{total}$ (pseudopotential) $\sim$ 0.6/16 (Ihm, Zunger and Cohen, 1979).

Finally by making use of expressions for the charge density and potential in reciprocal space the translational symmetry of the system can be exploited, changing the problem from one of 10^{23} ions to a single unit cell only. Brillouin zone sampling is then introduced to remove the need to calculate the wave functions at every point in the Brillouin zone. In all of this it is necessary to assume a periodic system of unit cells. If a non-periodic system needs to be simulated (such as a surface or a dislocation) then this is done by reintroducing the periodicity via a supercell which includes, in the case of a surface calculation, several layers of atoms followed by a vacuum gap. Both slab and vacuum gap must be large enough to stop the surfaces from interacting with each other. For an example of this see the paper by Štich *et al* (1992) which calculates the total energy of the reconstructed silicon (111) surface using this method.

When these adjustments have been made to the original problem all that is left is for the computer to minimise the total energy expression to find the ground-state. This can be done in two basic ways. Firstly the Kohn-Sham equations (see below) can be solved self consistently by matrix diagonalisation methods. Once this has been achieved the calculated ground state charge densities can be simply plugged into the total energy expression. Alternatively, the total energy expression can be minimised directly itself, a method which was pioneered by Car and Parrinello (1985). It is one of these latter methods that we shall be using.

We now have a framework for the calculation of the properties of real solids from first principles which is within the capabilities of the computers available to us.

2.2 Density Functional Theory

The first difficulty that arises in performing crystal structure calculations by first principles quantum-mechanical methods is the intractable problem of the many-body effects due to the $\sim 10^{23}$ electrons in the solid. This is only made soluble by the bold approximation of the local density approximation within the framework of density functional theory.

The density functional theory (DFT) is a powerful method for calculating electronic and total electronic energy from first principles. It was first put forward by Hohenberg and Kohn (1964) in their paper on the Inhomogeneous Electron Gas and expanded to include exchange and correlation effects by Kohn and Sham (1965). Developed from the Thomas-Fermi method (see for example Lundqvist and March, 1983) the formalism uses electronic charge density in a central role and postulates that the total energy of electrons moving in a given external potential can be obtained from knowledge of the self-consistent charge density.

The formalism can be divided into two theorems as follows.

Theorem 1: *The complete many particle ground-state ψ is a unique functional $\psi[n(\mathbf{r})]$ of the ground-state charge density $n(\mathbf{r})$.*

Theorem 2: *The total electronic energy functional $E_{ee}[V_{ext}, n]$ obeys a variational principle in the charge density $n(\mathbf{r})$, i.e. it equals the ground-state energy*

for $n = \rho(\mathbf{r})$, the correct ground-state charge density. $V_{ext}(\mathbf{r})$ is the external potential.

Although the functional $\psi[n(\mathbf{r})]$ is not known we may still define another functional $F[n]$:

$$F[n] = \langle\psi|(T + V_{ee})|\psi\rangle, \tag{2.1}$$

where T and V_{ee} are the kinetic and electron-electron interaction operators of the many-electron system. This in turn must also be a unique functional of the charge density. If the system is subject to an external potential $V_{ext}(\mathbf{r})$ (such as that arising from the atomic nuclei), then one can derive yet another functional,

$$E_{ee}[V_{ext}, n] = \int d\mathbf{r} V_{ext}(\mathbf{r})n(\mathbf{r}) + F[n]. \tag{2.2}$$

This is the total energy of the many-electron system in the presence of the external potential V_{ext}. Once again it is a unique functional of $n(\mathbf{r})$, and $F[n]$ is not known.

The functional $F[n]$ can be expressed as,

$$F[n] = T[n] + \int d\mathbf{r} \int d\mathbf{r}' \frac{n(\mathbf{r})n(\mathbf{r}')}{|\mathbf{r} - \mathbf{r}'|} + E_{xc}[n]. \tag{2.3}$$

The first two terms on the right hand side represent the kinetic and Hartree energies repectively. The third term, $E_{xc}[n]$, is a universal functional of n and represents all corrections to the independent-electron model, i.e. correlation and non-classical many-body effects of exchange. This term still remains unknown.

Using theorem 2 we can make $n = \rho(\mathbf{r})$ and write the expression for the ground-state energy of a many-electron system in a given external potential $V_{ext}(\mathbf{r})$ as,

$$E_{ee}[V_{ext}, \rho] = T[\rho] + \int d\mathbf{r} V_{ext}(\mathbf{r})\rho(\mathbf{r}) + \int d\mathbf{r} \int d\mathbf{r}' \frac{\rho(\mathbf{r})\rho(\mathbf{r}')}{|\mathbf{r} - \mathbf{r}'|} + E_{xc}[\rho]. \tag{2.4}$$

There are still three problems in evaluating equation (2.4).

(i) A self-consistent method is needed to determine the $\rho(\mathbf{r})$ which minimises E_{ee}.

(ii) The evaluation of $T[\rho]$ given only $\rho(\mathbf{r})$ is not straightforward as there is no information on the wave functions.

(iii) The functional $E_{xc}[\rho]$ remains unknown, except for a few simple systems, and must be approximated in some way.

The first two difficulties can be tackled using the method of Kohn and Sham (1965). In this way a set of single-particle equations can be written for the variational wave functions of fictitious non-interacting electrons,

$$\left\{-\nabla^2 + V_{KS}[\rho(\mathbf{r})]\right\}\phi_j(\mathbf{r}) = \varepsilon_j\phi_j(\mathbf{r}), \tag{2.5}$$

where ϕ_j and ε_j are the single-particle wave functions and eigenvalues, respectively, and $V_{KS}[\rho(\mathbf{r})]$ is the effective potential within which the non-interacting electrons move.

Differentiating equation (2.4) with respect to $\rho(\mathbf{r})$ we can show that,

$$V_{KS}[\rho] = V_{ext}(\mathbf{r}) + \int d\mathbf{r}' \frac{2\rho(\mathbf{r}')}{|\mathbf{r}-\mathbf{r}'|} + \frac{\partial E_{xc}[\rho]}{\partial\rho(\mathbf{r})}, \tag{2.6}$$

or,

$$V_{KS}[\rho] = V_{ext}(\mathbf{r}) + V_H[\rho(\mathbf{r})] + V_{xc}[\rho(\mathbf{r})], \tag{2.7}$$

where V_H and V_{xc} are the coulomb and exchange-correlation potentials. The ground-state charge density $\rho(\mathbf{r})$ is defined as

$$\rho(\mathbf{r}) = \sum_j |\phi_j(\mathbf{r})|^2, \tag{2.8}$$

which requires the solution to be self-consistent. A value for $n(\mathbf{r})$ is assumed. From this a potential can be constructed using equation (2.6), a new value for

$n(\mathbf{r})$ is then obtained from equations (2.5) and (2.8). This process is repeated until there is no further change in $n(\mathbf{r})$ and the ground-state of the system has been reached. The charge density $n(\mathbf{r})$ is now equal to $\rho(\mathbf{r})$ and the energy can be extracted from equation (2.4).

The final difficulty can be overcome by applying the *local density approximation* (LDA) to $E_{xc}[\rho]$. In this approximation it is assumed that the contribution to E_{xc} from the small region of space around each point $\mathbf{r}$ is taken to be the same as it would be in a *uniform* electron gas with the same local electron density $\rho(\mathbf{r})$. Hence,

$$E_{xc}[\rho] \cong \int d\mathbf{r} \varepsilon_{xc}[\rho(\mathbf{r})]\rho(\mathbf{r}) \tag{2.9}$$

where $\varepsilon_{xc}[\rho]$ is the exchange-correlation energy per electron of a uniform electron gas of density ρ. The corresponding exchange -correlation potential can be shown from equations (2.6) and (2.7) to be,

$$V_{xc}[\rho] \simeq \frac{d}{d\rho(\mathbf{r})}(\rho(\mathbf{r})\varepsilon_{xc}[\rho(\mathbf{r})]). \tag{2.10}$$

From the results of accurate quantum Monte Carlo calculations for the total energy of uniform electron gases of various densities, such as those of Ceperley and Alder (1980), it is possible (though even now not trivial, see Perdew and Zunger, 1981, for example) to obtain an equation for ε_{xc} in the parameterised form,

$$\varepsilon_{xc} = \varepsilon_x + \varepsilon_c \tag{2.11}$$

with,

$$\varepsilon_x = -\frac{0.9164}{r_s} \tag{2.12}$$

and,

$$\varepsilon_c = 2 \times \begin{cases} -0.1423/(1 + 1.0529\sqrt{r_s} + 0.3334 r_s) & \text{for } r_s \geq 1, \\ -0.0480 + 0.0311 \ln r_s - 0.0116 r_s \ln r_s & \text{for } r_s < 1. \end{cases} \tag{2.13}$$

In this form r_s is related to ρ through the relation,

$$\rho^{-1} = \frac{4\pi}{3} r_s^3 \tag{2.14}$$

These are formulae gained by interpolation of the computational data and can not be obtained analytically.

In solids, where r_s is typically in the range 1 to 4, ε_{xc} is very nearly proportional to $\rho^{1/3}$. This is reminiscent of Slater's *ad hoc* simplification of the Hartree-Fock equations to take better account of the effects of exchange (see for example Ashcroft and Mermin, 1976). The whole of DFT rests on the usefulness of the LDA. Somewhat surprisingly it has turned out to be very successful in depicting the many-body effects of exchange and correlation. Without this crude and sweeping generalisation DFT could only be used in that small minority of very simple cases for which the true exchange and correlation potential are known. It should be noted that the DFT deals only with the ground-state properties of the solid. It is necessary to use many-body theory to correct DFT calculations in even the simplest cases of semiconductor band-gap calculations. See, for example, the work of Godby, Schlüter and Sham (1986).

We now have a one-body problem that is, in principle, soluble. It is now possible to define the total crystal energy as the sum of the lattice (ion-ion energy) and the electronic energy,

$$E_{tot} = E_{ion-ion} + E_{ee}[V_{ext}, \rho]. \tag{2.15}$$

Substituting for $E_{ion-ion}$ and E_{ee} gives,

$$E_{tot} = N_0 \sum_{\mathbf{p},s,s'}{}' \frac{z_s z_{s'}}{|\mathbf{p} + \mathbf{R}_s - \mathbf{R}_{s'}|} + T[\rho] + \int d\mathbf{r} V_{ext}(\mathbf{r})\rho(\mathbf{r})$$

$$+ \int d\mathbf{r} \int \mathbf{r}' \frac{\rho(\mathbf{r})\rho(\mathbf{r}')}{|\mathbf{r} - \mathbf{r}'|} + \int d\mathbf{r}\rho(\mathbf{r})\varepsilon_{xc}[\rho(\mathbf{r})], \tag{2.16}$$

where N_0 is the number of unit cells, $\mathbf{p}$ is a Bravais lattice vector, and $\mathbf{R}_s$ and $\mathbf{R}_{s'}$ are position vectors for the nuclear (core or ionic) charges z_s and $z_{s'}$ in the unit cell. The prime on the summation sign indicates that the $\mathbf{p} + \mathbf{R}_s - \mathbf{R}_{s'} = 0$ term is omitted. The ionic charges are assumed to be spherically symmetric and non-overlapping.

Equation (2.16) can be summarised as,

$$E_{tot} = E_{ion-ion} + E_{kin} + E_{el-ion} + E_{el-el} + E_{xc}. \tag{2.17}$$

If the electron-ion interaction V_{ext} is known, then E_{tot} can be calculated provided $\rho(\mathbf{r})$ is known from, say, the self-consistent solution of equation (2.5). Care must be taken with the first, third and fourth terms to avoid divergences. More will be said about this later.

2.3 Pseudopotential Theory

We must now find some way to describe the potential $V_{ext}(r)$ felt by the electrons due to the ion cores. There are two major constraints on the way we can do this that require the atoms to be modelled as pseudopotentials. Firstly, as pointed out before a very great increase in accuracy can be achieved by removing the core electrons from the calculation by freezing them into the ion cores. This obviously reduces the amount of computation required as well. Secondly, in order to obtain derivatives of the energy easily it is necessary to use plane waves as the basis-set. This is because, unlike most other basis sets, plane waves are defined over all space rather than being attached to particular core or interstitial regions. With very deep bare-atom potentials it would require a prohibitively large number of plane waves to represent the rapid variation near the core, this number is obviously reduced if the core effects are removed.

The first pseudopotentials were introduced by Phillips and Kleinman (1959). Their work was followed and expanded by that of Cohen and Heine (1961); Austin, Heine and Sham (1962) and Abarenkov and Heine (1965). A good summary of this early theory can be found in the three review articles by Heine (1970); Cohen and Heine (1970) and Heine and Weaire (1970). The more modern theories involving *norm-conserving* and *separable* pseudopotentials will be discussed below in chapter 3.

In general a pseudopotential is non-local and can be represented as an angular-momentum-dependent potential of the form,

$$\hat{v}_s(\mathbf{r}) = \sum_l v_{s,l}(\mathbf{r})\hat{\mathcal{P}}_l, \tag{2.18}$$

where $\hat{\mathcal{P}}_l$ is the projection operator for angular momentum l and s identifies the atom.

This can be decomposed arbitrarily into local and non-local parts,

$$\hat{v}_s(\mathbf{r}) = v_s^L(r) + \sum_l \Big(v_{s,l}(\mathbf{r}) - v_s^L(r)\Big)\hat{\mathcal{P}}_l \tag{2.19}$$

which can be expressed as,

$$\hat{v}_s(\mathbf{r}) = v_s^L(r) + \Delta\hat{v}_s^{NL}(\mathbf{r}). \tag{2.20}$$

Now v_s^L is a local function and $\Delta\hat{v}_s^{NL}$ is a non-local, l-dependent correction term. In practice, for the potentials most usually dealt with, this term is only needed for $l = 0, 1, 2$. The form of the pseudopotential in equation (2.20) has been termed by Kleinman and Bylander (1982) as *semi-local.* This is because although the potential is non-local in the angular momentum quantum number l, it is still local in radial coordinate. If a potential of this form were used in Car-Parrinello type calculations it would be very inefficient. The process of formulating a fully non-local pseudopotential without this problem is described in chapter 3.

2.4 Plane Wave Basis for Total Energy

It can be seen that we now have, in principle, enough information to calculate the total energy of a solid and the forces on its ions. As the solids that we model must be periodic it is convenient to express all the terms as their Fourier transforms in k-space as well as real space. As mentioned earlier it is possible to handle non-periodic structures, such as surfaces or dislocations, by including them in very large cells (which can be periodic) made from a number of real unit cells. Although theoretically the pseudo-wave functions can be expanded in a number of ways (as Gaussians or mixed basis sets, for example) for the reasons stated previously it is advantageous to use plane waves. When expanded using a plane wave basis the wave function becomes,

$$\phi_j(\mathbf{k},\mathbf{r}) = \frac{1}{\sqrt{(N_0\Omega)}} \sum_{\mathbf{G}} c_j(\mathbf{k}+\mathbf{G}) \exp[i(\mathbf{k}+\mathbf{G})\cdot\mathbf{r}], \tag{2.21}$$

where the solid is made from N_0 unit cells of volume Ω each. The $\mathbf{G}$ are the reciprocal-lattice vectors. We can also write down the crystal potential as a sum of non-overlapping ionic pseudopotentials at positions $\mathbf{R}_s$. This is equivalent to the V_{ext} potential of equation (2.2),

$$V_{ext}(\mathbf{r}) = V_{ps}(\mathbf{r}) = \sum_{\mathbf{p}} \sum_{s} \hat{v}_s(\mathbf{r}-\mathbf{p}-\mathbf{R}_s). \tag{2.22}$$

By making the substitutions from equations (2.21) and (2.22) the single-particle Schrödinger equation (2.5) can be solved and the self-consistent charge density calculated. Ihm, Zunger and Cohen (1979), Ihm (1988) and Srivastava and Weaire (1987) give details of conventional methods of solving equation (2.5).

In k-space the charge density from equation (2.8) becomes,

$$\rho(\mathbf{q}) = 2 \sum_{\mathbf{k}} \sum_{j}^{occ} \sum_{\mathbf{G},\mathbf{G}'} c_j^*(\mathbf{k}+\mathbf{G}') c_j(\mathbf{k}+\mathbf{G}) \delta_{\mathbf{G}-\mathbf{G}',\mathbf{q}}, \tag{2.23}$$

where j sums over occupied states and the factor of 2 accounts for spin degeneracy. The sum over k in equation (2.23) is over all k-points in the Brillouin zone. This can be reduced considerably by calculation only at special points such as those suggested by Monkhorst and Pack (1976). It is through the use of k-point sampling, and the use of a cut-off for the reciprocal lattice vectors G (allowable because the pseudopotentials are soft core and cut-off rapidly in k-space) that the problem of 10^{23} atoms making up a real solid can be reduced to a size that the computer can handle.

Charge density is the central quantity in the density functional theory. Once the wave function coefficients c_G have been calculated, by whatever means are available, it is simple to obtain E_{tot} from equation (2.16). As noted previously care must be taken with the first, third and fourth terms of equation (2.16). This is because $V_H(\mathbf{G}=0)$, $V_{ps}(\mathbf{G}=0)$ and the summation over $\mathbf{p}, s, s'$ are all divergent. The method of Ihm, Zunger and Cohen (1979) is used to overcome this problem. The single electron Schrödinger equation (in momentum space) is solved with $V_H(0) = V_{ps}(0) = 0$. This is the equivalent of a small constant shift in potential and is compensated for by the addition of E_0, the pseudopotential core correction term.

Finally the total energy can be written down in a form that a computer can evaluate. Once the ground-state wave function coefficients c_G are evaluated we have all the information necessary to calculate the ground-state total energy of the system. Rather than using equation (2.16) directly it is natural to follow the scheme of Ihm *et al* (1979), (see also Ihm, 1988, and Srivastava and Weaire, 1987). The total energy is calculated from the sum of the energy eigenvalues ϵ_j and corrected (as necessary) for each term of the total energy equation (2.16).

The eigenvalue sum can be written as,

$$\sum_j \varepsilon_j = T_s[\rho] + \int d\mathbf{r}\rho(\mathbf{r})V_{tot}(\mathbf{r}), \tag{2.24}$$

where T_s is the kinetic energy of the system. The total energy then becomes,

$$E_{tot} = \sum_j \varepsilon_j - E'_H + \Delta E_{xc} + \gamma_E + E_0. \tag{2.25}$$

Here,

$$E'_H = \frac{1}{2}\sum_{\mathbf{G}\neq 0} \frac{4\pi e^2}{|\mathbf{G}|^2}|\rho(\mathbf{G})|^2, \tag{2.26}$$

is the correction to the total energy due to overcounting the Hartree energy in equation (2.25),

$$\Delta E_{xc} = \sum_{\mathbf{G}} \rho^*(\mathbf{G})[\varepsilon_{xc}(\mathbf{G}) - V_{xc}(\mathbf{G})], \tag{2.27}$$

is the correction due to overcounting the exchange and correlation energy in equation (2.25) and,

$$\gamma_E = N_0\frac{e^2}{2}\sum_{s,s',\mathbf{p}\neq 0} \frac{z_s z_{s'}}{|\mathbf{p}+\mathbf{R}_s-\mathbf{R}_{s'}|} - \frac{1}{2}\frac{1}{\Omega_{at}}\sum_s \int d\mathbf{r}\frac{z_s^2 e^2}{r}, \tag{2.28}$$

is the lattice energy. This is evaluated by Ewald's summation method (see for example Maradudin *et al*, 1971). Finally,

$$E_0 = \frac{1}{M}\sum_s z_s \frac{1}{\Omega_{at}}\sum_s \int d\mathbf{r}(v_s(\mathbf{r}) + \frac{z_s e^2}{r}), \tag{2.29}$$

is the pseudopotential core energy correction. M is the number of basis atoms in the unit cell.

2.5 Minimisation of the Total Energy

In order to derive the properties of a material it is necessary for us to find the correct ground-state of the system. Theorem 2 of the density functional theory allows us to calculate the minimum total energy of a system when the correct

(self-consistent) ground-state charge density has been established. Our task is reduced, therefore, to finding a convenient technique to evaluate the wave function coefficients c_G. There are two ways that these can be calculated.

First, the Kohn-Sham equations (2.5) can be solved by matrix diagonalisation. The one-electron Schrödinger equation is solved by expressing the one-electron Hamiltonian $-\frac{1}{2}\nabla^2 + V_{KS}$ in matrix form. This can then be diagonalised to obtain approximate eigenfunctions and eigenvalues of the original Hamiltonian. A new electron density can then be constructed from the eigenfunctions and a new V_{KS} is obtained. This process is iterated to self-consistency to produce to ground-state charge density. It is now a simple matter to substitute the ground-state charge density into the total energy equation (2.25) to obtain the energy minimum. Although matrix diagonalisation can be used in conjunction with pseudopotentials and a plane wave basis it is often impractical to do so. This is because the standard diagonalisation techniques have a CPU time that scales as n^3, where n is the number of wave function coefficients. Calculations are, therefore, limited to systems for which $n < 1000$ or so. Alternatively, more sophisticated iterative diagonalisation methods scale as bn^2 where b is the number of bands required in the calculation. Obviously this makes calculations involving large numbers of plane waves prohibitive.

An alternative to the diagonalisation of the Kohn-Sham equation is to minimise the total energy equation (2.25) directly by some means. The total energy is simply considered to be a function of the c_Gs and by minimising this function (subject to the constraints of keeping the wave functions orthogonal) we can directly obtain the total energy of the system. A particularly attractive way of achieving this is to use the technique of *fictitious* molecular dynamics (MD). This is simply a trick to find the ground-state c_G as if they were particles obeying

classical equations of motion. Car and Parrinello (1985) were the first to describe an *ab initio* method for performing fictitious MD calculations on the c_Gs. They realised that the concept of simulated annealing, developed in a Monte-Carlo method by Kirkpatrick, Gelatt and Vecchi (1983), could be converted to MD to provide this *ab initio* simulation of solids. When molecular dynamics is performed on a damped classical system the system eventually settles into the potential energy minimum. Here Car and Parrinello (1985) used the c_G as fictitious classical particles to minimise the DFT functional $E[n]$. Lagrangian equations of motion are set up from the the total energy equation with damping to remove kinetic energy slowly from the system until the wave function amplitudes are in their ground-states. This is analogous to the annealing of a substance as it cools. In this way the Car-Parrinello (CP) method achieves a direct minimisation of the LDA total energy.

The importance of this method is due to the speed of calculation that is possible compared to that of the matrix diagonalisation above. Rather than the cumbersome n^3 or bn^2 scaling of the CPU time to determine the total energy of a system the CP method can be made to run much faster. In the plane wave representation the kinetic energy term of the total energy equation (2.25) is diagonal in reciprocal space whereas all the other terms are diagonal in real space provided the pseudopotential is local. Each term is computed in whichever space is most efficient (with a scaling proportional to n). As information is required from both the rate determining step is now that of the fast Fourier transform which converts information between real and reciprocal space. This has a time dependence proportional to $n \ln n$. This must be done for each band so the final timing scales as $bn \ln n$. Once more the n is the number of wave function amplitudes c_G and the b is the number of bands in the system. In calculations where n can run into the tens of thousands or more the saving in computer time is obviously very great

indeed. It is very important to retain this advantage when using non-local pseudopotentials. For this reason the use of the Kleinman and Bylander (1982) form for non-local pseudopotentials (described below in chapter 3) is crucial. Without this innovation the non-local part of the calculation would introduce a scaling proportional to n^2 and the advantage of CP methods over matrix diagonalisation would be lost.

The computer must also spend time orthogonalising the wave functions as this is a constraint on the c_Gs. This calculation has a scaling proportional to b^2n. If a calculation were to involve, say, 100 ions then there might be between 100 and 400 bands present in the calculation. In this case the time taken in orthogonalisation of the wave functions would become the most important factor, even though n might now be 10^5. This timing will come to dominate calculations of very large systems. Even in this case though, the calculation will still proceed more quickly than an equivalent matrix diagonalisation.

Since Car and Parrinello's original work there have been a number of modifications proposed to improve the efficiency of this technique, especially for calculations dealing with large numbers of ions, large energy cut-offs for the pseudopotentials or both. Payne *et al* (1986) showed that by integrating the equations of motion analytically (before orthogonalising the wave functions) the number of iterations required to reach convergence was reduced considerably. In the example they quote (an eight-atom cell of germanium in diamond structure) the number of steps needed for self-consistency was reduced by an order of magnitude.

Even with this increase in computational efficiency there are still problems with very large calculations. Numerical instabilities in the equations of motion lead to the electron density overreacting to changes in the potential. No equilibrium

state can be reached unless the system is correctly damped. Teter, Payne and Allan (1989) suggested a scheme for performing CP calculations that would scale favourably with increasing numbers of plane waves and avoid numerical instabilities in large systems. They describe a preconditioned conjugate gradients method to work out the ground-state energy E of the solid with respect to the plane wave coefficients c_G. The gradient $\partial E_{tot}/\partial c_G$ is calculated at each iteration and used to amend the next estimate of the eigenvector. To improve convergence further the potential is updated after every band is calculated. This method has a number of advantages over other techniques for evaluating the minimum energy. It is the fastest iterative diagonalisation method currently known for large problems. Every iteration lowers the the total energy. There are no instabilities in the charge density and it is numerically stable. Finally it requires no arbitrary parameters such as time steps or fictitious particle masses. It is this method that we use in this thesis.

2.6 Implementation on Computer

The code to perform an energy minimisation using a fictitious molecular dynamics method similar to that of Car and Parrinello (1985) follows the approach of Payne *et al* (1986). Modifications over the years have improved its performance. Allan and Teter (1987) used the Kleinman and Bylander (1982) form of non-local pseudopotentials to properly account for their properties without slowing the computing down to the same level as matrix diagonalisation methods. To make the code even more efficient the algorithm to find the energy minimum was changed to that of a preconditioned conjugate gradients procedure by Teter, Payne and Allan (1989). This technique is reckoned to be the most efficient available. Further improvements are possible with the use of real space potentials

(see the paper by King-Smith, Payne and Lin, 1991), but in order to deal with large systems (with hundreds of ions) or badly behaved pseudopotentials (such as first row elements or transition metals) with large energy cut-offs, benefits are likely to come from changes in the computer hardware on which the code is run. The introduction of parallel computers provides the opportunity for this development.

The pseudopotentials used determine the energy cut-off needed in the calculation. Well behaved pseudopotentials require small cut-off energies. Silicon, for example needs a cut-off of < 150 eV. Badly behaved potentials, however, need cut-off energies much greater than this. These can be in the thousands of electron volts. This is explained in more detail in chapter 3 below. The plane waves used in the calculation are all those that have an energy less than the cut-off energy of the pseudopotential. These are contained within a sphere around the (0,0,0) point in k-space with a radius equivalent to the energy cut-off. The fast Fourier transform routine performs its calculations on a limited volume in k-space. This FFT box is specified by the user. To ensure a faithful representation of the charge density the FFT box must include components in all directions much further than the cut-off used for the wave functions. This is because the charge density (in real space) is of the form,

$$\rho(\mathbf{r}) \sim \sum_{\mathbf{G}} \sum_{\mathbf{G}'} c_{\mathbf{G}} c^*_{\mathbf{G}'} \exp\left[i(\mathbf{G} - \mathbf{G}') \cdot \mathbf{r}\right]. \tag{2.30}$$

The Gs are those contained within the cut-off sphere. In order to accommodate the $\mathbf{G} - \mathbf{G}'$ terms within the FFT box it must extend twice as far out as the sphere itself. The basic geometry used by the program is that of a sphere of plane waves contained within an FFT box whose side length is twice the diameter of the sphere. It is possible to get away with a box slightly smaller than this without losing significant accuracy in the calculation.

In order to study systems that are large enough to be of practical interest it is necessary to use the largest super computer available. The answer was the *grand challenge* computer in Edinburgh. This is a 64-node Meiko i860 Computing Surface. Each node has 16 Mbytes of memory allowing a total of 1 Gbyte to be accessed if all nodes are used. If the code running on it is efficiently parallelised then the theoretical performance of the machine is around 1 Gflop (see the paper by Clarke, Štich and Payne, 1992, for a fuller description). The energy minimisation program to be run on this surface is called the *Cambridge Edinburgh Total Energy Package* or CETEP.

In any calculation the plane wave coefficients c_G are represented by a complex array. This is of the form $C(n, b, k)$, where n and b are the number of coefficients and the number of bands in the calculation as before. The final quantity k is the number of special k-points which are used in the Brillouin zone sampling. In order to parallelise the CETEP code three avenues of approach present themselves corresponding to splitting the calculation between nodes according to any of the three quantities above.

The first (and most straightforward) method that could be applied is to divide the calculation by giving a single k-point to each node. This presents few problems as computations relevant to each k-point (including the FFT and orthonormalisation) are independent. It is necessary only to synchronise the nodes so that the total charge density and total energies can be summed from the contributions at each k-point. There is a major drawback to this approach. The number of special k-points required by the calculation is in inverse proportion to the number of atoms in the system being studied. Clarke, Štich and Payne (1992) estimate that convergence with respect to Brillouin zone sampling with a single k-point for metals is achieved for unit cells with around 1000 atoms. Even with unit cells

containing considerably fewer atoms the number of special k-points used need often be as few as four. As the CETEP code is designed to be used on just these large systems it would be of little use to attempt parallelisation by this method.

As an alternative the computation might be split between nodes by assigning separate nodes to work on different bands. This is possible as calculations performed on each band are largely independent of each other. Care must now be taken with the orthogonalisation as information is obviously required about the wave functions from all bands. This technique has a couple of drawbacks. The band-by-band energy minimisation of the conjugate gradient method must be abandoned for one that is slightly less efficient. It is also necessary to replicate a good deal of the data (specifically the FFT mesh) on all nodes. This is obviously very wasteful of memory.

The final approach to parallelisation is to split the wave functions themselves between the nodes on the computer. This involves parallelisation of the fast Fourier transform routine and, once more, care with the orthogonalisation. The FFT mesh is divided between the nodes by storing specific reciprocal space columns in the x-direction (and their associated yz-planes in real space) on different nodes. The x-columns are distributed so that there are approximately the same number of plane waves on each node to ensure greatest efficiency. The drawback to this method is the extra communication required between the nodes compared with the other techniques.

It was the third path that was chosen for the CETEP program. The conversion of the existent serial energy minimisation codes was achieved by Clarke, Štich and Payne (1992). This has already been used successfully by other groups (see for example De Vita *et al*, 1992a and 1992b; Štich *et al*,1992, or Bird *et al*, 1992).

In order to run the CETEP codes the user must set a number of parameters in the main program and provide three data files of information. The parameters required are those that are used to define the size of the various arrays in the calculations. These include the size of the k-space box, the number of ions, the number of electron bands needed and the number of special k-points. The pseudopotentials needed to represent the atoms in the calculation are read in from one data file. They are expressed in the Kleinman and Bylander (1982) form. See chapter 3 for full details of how these are constructed. Next the program needs to read a file with details concerning the running of the code. The number of iterations, how many species, how many ions of each species and what value of energy cut-off are all entered at this stage. The final data file contains information on the lattice vectors of the unit cell, the positions of the ions and the position and weighting of the special k-points to be averaged over in the calculation.

2.7 Summary

The density functional theory with the local density approximation have been shown to allow an effective one-particle solution for the energy of a solid. The only approximation inherent in this is the local density approximation which has been successfully applied to many problems before. This solution has been expressed using a plane wave basis and with pseudopotentials to represent the ions in the system. An efficient algorithm has been developed to find the ground-state wave function coefficients (and hence the energy) rapidly using a large parallel computer.

Chapter 3

PSEUDOPOTENTIALS

This chapter deals in detail with the formulation and testing of pseudopotentials for *ab initio* total energy calculations. The rival methods for generating *norm-conserving* pseudopotentials are considered. The *separable* form of the potential is introduced to ensure computational efficiency and techniques of optimisation are discussed. The codes to generate and test the pseudopotentials are then described. Magnesium pseudopotentials are created to demonstrate the process for a well behaved ion, this is contrasted with the pseudopotentials of oxygen which is an extremely badly behaved ion. Finally there is a section on the application of non-linear core corrections. Atomic units are used throughout this chapter with energy in Rydbergs except where specifically stated otherwise.

3.1 Introduction

As the previous chapter outlined, pseudopotentials are used to describe the potential felt by the electrons due to the ion cores within the solid. The principle reasons for this choice are the large increase in accuracy of this approach and

the ability to express the wave functions as plane waves. When pseudopotentials were first introduced by Phillips and Kleinman (1959), as an extension of the earlier Orthogonalised Plane Wave (OPW) method (Herring, 1940), they placed only one restriction on the formulation of the effective potential. This was that the pseudo-wave functions should have the same energy eigenvalues as the wave functions of the true atomic potential. It was soon realised that there were many alternative weak effective potentials for which this condition was satisfied.

This flexibility has been exploited in a number of ways over the years. Empirical pseudopotentials (Cohen and Bergstresser, 1966) are produced by empirically fitting the total effective potential acting on the electrons, including Hartree and exchange-correlation contributions as well as the ionic parts, to experimentally determined features of the energy bands. The potential is then of enforced smoothness as only a few terms of the Fourier expansion are used. In this way, however, the wave functions are only approximately described. Model pseudopotentials (Abarenkov and Heine, 1965) make use of the OPW concept underlying the method to derive pseudopotentials from atomic calculations. These potentials are generally *hard core* in character, that is they are strongly repulsive at the origin. The resulting wave functions generally exhibit the correct shape outside the core region; but they differ from the real wave functions by a normalisation factor. Accurate charge densities, outside the core region, are difficult to obtain as the normalised pseudo-wave functions must be orthogonalised to the core states and renormalised before they can be squared. Aspects of these two approaches were combined rather uneasily together by Schlüter *et al.* (1975) to make semiempirical pseudopotentials.

All these methods are unsatisfactory for our work. Empirical potentials are obviously useless for *ab initio* calculations. Model potentials are too *hard core* for

rapid convergence of the Fourier expansion, and have wave functions that need normalisation. Apart from the semiempirical pseudopotential, none of these potentials are transferable. That is they are unable to represent the ion potential in other geometries (such as surfaces), or configurations (e.g. from neutral atoms to their fully ionised states).

3.2 Norm-conserving Pseudopotentials

There are several characteristics that we need in our pseudopotentials that have not been satisfied by the families of potentials discussed so far. We need pseudopotentials that are generated from first principles calculations, rather than from empirical fits to experimental data. Our potentials must be fully transferable to model ions in all chemical environments. The pseudo-wave functions must agree with the real wave functions (outside the core radius r_c) without recourse to normalisation and the valence charge density should be obtained simply by squaring the wave functions. Finally the resulting pseudopotential must be soft-core in nature to keep the number of Fourier components needed to represent the potential in k-space as small as possible. Only with the introduction of norm-conserving pseudopotentials are these criteria fulfilled.

3.2.1 The Hamann, Schlüter and Chiang Method

Hamann, Schlüter and Chiang (1979) suggested four desirable properties for pseudopotentials that would produce these effects.

(i) Real and pseudo-valence eigenvalues should agree for a chosen electronic con-

figuration. This is the original condition used by Phillips and Kleinman (1959) to define pseudopotentials. If the potentials generated by this method are truly transferable the electronic configuration chosen is unimportant. Transferability may, however, be adversely affected by modifications made to the potential (such as optimisation or use in the Kleinman and Bylander (1982) form, see later) to improve computational efficiency.

(ii) Real and pseudo-atomic wave functions should agree beyond the chosen core radius r_c. This core radius can then be varied to obtain the right compromise between the strength of the potential and the essential information about the real atom that it contains.

(iii) The integrals from 0 to r of the real and pseudo-atomic charge densities agree for all $r > r_c$ for each valence state. This is the norm-conservation condition.

(iv) The logarithmic derivatives of the real and pseudo-atomic wave functions and their first energy derivatives agree for $r > r_c$. The logarithmic derivatives of the wave functions are a good measure of the scattering properties of the ion cores. For the pseudopotential to give a good representation of the properties of real solids it must obviously mimic the scattering of the true ion core very closely.

It is the last two properties that are the important ones. In order for the pseudopotential to be transferable it must have scattering properties that correctly reproduce those of the real ion cores even as bonding shifts the eigenenergies away from the atomic levels (which we know to be correct because of property (i)). Topp and Hopfield (1974) derived an identity for pseudopotentials that links property (iii) and property (iv). In atomic units,

$$\frac{1}{2}\Big[(r\phi)^2 \frac{d}{d\epsilon}\frac{d}{dr}\ln\phi\Big]_{r_c} = \int_0^{r_c} \phi^2 r^2 dr, \tag{3.1}$$

where ϕ is the pseudo-wave function, ϵ is the energy and r_c is the core radius. It can be seen that due to this identity it is only necessary to ensure the correct amount of charge density within the core radius in order to reproduce the correct energy dependence of the logarithmic derivatives of the wave functions to first order at least. Actually agreement between the logarithmic derivatives of the pseudopotential and its all-electron equivalent is usually much better than this would suggest. Often the scattering properties are correctly reproduced over a wide energy range.

With only the first three properties required for the production of a useful pseudopotential Hamann *et al* (1979) suggested the following procedure. A full core *ab initio* calculation of the atom is made to establish the atomic potential $V(r)$ and $u_l(r)$ which is defined as r times the valence wave function. The full atomic potential $V(r)$ is multiplied by a smooth short-range cut-off function to remove the strongly attractive part of the potential. This cut-off function is parameterised so the new potential $V_{1l}^{PS}(r)$ can be adjusted to yield the correct atomic eigenvalues. This satisfies property (i). The new potential takes the form,

$$V_{1l}^{PS}(r) = V(r)[1 - f(r/r_{cl})] + c_l f(r/r_{cl}). \tag{3.2}$$

The pseudopotential is now non-local because each angular momentum component l has a different $V_{1l}^{PS}(r)$. r_{cl} is the core radius for each different l, typically this is taken to be close to the outermost peak in u_l. c_l is the parameter used to adjust the potential so it gives the correct eigenvalue. $f(x)$ is the cut-off function. It must tend to 0 as $x \to \infty$ and cut-off for $x \approx 1$, that is when $r \approx r_{cl}$. It must also approach 1 for $x \to 0$ at least as fast as x^3 to avoid a r^{-2} divergence in the pseudopotential at small r. This divergence arises from the r^{l+1} behaviour of the wave function at this point (Bachelet, Hamann and Schlüter, 1982). Hamann,

Schlüter and Chiang (1979) chose as $f(x)$,

$$f(x) = \exp(-x^{\lambda}), \tag{3.3}$$

where $\lambda \geq 3$. Property (ii) is now also satisfied as for $r > r_{cl}$,

$$\gamma_l w_{1l}(r) \rightarrow u_l(r), \tag{3.4}$$

as they both satisfy identical differential equations and boundary conditions outside the core. $w_{1l}(r)$ is the (nodeless) solution of the radial Schrödinger equation with potential V_{1l}^{PS}, and γ_l is just a multiplicative constant.

The final step is to implement the norm-conservation condition of property (iv). The intermediate pseudo-wave function w_{1l} is modified by another cut-off function to produce the final (nodeless) pseudo-wave function w_{2l}.

$$w_{2l}(r) = \gamma_l[w_{1l}(r) + \delta_l g_l(r/r_{cl})], \tag{3.5}$$

where $g_l(x)$ is a function that cuts-off for $x > 1$, and behaves as x^{l+1} at small x. This is to ensure that the pseudo-wave function is still a good solution of the Schrödinger equation. The suggested choice for g_l is,

$$g_l = x^{l+1} f(x). \tag{3.6}$$

The factor δ_l is obtained from the solution to the condition that w_{2l} is normalised,

$$\gamma_l^2 \int_0^{\infty} [w_{1l}(r) + \delta_l g_l(r/r_{cl})]^2 dr = 1. \tag{3.7}$$

Inversion of the radial Schrödinger equation with eigenfunctions w_{2l} will obtain the final norm-conserving pseudopotential V_{2l}^{PS}.

This method was developed further in a paper by Bachelet, Hamann and Schlüter (1982) which found the optimum value of λ (3.5), and the core radii r_{cl} for all elements from hydrogen through to plutonium. A full list of the parameters used to create norm-conserving pseudopotentials by this method was also included for the elements to plutonium.

3.2.2 The Kerker Method

An alternative way of constructing norm-conserving pseudopotentials was put forward by Kerker (1980). Rather than imposing conditions on the potential a simpler and more direct method is to modify the wave functions directly to achieve the desired properties for the pseudopotential.

Once more a series of four conditions are applied to the formulation of the pseudopotential. Three of these are identical to those of Hamann, Schlüter and Chiang (1979). As the fourth condition proved to be redundant it is now replaced by the new condition (iv) which is used to help the pseudopotential converge rapidly in Fourier space. This new condition is as follows,

(iv) The first and second derivatives of the pseudo-wave functions are matched to the real values at r_c. This matching of the first and second derivatives of the wave functions at r_c ensures that there is no sharp kink at this point that might produce poorly converged high order terms in Fourier space. The resulting potential will be continuous, but has a discontinuous first derivative at r_c. This kink in the potential can be minimised by varying r_c.

As before the shape of the valence wave function within r_c is replaced by a convenient analytical form,

$$u_l(r) = r\phi(r) = r^{l+1} f(r). \tag{3.8}$$

The function $f(r)$ is chosen to give a smooth nodeless wave function as required by condition (ii). Two possible functions that could be used for $f(r)$ might be a polynomial,

$$f(r) = p(r) = \alpha r^4 + \beta r^3 + \gamma r^2 + \delta, \tag{3.9}$$

or an exponential,

$$f(r) = \exp(p(r)). \tag{3.10}$$

As there is no guarantee that the polynomial $p(r)$ would produce nodeless wave functions the exponential is the form that is used. The screened pseudopotential can be obtained analytically from the Schrödinger equation in atomic units (for $r \leq r_c$),

$$\left[-\frac{d^2}{dr^2} + \frac{l(l+1)}{r^2} + V_l^{PS}(r)\right] r^{l+1} f(r) = E_l r^{l+1} f(r). \tag{3.11}$$

This is inverted to produce (once more for $r \leq r_c$),

$$V_l^{PS}(r) = E_l - \frac{l(l+1)}{r^2} + \frac{1}{r^{l+1} f(r)} \frac{d^2}{dr^2}\left(r^{l+1} f(r)\right). \tag{3.12}$$

This is a form of the pseudopotential that can be used when the values of the parameters of $p(r)$ in equation (3.9) are known. In order to ensure that V_l^{PS} in equation (3.12) is non-singular at the origin the term in r is omitted from the polynomial $p(r)$.

The four conditions above are now used to solve for the parameters α, β, γ and δ. Conditions (i), (ii) and (iv) are translated by Kerker (1980) into three equations,

$$r_c^2 V_c + (l+1)^2 - r_c^2(E_l + D^2) = r_c^2 p''(r_c), \tag{3.13}$$

$$\ln(u_c / r_c^{l+1}) = p(r_c), \tag{3.14}$$

$$r_c D = l + 1 + r_c p'(r_c). \tag{3.15}$$

The prime denotes differentiation with respect to r. $u(r)$ is r times the atomic wave function, with $u_c = u(r_c)$ and $D = u'(r_c)/u(r_c)$. V_c is the value of the atomic potential at r_c and E_l is the atomic eigenvalue for angular momentum quantum number l. These are three linear equations for α, β and γ in terms of δ. To solve for δ condition (iii) for norm-conservation is used to yield the following equation,

$$2\delta + \ln I - \ln A = 0, \tag{3.16}$$

where,

$$I = \int_0^{r_c} dr r^{2(l+1)} \exp 2(\alpha r^4 + \beta r^3 + \gamma r^2) \tag{3.17}$$

and A is the amount of real charge that is contained within the core of the atom. This equation must be solved numerically for δ.

Once again the pseudopotential can be calculated by inverting the Schrödinger equation after the value of the parameters have been established. When these parameters are substituted into equation (3.12) the form of the pseudopotential is given by (for $r < r_c$),

$$V_l^{PS}(r) = E_l + \lambda(2l + 2 + \lambda r^2) + 6\beta r + 2\gamma \tag{3.18}$$

where,

$$\lambda = 4\alpha r^2 + 3\beta r + 2\gamma. \tag{3.19}$$

All that needs to be done now is to find the most favourable value for r_c. As before the natural place for the core radius is between the outermost node of the atomic wave function and the outermost extremum. At the outermost node it becomes impossible to satisfy the norm-conservation condition with the exponential form of $f(r)$ used so r_c must be taken towards the extremum. The exact position is dependent on the kink in the pseudopotential at r_c. Kerker (1980) uses the value of r_c which minimises the kink in $V_l(r)$ so that it converges quickly in Fourier space. This must be done separately to establish the optimum core radius for each angular momentum quantum number l. The HSC pseudopotential is smooth around r_c while the Kerker form will always retain some sort of kink at this point. This does not affect convergence directly in a plane wave calculation as the convergence properties of the wave functions are more important than those of the potential (see for example Rappe *et al*, 1990).

As the potential has different components for each angular momentum quantum number it is usually convenient to separate out a local part of the potential and have a set of non-local corrections to this, one for each value of l. As the local potential can be chosen arbitrarily it is easiest to take one of the l-dependent potentials for this. The non-local correction to this term is obviously zero everywhere. For instance if a magnesium pseudopotential is being created the s component could be taken as local. The three correction terms can then be formulated from this (with the $l = 0$ correction being zero everywhere).

3.3 Separable Pseudopotentials

The norm-conserving pseudopotentials produced by the two methods above accurately reproduce the scattering properties of the real ions. Depending on the choice of r_c a balance can be struck between softness of the potential and its transferability. If r_c is made large then the resulting pseudopotential is in turn very soft, however, less information about the ion core will be included and the transferability will thus be reduced. Alternatively a small r_c produces a pseudopotential that contains a great deal of information about the ion core, but this potential will be of a correspondingly hard core nature. Norm-conserving pseudopotentials do have one drawback over the more primitive types that they have replaced. The potential is now non-local in the angular momentum quantum number. This is not surprising as each component of angular momentum is orthogonalised with core wave functions of its own matching type. Effectively the s, p and d electrons all feel a different potential. This leads to problems when the pseudopotentials are used in Car Parrinello type programs.

The old Phillips and Kleinman (1959) pseudopotential was of the form,

$$V_{PK}^{PS} = \sum_c (E - E_c)|\phi_c\rangle\langle\phi_c|, \tag{3.20}$$

where E_c is a core-state eigenvalue. When the integral between the two plane waves $|e^{i\mathbf{k}\cdot\mathbf{r}}\rangle\langle e^{i\mathbf{k}'\cdot\mathbf{r}'}|$ from this is carried out it is proportional to,

$$\int j_l(kr)\phi_c(r)r^2dr \int j_l(k'r')\phi_c(r')r'^2dr' P_l(\cos\theta_{kk'}). \tag{3.21}$$

The j_l are spherical Bessel functions and $P_l(\cos\theta_{kk'})$ is the Legendre polynomial of the angle between the wave vectors k and k'. This requires the evaluation of only mn separate integrals for each ϕ_c. In other words only one integral is needed for each k (or $|\mathbf{k}+\mathbf{G}|$ in the plane wave method) in the calculation. Here n is the number of plane wave components c_G used and m is the number of special points in the Brillouin zone at which they are evaluated.

With conventional norm-conserving pseudopotentials, however, the equivalent form for the potential is,

$$V_{NC}^{PS} = \sum_{lm} |Y_{lm}\rangle V_l^{NC}(r)\langle Y_{lm}|. \tag{3.22}$$

Here the potential is non-local in the angular momentum quantum number and the spherical harmonics are necessary to project out the correct angular momentum dependence from the wave functions they operate on. For a given l the integral between two plane waves is now $\langle e^{i\mathbf{k}'\cdot\mathbf{r}} \sum_m |Y_{lm}\rangle V_l(r)\langle Y_{lm}|e^{i\mathbf{k}\cdot\mathbf{r}}\rangle$ and is proportional to (Kleinman and Bylander, 1982),

$$\int j_l(kr)V_l(r)j_l(k'r)r^2dr P_l(\cos\theta_{kk'}). \tag{3.23}$$

Now the number of integrals scales as $mn(n+1)/2$. As n is the number of wave function amplitudes c_G and in a Car-Parrinello calculation n can exceed 10000 the time taken to perform the evaluation becomes prohibitive. Kleinman and Bylander (1982) were originally interested only in reducing the inconvenient n^2

scaling in filling up the potential energy term for a matrix diagonalisation calculation. However, as this is a once and for all calculation the technique was little used. The time taken to diagonalise the matrix was usually considerably greater than that to calculate the matrix elements, no matter how badly this operation scaled. The Car-Parrinello type programs that we will be using require a slightly different calculation. In each iteration $\langle\phi|H|\phi\rangle$ must be evaluated. Much effort has been made to ensure that the rest of the calculation has a time scaling proportional to $n \ln n$ (the fast Fourier transform) at most. All the advantage of this method would be lost if any part of the calculation reintroduced a scaling proportional to n^2.

To regain a scaling proportional to n Kleinman and Bylander (1982) first separated out an arbitrary local potential to produce the standard form of the pseudopotential (this they christened *semi-local*),

$$V^{SL}(r) = V^{L}(r) + \sum_{l} \left(V_l^{PS}(r) - V^{L}(r)\right)\hat{\mathcal{P}}_l. \tag{3.24}$$

Here V^{SL} is the pseudopotential in semi-local form, V^{L} is the local potential that has no l-dependence, V_l^{PS} is the l-dependent norm-conserving pseudopotential and $\hat{\mathcal{P}}_l$ is the projection operator for angular momentum l. This can be abbreviated to,

$$V^{SL}(r) = V^{L}(r) + \sum_{lm} |Y_{lm}\rangle \Delta V_l \langle Y_{lm}|, \tag{3.25}$$

where ΔV_l is the correction term $(V_l^{PS} - V^{L})$. The scaling for operations involving the local part $V^{L}(r)$ are no trouble as (by definition) there is no l-dependence in this term. The problem is to write the semi-local correction term in a form that removes the n^2 scaling of any calculation in which it is involved.

Kleinman and Bylander chose to make this semi-local term fully non-local by

expressing it as,

$$V^{NL} = \sum_{lm} \frac{|\Delta V_l \phi_l^{ref} Y_{lm}\rangle\langle \phi_l^{ref} Y_{lm} \Delta V_l|}{\langle \phi_l^{ref}|\Delta V_l|\phi_l^{ref}\rangle}. \tag{3.26}$$

The ϕ_l^{ref} are the reference eigenfunctions for which the pseudopotential was calculated. It can be seen that if the calculation $\langle \phi_l^{ref}(r)Y_{lm}|V^{NL}(r)|\phi_l^{ref}(r)Y_{lm}\rangle$ is made this will then reduce (as it must) to its original form $\langle \phi_l^{ref}|\Delta V_l|\phi_l^{ref}\rangle$.

In reciprocal space the non-local part of the pseudopotential equation (3.26) now becomes,

$$V^{NL}(k,k') = \sum_l 4\pi(2l+1)P_l(\cos\theta_{kk'})\frac{I_l(k)I_l(k')}{I_l^S}. \tag{3.27}$$

The $I_l(k)$ and I_l^S are projection and scaling integrals respectively,

$$I_l(k) = \int_0^\infty dr r^2 j_l(kr)\phi_l^{ref}(r)\Delta V_l(r), \tag{3.28}$$

$$I_l^S = \int_0^\infty dr r^2 [\phi_l^{ref}(r)]^2 \Delta V_l(r). \tag{3.29}$$

In these equations $\phi_l^{ref}(r)$ is the radial part of the pseudo-wave function used to generate the pseudopotential component $V_l(r)$ and ΔV_l is the difference between this and the local potential $V^L(r)$ that has been separated out earlier. The integrals are now arranged in such a way that those concerning k are now separate from those with k' so that the scaling is once more proportional to n.

One problem exists with the use of norm-conserving pseudopotentials in the Kleinman and Bylander (KB) form. Gonze, Käckell and Schleffler (1990) showed that it was possible for a potential in the KB form to possess eigenstates below the true lowest eigenvalue of the atom. These *ghost states* are a purely mathematical artifact of the technique and have no physical significance. Obviously it is important that any potential that is to be used is free of these states. Close examination of the logarithmic derivatives of the KB potential is necessary to ensure that they are not present. If a ghost state appears in the logarithmic derivatives the potential must be reformulated in such a way that the state is

removed. Choosing the component with the ghost state to be the local one is an easy way to banish this quirk.

3.4 Optimisation of Pseudopotentials

The pseudopotentials we have now obtained are both transferable and efficient for non-local calculations. For many elements this is enough to allow their easy use in DFT calculations within the memory and speed limitations of computers. In order for this to be true it is obviously necessary to keep the number of plane waves needed by the calculation as small as possible. This is governed by the energy cut-off of the pseudopotential which is related to the cut-off of the potential and its wave functions in reciprocal space. In the Kerker (1980) type pseudopotential, for instance, there are two features that tend to make the potential cut off slowly in k-space. The potential has finite gradient at the origin which produces a cusp at this point. There is also a kink at $r = r_c$ as only the wave function and its first and second derivatives are continuous at this point. This kink is minimised to some extent by varying r_c until an optimum position is found. This is, however, the optimum point for minimising the kink in the potential at this point. No attempt is made to optimise the similar discontinuity in the third derivative of the wave functions at r_c.

These small problems are of little consequence to the pseudopotentials of well-behaved elements such as Mg. However, as pseudopotentials make use of core states to cancel out the rapidly oscillating parts of the valence wave functions, there are considerable problems with first row elements (such as O which has no core p electrons) and transition elements (which have sharply peaked valence states for the d electrons). In order to make realistic calculations on elements

such as these more effort must be made to reduce the energy cut-off.

In optimisation the basic method is always to push out r_c to make the potential softer. This will of course affect the transferability of the pseudopotential. In all cases there is this trade-off between optimisation and transferability. Two techniques have been proposed to tackle this problem. In one the Kerker method is adjusted to optimise the cut-off energy. In the other approach it is the wave functions themselves that are explicitly optimised with the potential formulated by the usual method of inverting the Schrödinger equation.

3.4.1 The Troullier and Martins Method

One scheme for producing softer pseudopotentials has been proposed by Troullier and Martins (1990 and 1991). The Kerker (1980) method for constructing pseudopotentials is taken as a starting point with extra conditions applied to the potential to reduce the energy cut-off by removing the cusp and kink. In total three extra conditions are used to achieve this.

(i) The pseudopotential is analytic at the origin by ensuring that the first derivative of the potential at the origin is zero. It is also desirable to make the second derivative of the potential zero as well to ensure that the pseudopotential is neither too deep or too shallow at the origin. These measures will remove the $r = 0$ cusp from the final pseudopotential.

(ii) In order to smooth out the kink at $r = r_c$ from the potential the third differential of the wave function is made continuous at the core radius r_c, rather than just the wave function itself and its first and second derivatives.

(iii) Similarly the fourth differential of the wave function is made continuous at r_c as well.

The shape of the analytic valence wave function $f(r)$ is taken as equation (3.10) as before. This time the polynomial part $p(r)$ is expanded a little to accommodate the extra parameters. Troullier and Martins (1990) used the following form for $p(r)$,

$$p(r) = c_0 + c_1 r + c_2 r^2 + c_3 r^3 + c_4 r^4 + c_5 r^5 + c_6 r^6 + c_7 r^7 + c_8 r^8. \qquad (3.30)$$

As before c_1 must be zero to make the pseudopotential non-singular at the origin. The new condition requiring analyticity of the potential at the origin forces c_3 to equal zero as well. The remaining parameters c_7 and c_8 are determined by applying the new continuity conditions in a similar way to before. From these parameters the full pseudopotential can be reconstructed as in the previous method.

In a later refinement Troullier and Martins (1991) suggested a slightly different form for $p(r)$ that produced an even softer pseudopotential to the one above. This time the polynomial $p(r)$ is taken in the following form,

$$p(r) = c_0 + c_2 r^2 + c_4 r^4 + c_6 r^6 + c_8 r^8 + c_{10} r^{10} + c_{12} r^{12}. \qquad (3.31)$$

Once more the parameters are evaluated from the conditions above and the pseudopotential reconstructed from them. In the paper (Troullier and Martins, 1991) there is also an extensive comparison between the energy cut-offs of both these techniques of optimisation and the Kerker (1980) and Hamann, Schlüter and Chiang (1979) methods that have gone before.

3.4.2 The method of Rappe, Rabe, Kaxiras and Joannopoulos

An alternative scheme for the optimisation of badly behaved pseudopotentials was put forward by Rappe *et al* (1990). The plane wave energy cut-off is linked to the cut-off in k-space of the pseudo-wave functions. The new approach is to correct a pseudo-wave function so that the kinetic energy that it possesses beyond an arbitrary cut-off in reciprocal space k_c is minimised. All that is then necessary is to ensure that the k_c chosen is sufficiently small for the calculation that is to be performed.

The pseudo-wave function (within a core radius r_c) is expressed thus,

$$\Psi_l(r) = \sum_{i=1}^{N} \alpha_i j_l(q_i r). \tag{3.32}$$

Here $\Psi_l(r)$ is the optimised pseudo-wave function and the $j_l(q_i r)$ are spherical Bessel functions. The wave vectors q_i are chosen so that their logarithmic derivatives match that of the all-electron wave function ϕ_l at r_c by imposing the condition,

$$\frac{j_l'(q_i r_c)}{j_l(q_i r_c)} = \frac{\phi_l'(r_c)}{\phi_l(r_c)}. \tag{3.33}$$

Lagrange multipliers are used to enforce normalisation and the continuity of two derivatives at r_c. The coefficients α_i are chosen to minimise the kinetic energy beyond the cut-off k_c. This energy is given by the equation,

$$T_{k_c} = -\int_0^{\infty} d^3r \Psi_l^*(r) \nabla^2 \Psi_l(r) - \frac{1}{(2\pi)^3} \int_0^{k_c} d^3k k^2 |\Psi_l(k)|^2, \tag{3.34}$$

where $\Psi_l(k)$ is the reciprocal space representation of the wave function. If this energy is sufficiently small the pseudopotential can be obtained once more by inversion of the Schrödinger equation.

The full procedure for formulating the optimised pseudopotential is to choose a value for r_c that ensures transferability. Choose a value for k_c and calculate the kinetic energy beyond this point. This value for k_c is then varied until only the tolerated amount of energy is found after the cut-off. In their paper Rappe *et al* (1990) suggest that the value of N is chosen to be 10 or even greater. More recently Lin *et al* (1993) have shown that it is often advantageous to restrict N to a value as small as 4 when trying to keep k_c as small as possible. This is because it is very difficult to minimise T in equation (3.34) if there are any Bessel function wave vectors q_i that are larger than k_c. If this is allowed to happen numerical instabilities occur and the resulting pseudopotential has strong short-wave oscillations. The normalisation condition requires that N be at least 4.

3.5 Implementation on Computer

The all-electron calculations and the generation of pseudopotentials by the HSC and Kerker methods were all performed using standard codes. These were written by Sverre Fröyen at the University of California at Berkeley in 1983. This is an extensive suite of programs that can do relativistic and non-relativistic all-electron calculations using a wide variety of approximations for the exchange and correlation energy. It can use the results of these all-electron calculations to generate pseudopotentials by Kerker method or recreate a HSC pseudopotential from the tables given in the paper by Bachelet, Hamann and Schlüter (1982). With little modification it could also be made to formulate Kerker-type pseudopotentials suitable for use with non-linear core corrections (see section 3.7). These programs produce output files of rV_l tabulated against r and $r\phi_l$ against r for each of the three angular momentum quantum numbers l. The codes used to produce optimised pseudopotentials by the Troullier method were provided by

the authors (Troullier and Martins) themselves. They work in a similar manner to the HSC and Kerker codes above.

The data provided by the HSC and Kerker (and Troullier) generation programs is converted into a Kleinman and Bylander (KB) form in reciprocal space for use by the CETEP program. A local potential is made by taking a fraction of each individual component of the norm-conserving pseudopotential. Usually this is all of one component and none of the other two. This is then subtracted from the individual pseudopotential terms to produce the non-local correction potentials. These are then transformed into the correct reciprocal space form by performing the integration in equation (3.28) to yield $I_l(k)$ on a grid of k values. Finally the integration in equation (3.29) is accomplished to calculate the scaling integrals I_l^S. All this data is then sent to file.

Two separate routines are needed to calculate the logarithmic derivatives of the wave functions. To make a proper comparison we must be able to display the logarithmic derivatives of the all-electron calculation (showing the scattering properties of the real atoms) along with those of the norm-conserving potentials (HSC and Kerker) and the KB form of the same pseudopotentials. If these are in agreement then the transferability of the pseudopotentials should be good. The same code can be used for the all-electron and the norm-conserving logarithmic derivatives. The special form of the separable KB pseudopotential requires a slightly modified calculation.

With the potential in the *semi-local* form $V^L(r) + \Delta V_l(r)$, for the all-electron and norm-conserving calculations, it is necessary to solve the Schrödinger equation to obtain the wave functions. This takes the form,

$$-\phi''(r) + \frac{l(l+1)}{r^2}\phi(r) + (V^L(r) + \Delta V_l(r) - E)\phi(r) = 0, \qquad (3.35)$$

where ϕ is r times the radial wave function. The Fröyen codes are used to integrate this equation out from $r = 0$ and it is an easy matter to obtain ϕ'/ϕ, the logarithmic derivative. This can be done over a range of energies E and for each l to produce the full energy dependence curves. The value of r up to which the integration is undertaken is specified by the user. This should be greater than the core radius of the pseudopotential r_c.

The logarithmic derivatives of pseudopotentials in the KB form require a slightly different calculation. The Schrödinger equation to be solved is now,

$$-\phi''(r) + \frac{l(l+1)}{r^2}\phi(r) + (V^L(r) - E)\phi(r) + \Delta V_l \phi_l^{ref} \lambda = 0, \tag{3.36}$$

where λ is given by,

$$\lambda = \frac{\int_0^\infty dr \phi_l^{ref}(r) \Delta V_l(r) \phi(r)}{\int_0^\infty dr \phi_l^{ref}(r) \Delta V_l(r) \phi_l^{ref}(r)}. \tag{3.37}$$

The ϕ_l^{ref} are the reference wave functions as before. The integration need only be performed as far as r_c in practice. Equation (3.36) must be solved self-consistently at each energy as λ depends on the form of $\phi(r)$. The local part of the potential, the scaling integral I_l^S (the denominator of equation (3.37)) and $\Delta V_l(r)\phi_l^{ref}(r)$ are calculated beforehand and stored in file. These are simply read into the integration subroutine to replace the relevant terms in the calculation. Typically it takes around five iterations before the factor λ is established for each energy.

To test the convergence of the pseudopotential against energy cut-off a further routine was used. As energy cut-off is the square of the reciprocal space cut-off k_c the kinetic energy of the wave functions against k_c is calculated. The full kinetic energy T is given by,

$$T = -\int d^3r \Psi_l^*(r) \nabla^2 \Psi_l(r). \tag{3.38}$$

We can write the wave function $\Psi_l(r)$ in terms of its Fourier components as,

$$\Psi_l(r) = \frac{1}{(2\pi)^3} \int dk \exp(ik \cdot r) \Psi_l(k). \tag{3.39}$$

When substituted into equation (3.38) this gives,

$$T = -\frac{1}{(2\pi)^6}\int d^3r \int d^3k \int d^3k' \exp(-ik'\cdot r)\Psi_l(k')(-k^2)\exp(ik\cdot r)\Psi_l(k), \quad (3.40)$$

which can be simplified to,

$$T = \frac{1}{(2\pi)^3}\int d^3k |\Psi_l(k)|^2 k^2. \quad (3.41)$$

The wave function (in reciprocal space) $\Psi_l(k)$ can be written as,

$$\Psi_l(k) = \int d^3r \exp(-ik\cdot r)\Psi_l(r). \quad (3.42)$$

This wave function can be divided into radial, $\phi_l(r)$, and spherical, $Y_{lm}(\hat{r})$, parts so,

$$\Psi_l(k) = \int d^3r \exp(-ik\cdot r)Y_{lm}(\hat{r})\phi_l(r). \quad (3.43)$$

A plane wave can be expanded in terms of spherical harmonics (see for example Pendry, 1974) according to the following relation,

$$\exp(i\mathbf{k}\cdot\mathbf{r}) = 4\pi\sum_{l,m} j_l(kr)Y^*_{lm}(\hat{r})Y_{lm}(\hat{k}). \quad (3.44)$$

Substituting this into equation (3.43) gives,

$$\Psi_l(k) = 4\pi\int d^3r \sum_{l',m'} j_{l'}(kr)Y^*_{l'm'}(\hat{r})Y_{l'm'}(\hat{k})Y_{lm}(\hat{r})\phi_l(r). \quad (3.45)$$

When the orthonormality relations for the spherical harmonics are applied this becomes,

$$\Psi_l(k) = 4\pi Y_{lm}(\hat{k})\int r^2 dr j_l(kr)\phi_l(r). \quad (3.46)$$

The integral part of equation (3.46) can now be written as $R_l(k)$ leaving,

$$\Psi_l(k) = 4\pi Y_{lm}(\hat{k})R_l(k). \quad (3.47)$$

Substituting for $\Psi_l(k)$ in equation (3.41) and simplifying gives,

$$T = \frac{2}{\pi}\int_0^\infty dk k^4 |R_l(k)|^2. \quad (3.48)$$

The wave function energy can now be evaluated by reading the wave function (in real space) from file. This is then Fourier transformed into reciprocal space. The kinetic energy of the wave function up to any cut-off k_c is given by the integral in equation (3.48) with the top limit changed to k_c.

3.6 Generation and Testing of Pseudopotentials

Norm-conserving pseudopotentials are generated to represent Mg ions in calculations. Both of the methods of construction discussed above are tried. Figure 3.1 shows the l-dependent components of the Hamann, Schlüter and Chiang (HSC) (1979) pseudopotential. This was obtained from the tables of HSC pseudopotentials found in the paper by Bachelet, Hamann and Schlüter (1982). To allow comparison the dotted line shows the value of $-2Z_v/r$ (the energy is in Rydbergs) i.e. the full bare-ion potential. As recommended by Bachelet, Hamann and Schlüter (1982) the ground state of magnesium ($3s^2$) was used to generate the potential and wave functions for the $l = 0$ component. For the $l = 1$ and $l = 2$ components the configuration $3s^{0.5}\ 3p^{0.25}\ 3d^{0.25}$ was used. The core radii used in the generation of this potential are 1.40 a.u. for the $l = 0$ term, 1.98 a.u. for the $l = 1$ term and 2.07 a.u. for the $l = 2$ term. They are soft around $r = 0$ and converge rapidly to the full potential close to the core radii.

Figure 3.2 shows the pseudo-wave functions that result from using the HSC potential. As required by the conditions of their generation they are smooth within the core radius, and have the single node at $r = 0$.

Convergence was tested by the method suggested by Rappe *et al* (1990) (see last section). The kinetic energy present in the various l-dependent wave functions was calculated at a variety of reciprocal space cut-offs k_c. Figure 3.3 shows the wave function kinetic energy plotted against the square of k_c. This is because k_c^2 is the energy cut-off used in calculations involving the pseudopotential. It can be seen that all three l-dependent parts converge rapidly to the maximum value (shown by the solid lines). The $l = 0$ term is the slowest to converge to

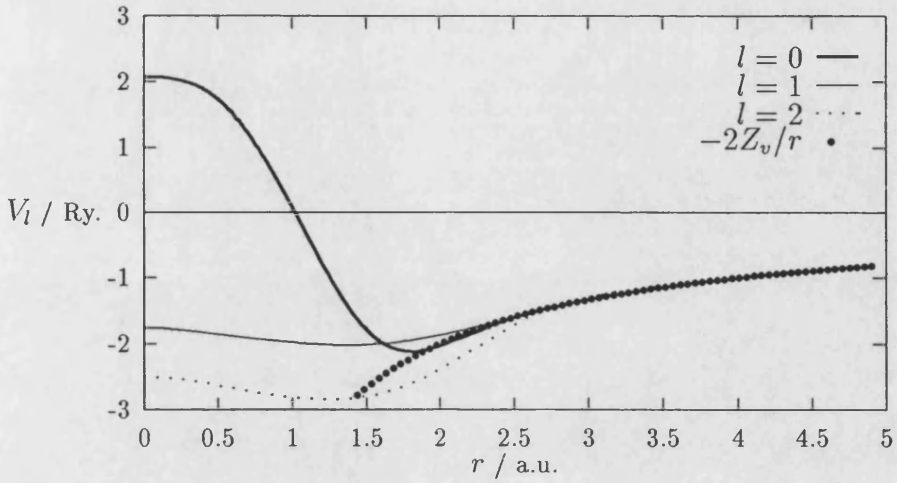

Figure 3.1: Mg pseudopotential generated using the Hamann, Schlüter and Chiang method.

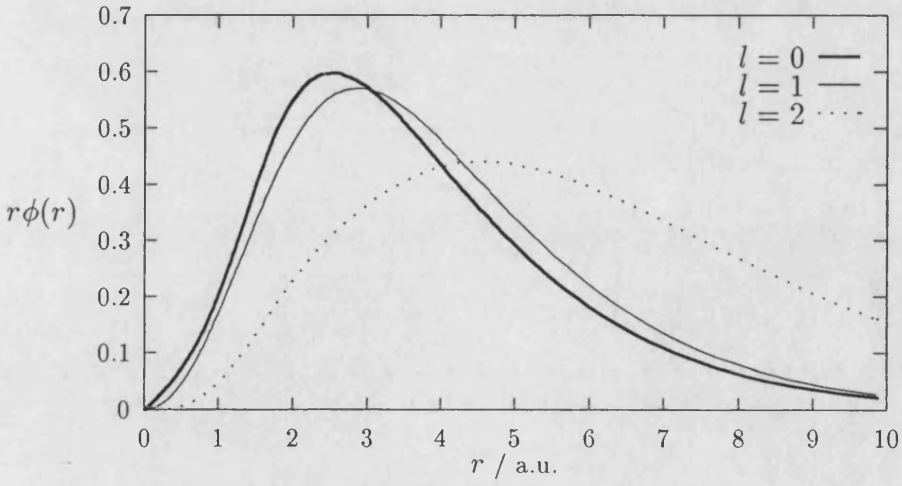

Figure 3.2: Pseudo wave functions of the HSC potential for Mg.

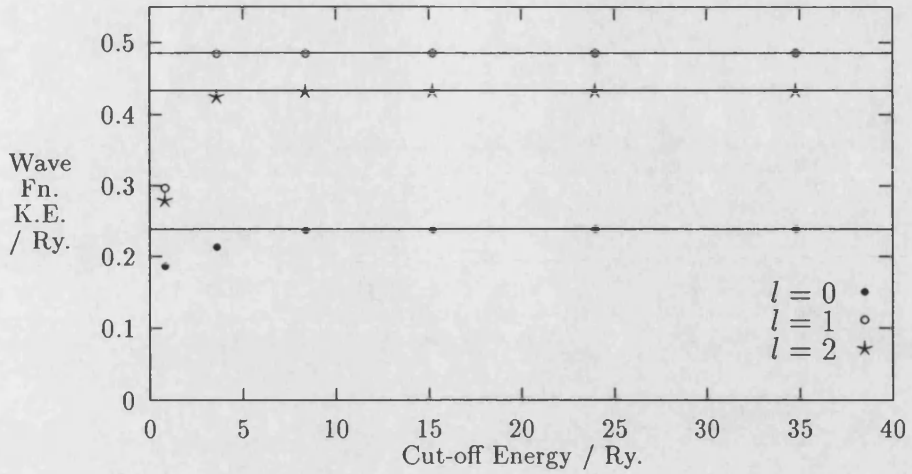

Figure 3.3: Kinetic Energy in (HSC) Wave Functions for Mg.

its maximum value. Even this looks to be fully converged before $\sim$ 15 Rydbergs (about 200 eV). A closer look at the data itself reveals that the kinetic energy is within 100 meV of the fully converged value for an energy cut-off of 75 eV. It closes to within 10 meV of this value for a cut-off of 140 eV, and is within 1 meV of convergence if a cut-off of 310 eV is used. Absolute convergence is not necessary in the calculations as it is energy differences that are important and these converge more rapidly than total energies. For a calculation using a HSC pseudopotential such as this one an energy cut-off of only $\sim$ 100 eV would be sufficient.

Figures 3.4, 3.5, and 3.6 show the energy dependence of the logarithmic derivatives of the $l = 0$, $l = 1$ and $l = 2$ pseudo-wave functions. The solid line (marked AE) shows the corresponding results for the true all-electron potential. The points marked HSC are for the potential generated by the Hamann, Schlüter and Chiang (1979) method and those marked KB are those resulting from the Kleinman and Bylander (1982) form of the same potential. The derivatives are

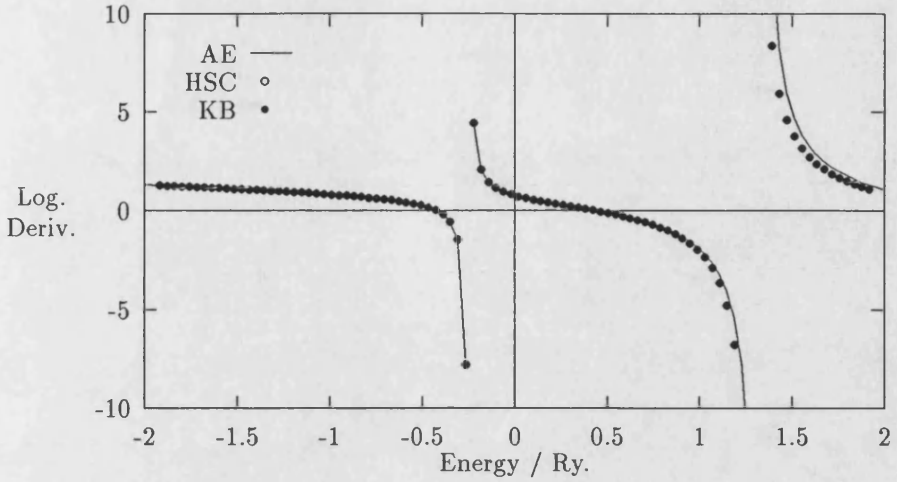

Figure 3.4: Logarithmic derivatives for $l = 0$ part of HSC potential for Mg.

calculated at $r = 5.0$ a.u. for all angular momentum quantum numbers. In all cases agreement is good between the All-Electron and pseudo-logarithmic derivatives over the energy range studied. The $l = 0$ component is taken to be local. This explains why the KB and HSC curves are identical for $l = 0$.

A magnesium norm-conserving pseudopotential generated by the rival method of Kerker (1980) is shown in figure 3.7. Once again the three l-dependent terms are shown by the lines, whilst comparison can be made with the coulomb potential represented by the dots. Identical atomic configurations to those used for the HSC potential ($3s^2$ for $l = 0$, $3s^{0.5}\ 3p^{0.25}\ 3d^{0.25}$ for $l = 1, 2$) were used to calculate the various components of the potential and their wave functions. The core radii used to formulate the potential by this method are 1.94 a.u. for the $l = 0$ term, 2.62 a.u. for the $l = 1$ term and 4.33 a.u. for the $l = 2$ term. Once again the potentials are soft about $r = 0$, although not as soft as those produced by the HSC technique. They converge rapidly to the full potential around the core radii. These radii are rather larger than their HSC equivalents. Figure 3.8 shows

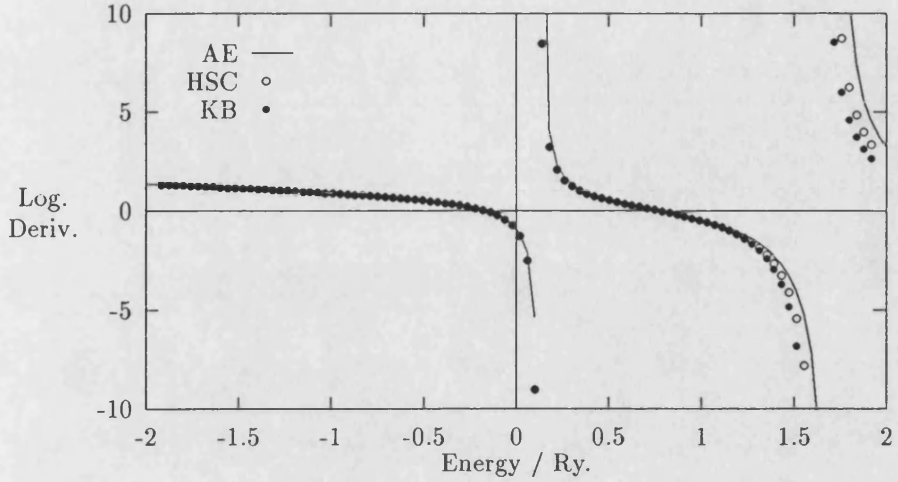

Figure 3.5: Logarithmic derivatives for $l = 1$ part of HSC potential for Mg.

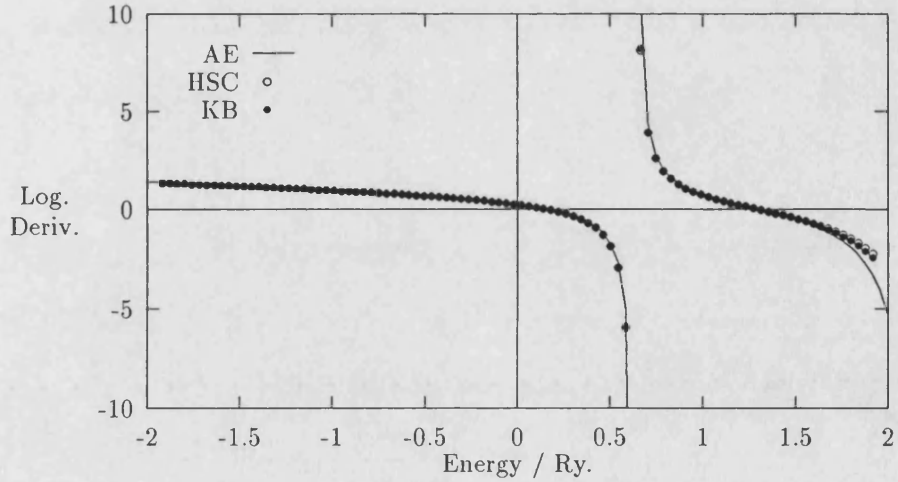

Figure 3.6: Logarithmic derivatives for $l = 2$ part of HSC potential for Mg.

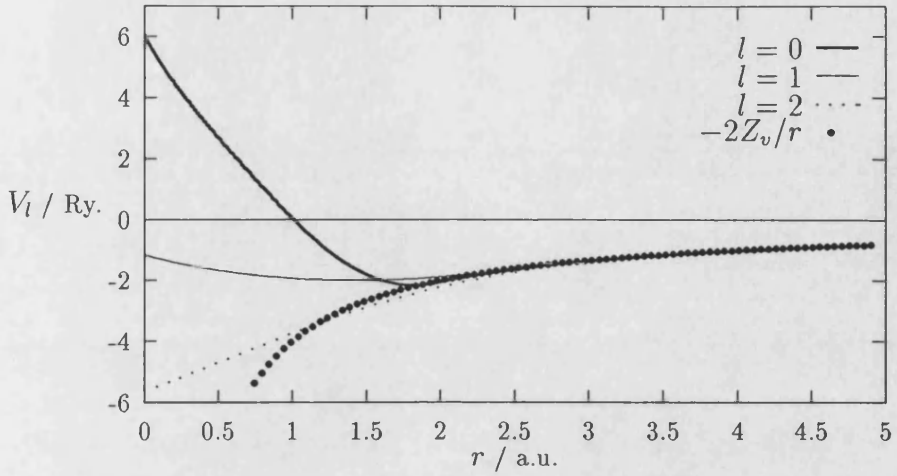

Figure 3.7: Mg pseudopotential generated using the Kerker method.

the pseudo-wave functions resulting from the Kerker potential. They are similar (though not identical) to their equivalent HSC wave functions. They have the same desirable properties.

As with the HSC potential previously the kinetic energy of the individual l-dependent wave functions was examined to establish the cut-off energy required to obtain the necessary degree of convergence. This is shown in figure 3.9. Once more it is the $l = 0$ component that is most sluggish in reaching its maximum value. Even this component is indistinguishable from the line for full convergence before a cut-off energy of $\sim$ 15 Rydbergs is reached (about 200 eV). This is approximately the same rate of convergence that the HSC potential demonstrated. Closer examination of the data for the kinetic energies reveals that the $l = 0$ term is within 100 meV if an energy cut-off of 100 eV is used. Convergence to within 10 meV is achieved with a cut-off of 140 eV, and the kinetic energy reaches to within 1 meV of its maximum value for an energy cut-off of 330 eV. These figures are similar to those for the HSC potential and a similar energy cut-off would be

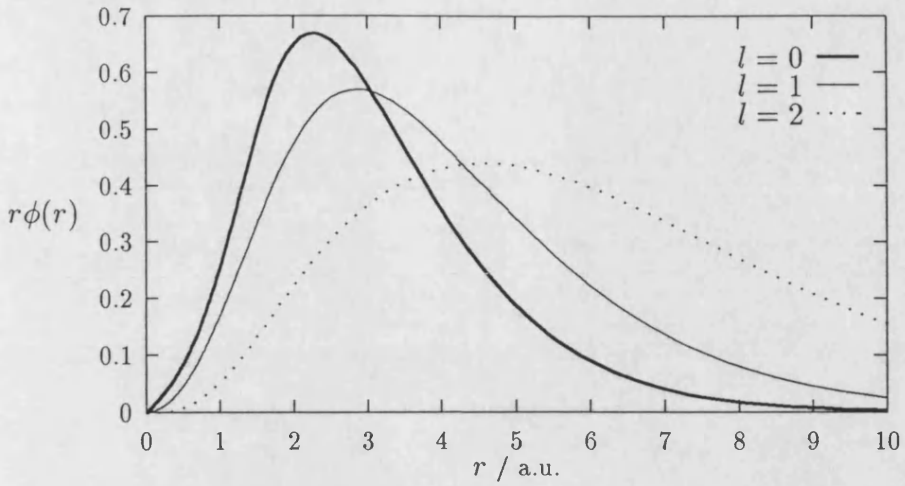

Figure 3.8: Pseudo wave functions of the Kerker potential for Mg.

sufficient for either potential.

Figures 3.10, 3.11 and 3.12 show the energy dependence of the logarithmic derivatives of the three l-dependent pseudo-wave functions. The derivatives are once again calculated at $r = 5.0$ a.u. for the three angular momentum quantum numbers. The key to the acronyms is as with the previous figures for the HSC logarithmic derivatives. Once again the $l = 0$ term is taken to be local and there is still good agreement between the pseudo-logarithmic derivatives and the all-electron curves.

Either of these two potentials would be suitable for use in this work. Both have energy cut-offs that are small enough to make the calculation feasible. The good agreement of their logarithmic derivatives with those of the all-electron calculation over a wide range of energies gives us confidence that the scattering properties of the ions will be correctly mimicked and that the pseudopotentials will be highly transferable.

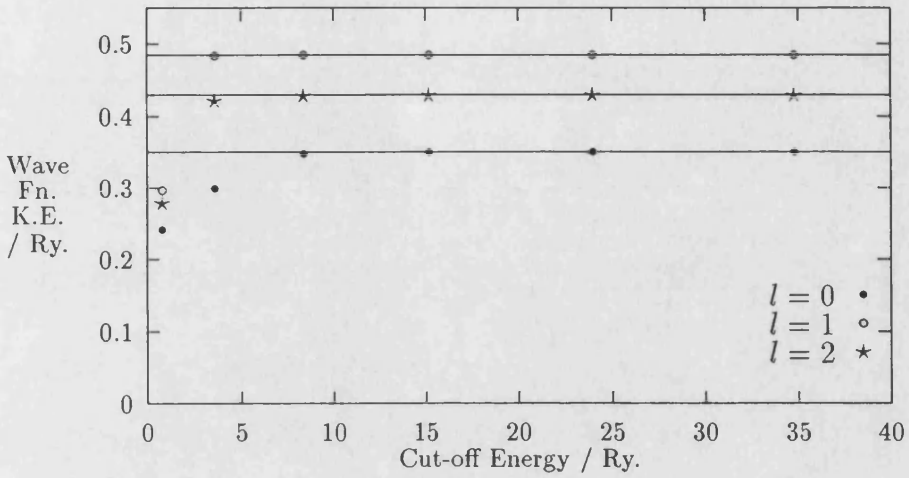

Figure 3.9: Kinetic Energy in (Kerker) Wave Functions for Mg.

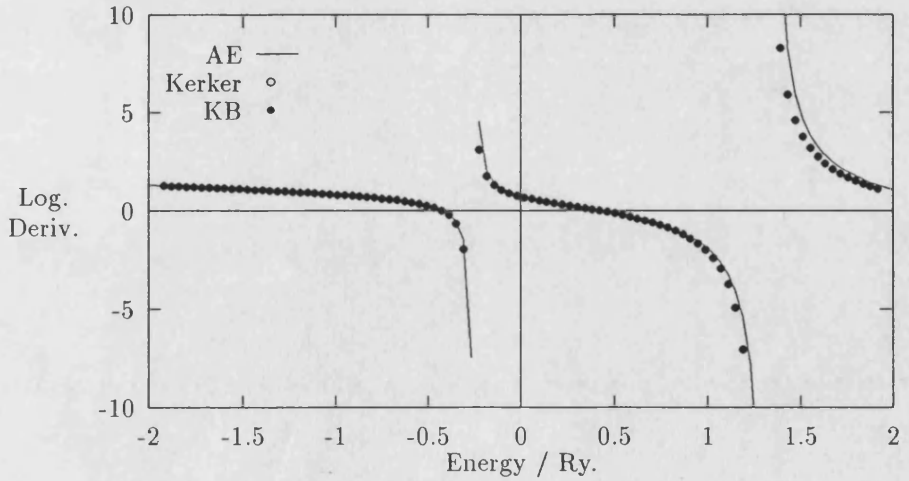

Figure 3.10: Logarithmic derivatives for $l = 0$ part of Kerker potential for Mg.

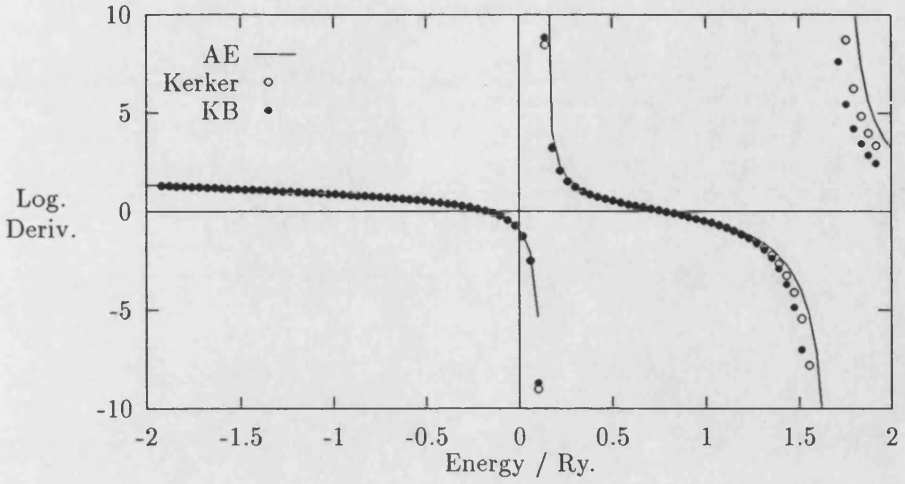

Figure 3.11: Logarithmic derivatives for $l = 1$ part of Kerker potential for Mg.

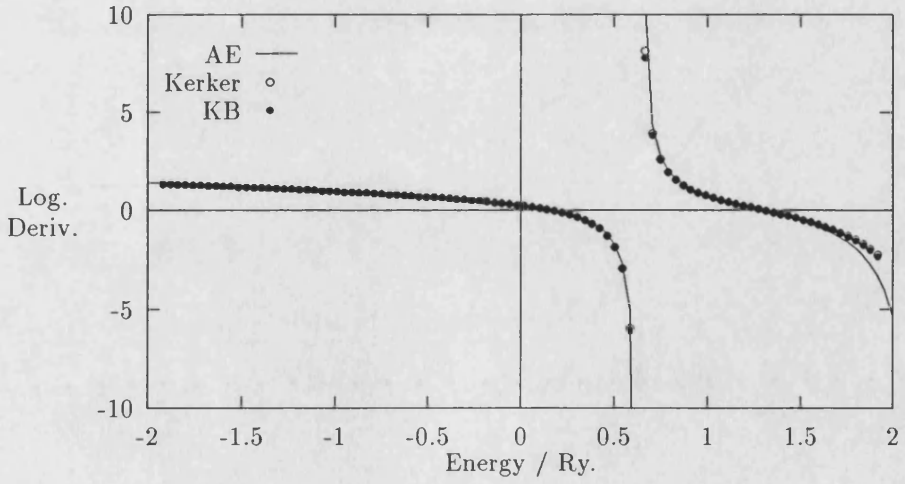

Figure 3.12: Logarithmic derivatives for $l = 2$ part of Kerker potential for Mg.

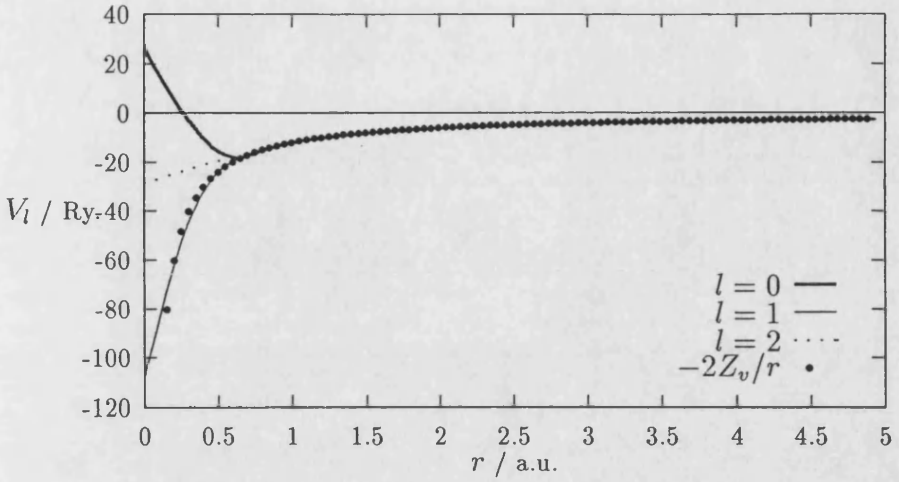

Figure 3.13: O pseudopotential generated by the Kerker method.

We now illustrate the problems of difficult atoms with reference to oxygen. An oxygen pseudopotential was formulated by the method of Kerker (1980). This is shown in figure 3.13. The electronic configurations used to derive the potentials and wave functions were those recommended in the paper by Bachelet, Hamann and Schlüter (1982). The $l = 0$ and $l = 1$ terms were generated from the oxygen ground state ($2s^2\ 2p^4$). The $l = 2$ term was obtained from the electronic configuration $2s^1\ 2p^{1.75}\ 3d^{0.25}$. The core radii used in its generation were 0.72 a.u. for the $l = 0$ term, 0.76 a.u. for the $l = 1$ term and 2.06 a.u. for the $l = 2$ term. These core radii are much smaller than those used in the generation of the magnesium pseudopotentials. The resulting oxygen pseudopotential (shown in figure 3.13) is correspondingly hard-core in nature. Comparison with figure 3.7 (the Kerker pseudopotential for magnesium) highlights just how hard the oxygen potential is around the origin. The $l = 1$ component reaches energies of ~ -110 Rydbergs at $r = 0$. This is twenty times greater than the corresponding magnesium term.

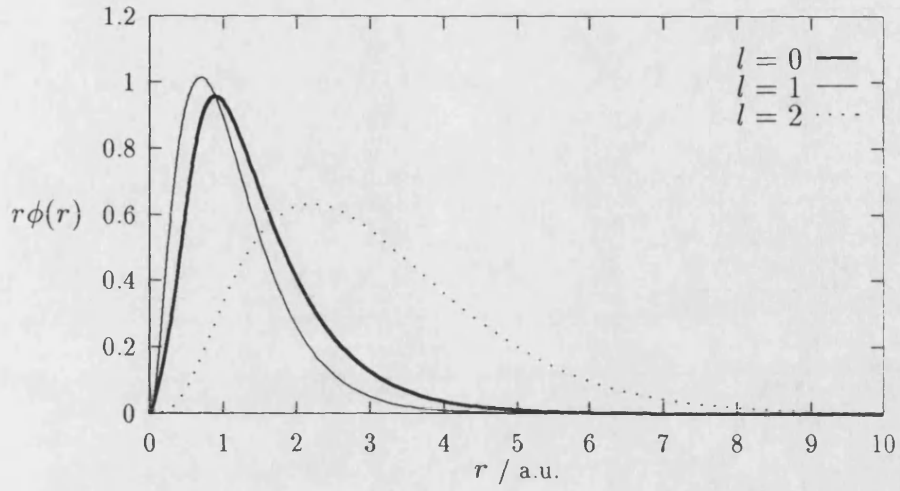

Figure 3.14: Pseudo wave functions of the Kerker method for O.

Figure 3.14 shows the pseudo-wave functions that result from using the Kerker potential. They are peaked much closer to the origin than the previous wave functions for magnesium. This is especially true for the $l = 0$ and $l = 1$ terms. It is because of this that the core radii used in the generation of this potential are so small resulting in its hardness around the origin.

Figure 3.15 plots the wave function kinetic energy of the Kerker oxygen pseudopotential against energy cut-off. The vastly expanded x-axis shows that this potential is very slow in converging indeed. The $l = 2$ is the best behaved. It looks to be close to its maximum value if a cut-off of around 20 Rydbergs (about 270 eV). Even though this value is large it is dwarfed by the cut-off energies required for convergence of the other two terms. The $l = 0$ component looks to be converged with a cut-off of 60 Rydbergs (about 800 eV) and although it is obviously approaching its maximum value the $l = 1$ component has still not truly converged with a cut-off of 140 Rydbergs (about 1900 eV). Examination of the data shows that even this figure is optimistic. In order for the $l = 1$ term

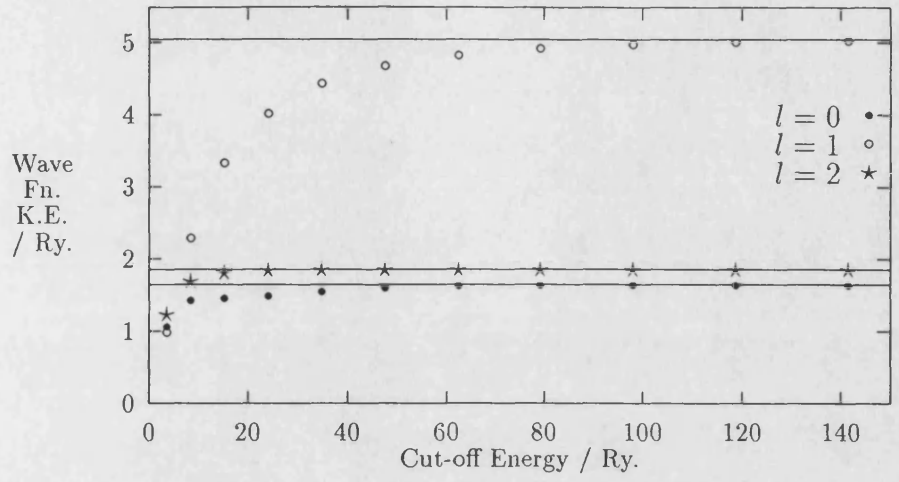

Figure 3.15: Kinetic Energy in (Kerker) Wave Functions for O.

to be within 100 meV of convergence an energy cut-off of $\sim$ 2800 eV must be used. This rises to 4500 eV if convergence to within 10 meV is required. Finally a staggering 7100 eV cut-off must be used to achieve convergence to within 1 meV.

Figures 3.16, 3.17 and 3.18 show the energy dependence of the logarithmic derivatives of the $l = 0$, $l = 1$ and $l = 2$ pseudo-wave functions. Once again the key to the acronyms is as before. The $l = 2$ term is taken as local in the KB calculation. Once more agreement with the all-electron data is very good.

An energy cut-off of several thousand electron-volts would be very inconvenient. Any program using this pseudopotential would require an enormous amount of memory to accommodate the wave functions, and the code would run exceedingly slowly. It is obviously desirable to try to optimise the pseudopotential into a form that would allow reasonable calculations to be made on the computer. The method of Troullier and Martins (1991) was tried in order to achieve this.

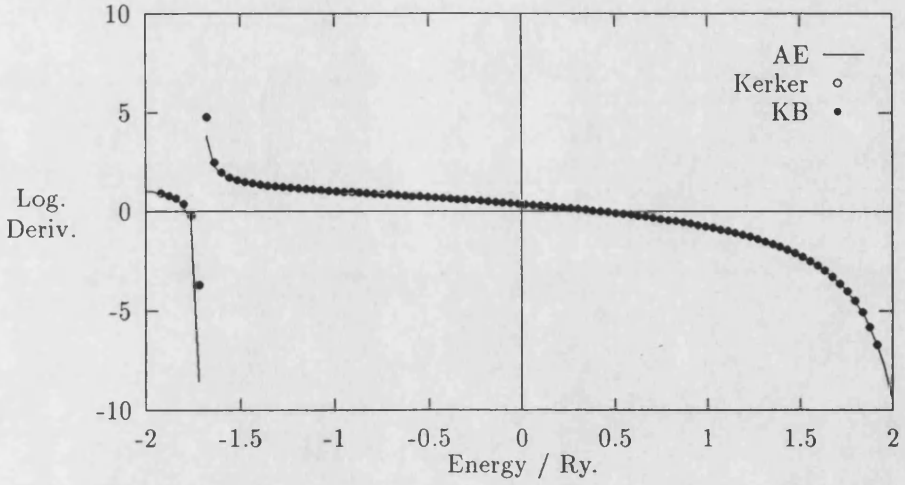

Figure 3.16: Logarithmic Derivatives for $l = 0$ part of the Kerker potential for O.

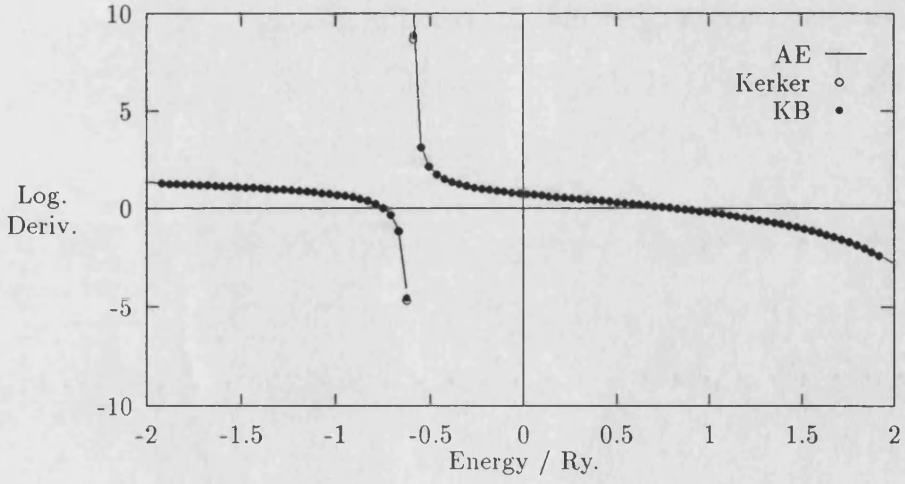

Figure 3.17: Logarithmic Derivatives for $l = 1$ part of the Kerker potential for O.

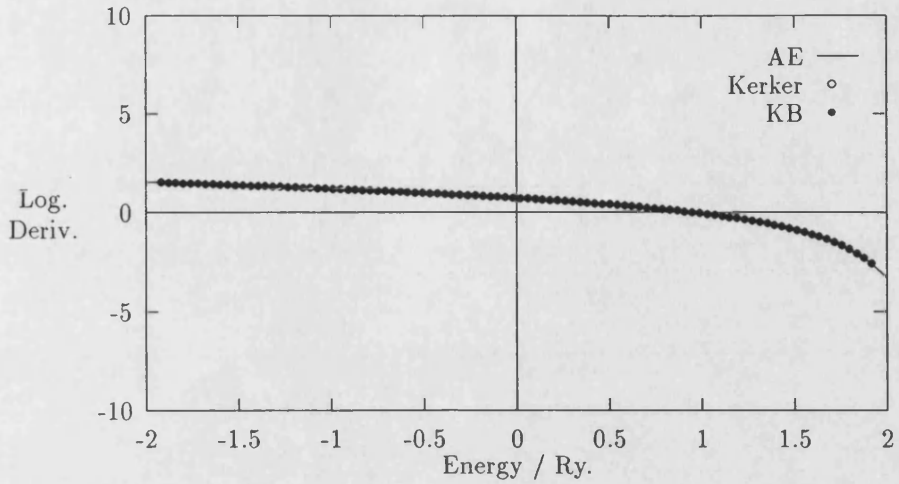

Figure 3.18: Logarithmic Derivatives for $l = 2$ part of the Kerker potential for O.

The $l = 0$ and $l = 1$ terms of the oxygen pseudopotential were optimised using the method of Troullier and Martins (1991). The $l = 2$ term was considered to be well enough behaved already and the standard Kerker potential was used for this. Figure 3.19 shows the resulting pseudopotential. The core radii for the two new potential terms were both set to 1.45 a.u. This is fairly substantially larger than the radii used to produce the Kerker potential. It can be seen that the potential is considerably more soft-core in character than the previous pseudopotential.

Figure 3.20 shows the pseudo-wave functions that result from using this Troullier potential. The peaks are now slightly further from the origin than for the previous Kerker pseudopotential. This has been made possible by the larger core radii for the $l = 0$ and $l = 1$ terms.

Figure 3.21 shows the convergence of the wave function kinetic energy for the Troullier oxygen pseudopotential. This is a great improvement on the convergence of the Kerker pseudopotential. The $l = 2$ component is still the best behaved

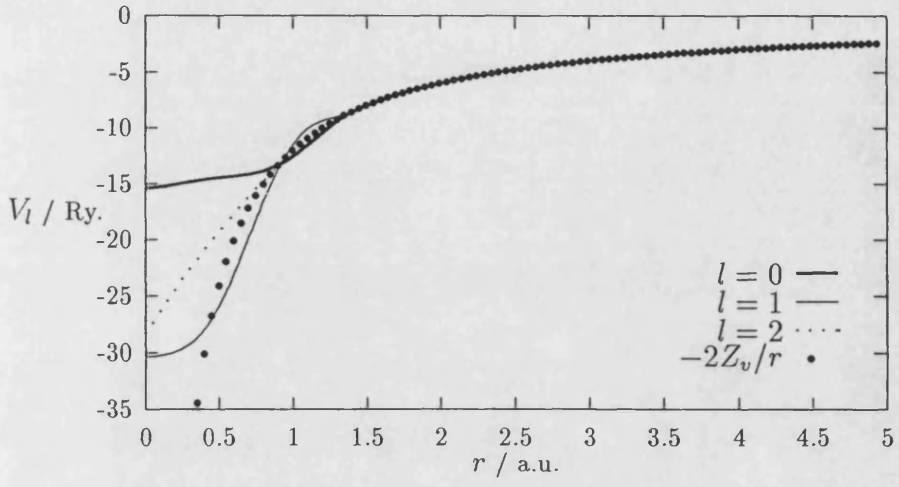

Figure 3.19: O pseudopotential generated by the Troullier method.

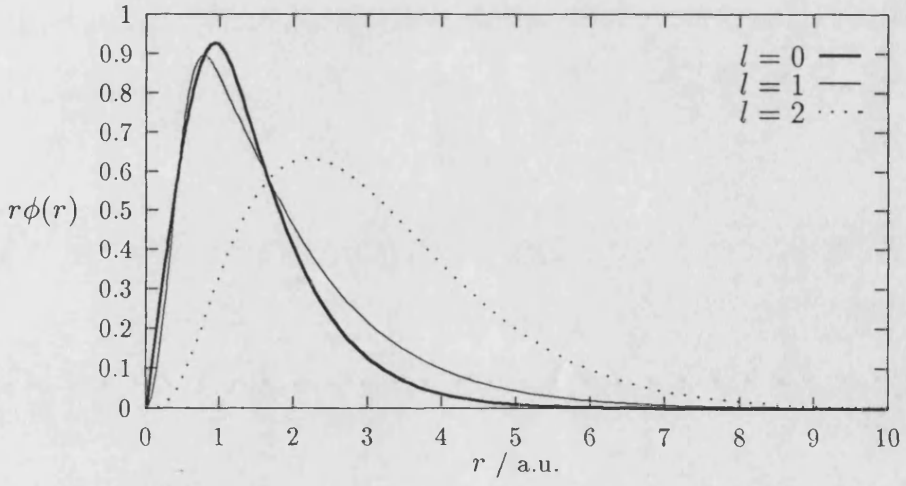

Figure 3.20: Pseudo wave functions of the Troullier method for O.

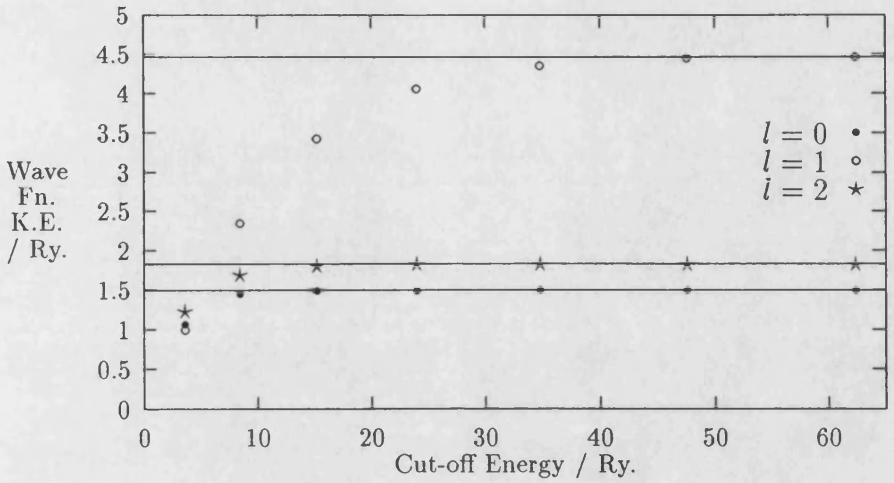

Figure 3.21: Kinetic Energy in (Troullier) Wave Functions for O.

with an energy cut-off of ~ 20 Rydbergs (about 270 eV) the same as before (this is unsurprising as it is the same potential). This time, however, the other two components are not so outrageously slow in following this term to convergence. The $l = 0$ term appears to have reached its maximum value for a cut-off of ~ 25 Rydbergs (about 340 eV) and the $l = 1$ term is properly converged with an energy cut-off of only ~ 60 Rydbergs (about 820 eV). Close inspection of the data reveals that this potential is within 100 meV of convergence if an energy cut-off of 710 eV is used. This rises to 820 eV for convergence to within 10 meV. Finally convergence to within 1 meV is achieved with an energy cut-off of 1580 eV.

Figures 3.22, 3.23 and 3.24 show the energy dependence of the logarithmic derivatives of the $l = 0$, $l = 1$ and $l = 2$ pseudo-wave functions. Once again the key to the acronyms is as before and the $l = 2$ term is taken to be local. Once more agreement with the all-electron data is good. There appears to have been very little loss of transferability in either the optimising of the pseudopotential or in

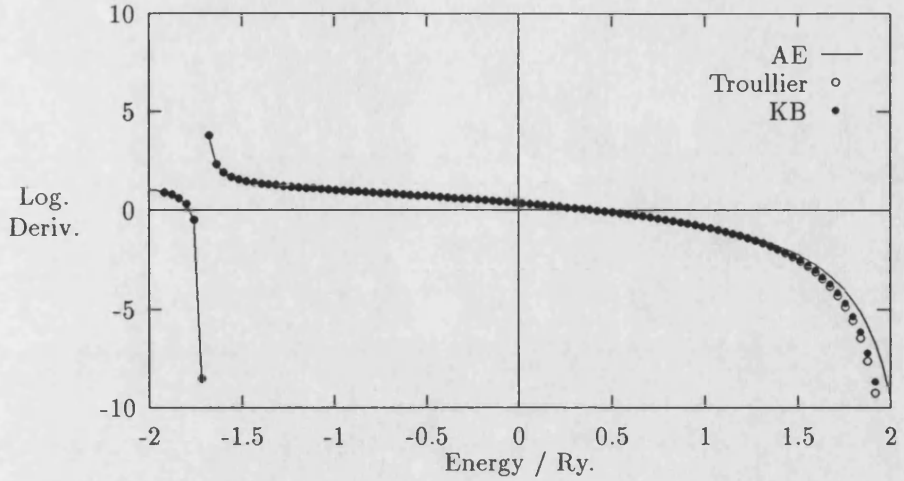

Figure 3.22: Logarithmic Derivatives for $l = 0$ part of the Troullier potential.

the use of the Kleinman and Bylander (1982) form. With logarithmic derivatives that are as good as these and the ability to use an energy cut-off of $\sim$ 1000 eV (or perhaps even less) this should be an excellent potential for our needs.

The alternative method of optimisation proposed by Rappe *et al* (1990) was also implemented for oxygen. This was done by Lin *et al* (1993). This potential, in the Kleinman and Bylander (1982) form with the $l = 2$ term taken as local, was tested and proved to have an energy cut-off of $\sim$ 1000 eV similar to that of the Troullier potential. As this potential was already being used successfully by other groups (see for example De Vita *et al*, 1992a and 1992b) this is the potential adopted for this work. The energy cut-off is now of a much more reasonable magnitude and it is possible to contemplate attempting real calculations using them. Further refinements to this technique have resulted in pseudopotentials with energy cut-offs of as little as 500 eV. As this is gained at least partially through a loss of transferability (as r_c is pushed further out) and the cut-off of 1000 eV is sufficiently small for useful calculations to be made already, these

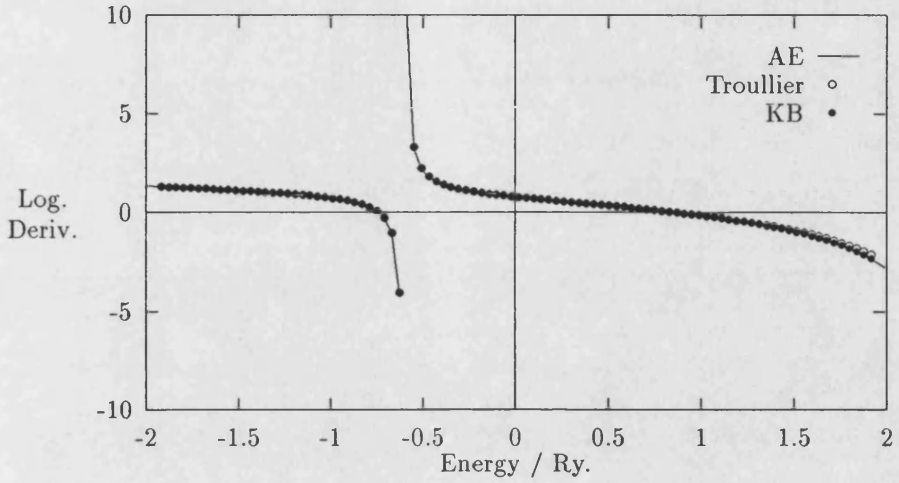

Figure 3.23: Logarithmic Derivatives for $l = 1$ part of the Troullier potential.

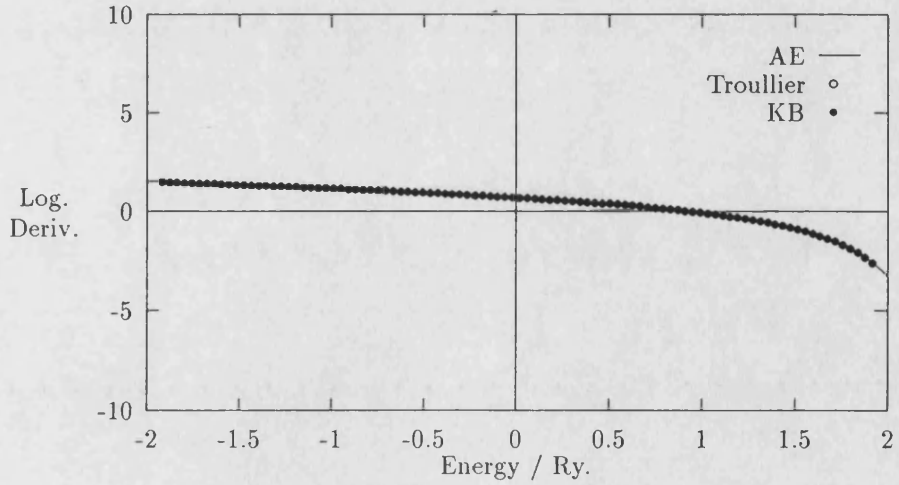

Figure 3.24: Logarithmic Derivatives for $l = 2$ part of the Troullier potential.

newer potentials have not been used.

In order to test these potentials in conjunction with the CETEP program a series of calculations are carried out involving single atoms in very large boxes. With the ions very far apart in real space the ions should be unable to form any bonds and will display the characteristics of isolated atoms. As all-electron calculations, that were used as the basis for the pseudopotential generation, are available with information on atomic eigenvalues and atomic charge densities it is a simple matter to compare these with the values computed by the CETEP code.

Figure 3.25 shows the comparison between the atomic pseudo-charge density about a magnesium atom from an atomic calculation (AT) and a full pseudopotential calculation (CETEP) involving a single magnesium atom in a large ($9 \times 10 \times 11$ Å) box. The large box is chosen to be of irregular side length to avoid symmetries and to provide $\rho(r)$ at as many points as possible. Its size must be great enough size to avoid bonding between magnesium atoms in adjacent boxes. The excellent agreement between the atomic curve and the pseudopotential points shows that not only is the box of large enough proportions but that the magnesium pseudopotential (a Kerker one in this case) can reconstruct the correct charge density very accurately. There is also good agreement in the eigenvalues of the magnesium atom calculated by these two different methods.

3.7 Non-linear Core Corrections

As we have seen in the previous chapter, the density functional theorem (DFT) gives the total energy of the ground state in terms of a functional of the total

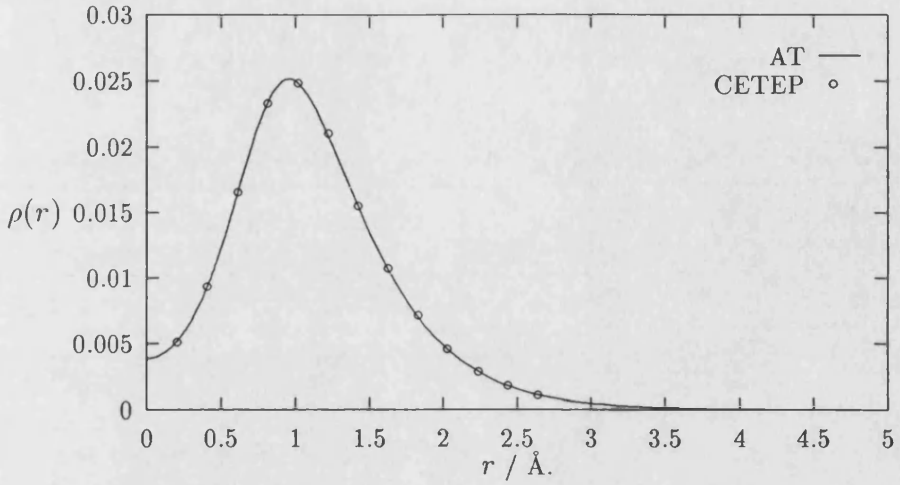

Figure 3.25: Charge density around single Mg atom (Kerker potential).

electron charge density,

$$E_{tot} = T[\rho] + E_{ion}[\rho] + E_{ee}[\rho] + E_{xc}[\rho]. \tag{3.49}$$

These terms represent the kinetic energy, the electrostatic interaction between the ions and the electrons, the Hartree interaction and the exchange and correlation energy respectively. The kinetic energy is obtained from the ∇^2 of the (single-particle) wave functions. The other three terms are given by,

$$E_{ion} = \int V_{ion}(\mathbf{r})\rho(\mathbf{r})d^3r, \tag{3.50}$$

$$E_{ee} = \frac{1}{2}\int \frac{\rho(\mathbf{r}')\rho(\mathbf{r})}{|\mathbf{r}' - \mathbf{r}|} d^3r' d^3r, \tag{3.51}$$

$$E_{xc} = \int \varepsilon_{xc}[\rho(\mathbf{r})]\rho(\mathbf{r})d^3r. \tag{3.52}$$

The final term for exchange and correlation energy is represented by the local density approximation (LDA) which is non-linear in the charge density. In the pseudopotential approach the charge density is divided between the core and valence contributions. The core density is assumed to be frozen around the ion sites and its contribution is ignored. The charge density in equations (3.50) to

(3.52) is replaced by the (pseudo) valence charge density and all interactions between the core and valence electrons are transferred to the pseudopotential that replaces V_{ion}. This can cause problems with the non-linear exchange and correlation term if the core and valence electrons are not well separated. If this is the case then systematic errors will creep into the total energy calculation. We will see later that these errors can be very important for the systems that we are investigating.

Louie, Fröyen and Cohen (1982) attempted to solve this problem, which they found was important for alkali metals and magnetic systems. As this effect is only present in the exchange and correlation term of the energy they decided to include the core charge with the valence charge whenever this term is calculated. This core charge density is easily obtained from the all-electron calculation. It can then be stored away in a similar manner to the potential. As the core will remain unchanged it is necessary to read this data in only once and then add it to the pseudo-charge density when needed for the evaluation of the exchange and correlation energy. This approach has problems if the ions are allowed to move in the calculation as the core charge distribution would have to be recalculated after every evolution. However, it is not necessary to have the ions change position in our calculations so this problem can be ignored.

There is one further complication in this process. As we are using a plane wave method to describe the wave functions it is impractical to use the full core charge density. This density possesses some very high Fourier components which we would prefer to avoid if it is not to make our programs very large and slow. It is possible to avoid this by noting that the core charge has significant effect only where the core and valence charge densities are of similar magnitudes (Louie *et al*, 1982). It is unnecessary, therefore, to use the real core density close to

the nucleus where most of the charge resides. Some radius r_0 is chosen beyond which the true core charge is used. Within r_0 the core charge is replaced by a function that matches the core charge ar r_0, which Fourier transforms easily, and which contains the smallest possible integrated charge density. Louie *et al* (1982) suggest the use of the function,

$$\rho^c_{partial}(r) = A\sin(Br)/r \tag{3.53}$$

for this task. The two parameters A and B are used to match the value and the gradient of the core charge density at the point r_0. Tests carried out by Louie *et al* (1982) showed that r_0 could be chosen as the radius at which the core density is between one and two times larger than the pseudo-valence charge density.

The condition that the core charge density and the valence charge density are overlapping significantly should not be met in most instances. When this occurs it is a simple matter to extract the core density (and modify it as above) and produce an amended potential. For example figure 3.26 shows a magnesium pseudopotential (of the Kerker type) that has been generated for use with non-linear core corrections. Figure 3.27 shows the partial core charge density that would be used in conjunction with this.

The usual atomic configuration of magnesium ($3s^2$ for $l = 0$, $3s^{0.5}\ 3p^{0.25}\ 3d^{0.25}$ for $l = 1, 2$) was used in the generation of this pseudopotential. The core radii for the various angular momentum quantum numbers were 1.94 a.u. for the $l = 0$ term, 2.62 a.u. for the $l = 1$ term and 4.33 a.u. for the $l = 2$ term. These are identical values to those used with a normal Kerker potential. The radius r_0 used in the formulation of the partial core density was 1.59 a.u.

By comparing figure 3.26 with figure 3.7 it is possible to see some changes between the straight Kerker pseudopotential and a Kerker potential amended for use with

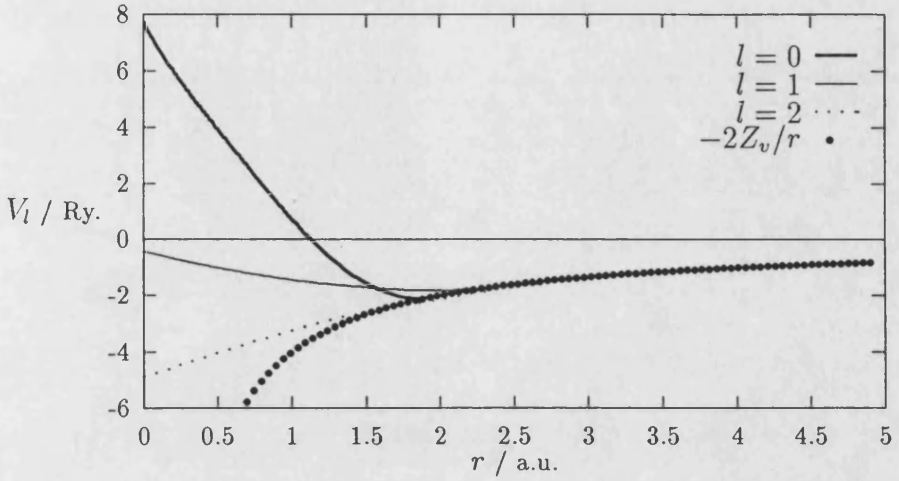

Figure 3.26: Mg pseudopotential with core corrections.

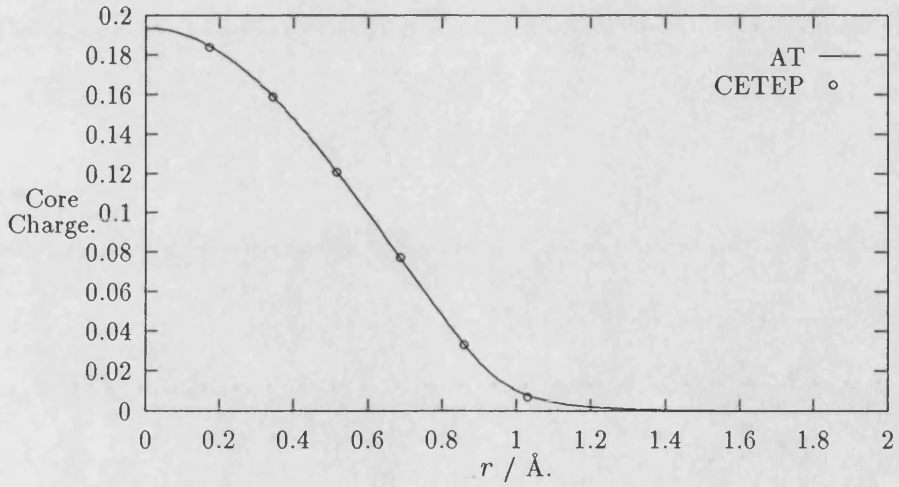

Figure 3.27: Partial core density for Mg.

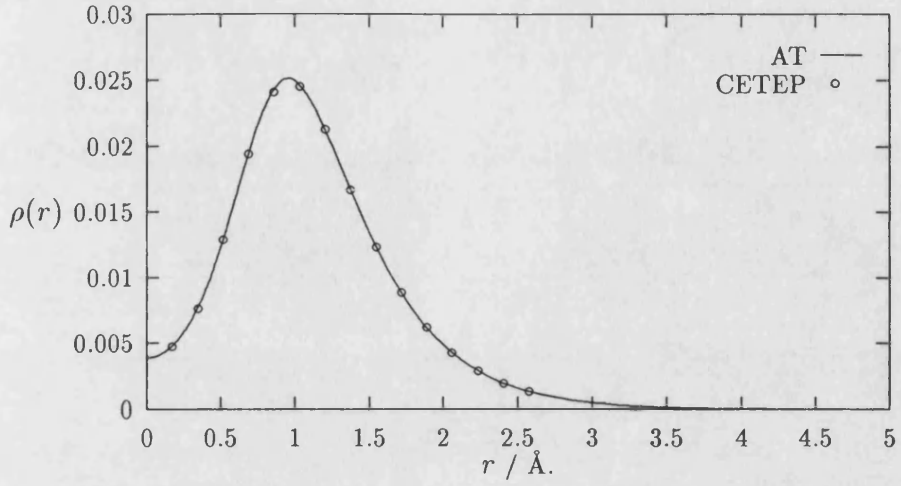

Figure 3.28: Charge density around single Mg atom with core corrections.

core corrections. These small differences persist until r is about 2 Å after which the potentials are indistinguishable. The wave functions (and their logarithmic derivatives with energy) are also identical.

Finally this new magnesium potential was tested in a large irregular box as before. Figure 3.27 demonstrates that the core charge density is correctly reconstructed by our modifications to the CETEP program. Figure 3.28 shows the resulting pseudo valence charge density that is calculated using this potential and with the use of the non-linear core corrections. Once more the atomic pseudo-charge density is reproduced extremely well by the pseudopotential and the CETEP program. If there is an occasion to use core corrections then we can have confidence that they are correctly simulating the atom in question.

3.8 Summary

The norm-conserving pseudopotentials of Hamann, Schlüter and Chiang (1979) or Kerker (1980) are excellent schemes for representing the potential V_{ext} felt by the electrons due to the ion cores. They successfully reproduce the scattering properties of the ions themselves over a wide range of energies and are fully transferable. For computational efficiency they can be expressed in the Kleinman and Bylander (1982) form with little loss of transferability. Badly behaved ions, such as oxygen in our example, can be more easily handled when the optimisation techniques of Troullier and Martins (1990 and 1991) or Rappe *et al* (1990) are used.

Pseudopotentials of the types above have been successfully generated for magnesium and oxygen. Testing has shown that they possess the properties that we desired and they should be well suited to use in *ab initio* total energy calculations. The optimisation of the oxygen pseudopotential has been particularly effective. The cut-off energy has been reduced to $\sim$ 1000 eV which is small enough to allow reasonable calculations to be made. The transferability does not seem to be badly affected by this.

Chapter 4

MAGNESIUM OXIDE

For the reasons outlined in chapter 1 magnesium oxide is the material initially selected for analysis. In this chapter MgO will first be introduced. A comparison of the previous attempts to calculate its properties will then be given. The set-up for the calculations is described next, followed by the equilibrium properties derived from these calculations. If these equilibrium properties are in good agreement with experiment the high pressure properties will then be calculated. Finally the charge density (both at equilibrium and under strain) is examined in order to investigate the bonding of MgO.

4.1 Introduction

Alkaline earth-metal oxides are technologically important materials. They have high melting points, low coefficients of expansion and small thermal conductivities. These parameters make them good candidates for applications as, for example, substrates for thin-film growth, optical materials and in microelectronics. They also have uses in catalysis.

Magnesium oxide is also important in its own respect. It is a major constituent of the Earth's lower mantle (along with magnesium silicon oxide). Its properties at the high pressures within the mantle (up to about 1.4 MBar) are of considerable interest to geophysicists and geologists. Unfortunately experimental data on MgO in these conditions is difficult to obtain. The behaviour of MgO at relatively low pressures (up to 10 kbar) has been investigated by Chang and Barsch (1969) using an ultrasonic pulse method. They were able to measure the individual elastic constants of MgO at these pressures. From these they went on to calculate the pressure dependence of the bulk modulus and the elastic constants. Data at greater pressures has been obtained by Mao and Bell (1979). Using X-ray diffraction results from MgO in a diamond window high pressure cell they measured the relative change in unit cell volume at pressures up to 1.0 Mbar. From this they calculated the equation of state of MgO at these pressures. Their work was sufficient to show the change in bulk modulus with pressure but not to isolate individual elastic constants. If an *ab initio* calculation could be trusted to produce accurate results at pressures up to 1.4 Mbar this would shed light on an area of the behaviour of MgO that experimentalists have found difficult to penetrate.

There are also good reasons for studying the electronic structure of magnesium oxide. Experimental results for MgO at equilibrium (see Anderson and Andreatch, 1966, for example) indicate that there is a violation of the Cauchy condition. In other words the elastic constants C_{12} and C_{44} are not equal as a simple pairwise interaction model of the solid would imply. MgO is not as simple an ionic solid as NaCl in which C_{12} is very close to C_{44}. Obviously we hope that this property is correctly reflected in our calculations. We also wish to try to understand the mechanism behind this so that empirical models can properly take account of the effect. There are several possible mechanisms which could be used by empirical

modellers to explain the source of the violation in ionic crystals. These include three body effects such as angle-bending forces (see for example Au and Weidner, 1986), next nearest neighbour forces (Davies, 1981), the deformable ion model (Weidner and Price, 1988) and the breathing shell model (Schröder, 1966, and Boyer *et al*, 1985). The latter two of these effects are thought to be the most important.

According to the deformable ion model when the unit cell is placed under strain the charge density will try to maintain its volume at the expense of distorting its shape. This leads to the elastic constant C_{12} being greater than C_{44} and hence the sign of the Cauchy violation, $C_{12} - C_{44}$, is positive. Alternatively the charge cloud around the ions might try to remain spherical at all times, even when the unit cell is strained. In this case the charge density attempts to maintain its shape at the expense of changing its volume. The charge cloud remains spherical at all times but its volume varies with that of the unit cell. The charge density is said to *breathe*. This leads to the elastic constant C_{12} being smaller than C_{44} and this time the sign of the Cauchy violation is negative. A summary of the relevant elastic theory is given in the appendix at the end of this chapter.

The latter is the assumption behind the *Potential Induced Breathing Model* used to study MgO by Isaak, Cohen and Mehl (1990). By analysing MgO charge densities at equilibrium and under a variety of different strains and unit cell volumes it should be possible to see if there is any evidence for either of these mechanisms at work. The equilibrium charge density can also be studied to discover the ionicity of MgO. Previous work (for example the Hartree-Fock calculations of Causa *et al*, 1986) have taken MgO to be almost entirely ionic in character with the Mg ion having a charge very close to +2.0.

4.2 Previous Work on Magnesium Oxide

One of the benefits of studying magnesium oxide is that it enables a comparison to be made between calculations made using the CETEP code and those made by other *ab initio* or empirical methods. In the past at least seven different methods have been used to analyse the properties of MgO. These will give us an important yardstick by which we can judge the success of the CETEP codes in calculating total energies.

Isaak, Cohen and Mehl (1990) used an empirical technique, the potential induced breathing model (PIB), to simulate MgO. Other groups have tried a variety of *ab initio* methods with the same object. Causa, Dovesi, Pisani and Roetti (1986) have used Hartree-Fock (HF); Cohen and Gordon (1976) tried a modified electron gas (MEG) theory; Mehl, Cohen and Krakauer (1988) used linearised augmented plane wave (LAPW) calculations; McCammon, Brown and Meagher (1990) used molecular orbital (MO) calculations; Chang and Cohen (1984) made an early use of pseudopotentials (PP) as have De Vita *et al* (1992a and 1992b) more recently. Some of the basic physical properties resulting from these calculations are summarised in table 4.1 along with the results obtained in this thesis. For comparison the experimental values of these parameters are shown also. These figures are taken from the papers by Durand (1936); Susse (1961); Chung (1963); Bogardus (1965); Anderson and Andreatch (1966); Spetzler (1970) and Markland and Mahmoud (1971). The values quoted are averages of all these results made by Hearmon (1979) and are for MgO at room temperature (~300 K). Investigation of the temperature dependence of the elastic constants by Durand (1936); Susse (1961); Anderson and Andreatch (1966) and Markland and Mahmoud (1971) show that there is little change in their value as the temperature is extrapolated back towards absolute zero. This is good as the theoretical methods make their

	a_0/Å	B/GPa	C_{11}/GPa	C_{12}/GPa	C_{44}/GPa
expt	4.21	160	294	93	155
PIB[a]	4.21	182	308	119	188
MO[b]	4.60	104	228	42	154
MEG[c]	4.08 - 4.58	169 - 292	223 - 509	126 - 221	126 - 221
HF[d]	4.20	186	-	-	-
LAPW[e]	4.17	172	-	-	-
PP[f]	4.19	146	-	-	-
PP[g]	4.17	154	-	-	-
PP[h]	4.23	163	303	92	139

[a] Isaak, Cohen and Mehl, 1990.
[b] McCammon, Brown and Meagher, 1991.
[c] Cohen and Gordon, 1976.
[d] Causa, Dovesi, Pisani and Roetti, 1986.
[e] Mehl, Cohen and Krakauer, 1988.
[f] Chang and Cohen, 1984.
[g] De Vita *et al*, 1992a and 1992b.
[h] This work.

Table 4.1: Comparison of previous MgO calculations.

predictions of the physical properties of MgO at 0 K. There is, however, a marked fall-off in the value of the elastic constants when the temperature is increased above 300 K. As might be expected, there is a small spread in these parameters amongst the different sources. For example the value of C_{11} ranges between 289 GPa (in the paper by Chung, 1963) and 302 GPa (from the work of Susse, 1961). Both of these are around 2% away from the average value used by Hearmon. Although most of the other values for C_{11} are rather more tightly grouped around the mean it will be difficult to accurately quote errors from theoretical results that are within a few percent of the average value.

Neglecting, for the moment, the pseudopotential calculations of De Vita *et al* (1992a and 1992b) and this thesis, it can be seen from table 4.1 that most of the techniques make good predictions for the lattice parameter of MgO. Four of the

methods give results that are within 1% of the experimental value. The molecular orbital technique of McCammon, Brown and Meagher (1990) is a rather more disappointing 9.3% too large. Cohen and Gordon (1976) provide a range of answers from their modified electron gas calculation depending on which wave functions they have chosen to represent the charge cloud around the oxygen ions and how many nearest neighbours they they allow to interact. In contrast, the values calculated for the bulk modulus of MgO are not as successful. No technique manages to approach closer than 7.5% away from the experimental result. The four methods that gave good values for the lattice constant produce bulk moduli that are between 7.5% and 16.3% in error. As might be expected from its performance earlier the MO calculations are even further from experiment. Somewhat ironically the wave functions that produced the best lattice parameter in MEG calculations were responsible for the least accurate values of the bulk modulus. Only three of the techniques made any attempt to derive the individual elastic constants. The PIB model makes a creditable stab at C_{11}, but is much more inaccurate for C_{12} and C_{44}. The MO method is a long way from the experimental values of C_{11} and C_{12}. It can only be by pure fluke that the value for C_{44} was so close as all the other results from this method were so poor. Finally the MEG calculations provide us, once again, with a wide range of possible values for the elastic constants. Although the experimental value for C_{11}, say, is straddled by the calculations, none of the answers are in the region of the experimental value itself. It is interesting to note that in all cases the value calculated for C_{12} is equal to that calculated for C_{44}. In other words there is no violation of the Cauchy condition for MEG calculations.

Other theoretical work has been done on magnesium oxide that is of less interest to us. Pandey, Jaffe and Kunz (1991) used Hartree-Fock calculations to produce the band structure and density of states of MgO (along with CaO and SrO). As

we make no attempt to do this ourselves we can make no comparison with their results. Xu and Ching (1991) used an orthogonalised linear combination of atomic orbitals technique (OLCAO) to generate the same features. They also went on to produce charge distributions (in real space) with which we can compare our work.

There is one further piece of theoretical work that is of interest. De Vita *et al* (1992a and 1992b) made calculations of the lattice parameter and bulk modulus of MgO as a prelude to making predictions of the defect energies of vacancies in MgO. This work was carried out using the same CETEP codes that will be used in this work, and with very similar potentials. Their results showed the lattice parameter to be 4.17 Å, and the bulk modulus to be 1.54 Mbar. These were achieved using energy cut-offs of between 600 and 1000 eV and four special k-points in the Brillouin zone selected according to the scheme of Monkhorst and Pack (1976). It is to be expected that the results of this work will be very close to those of De Vita *et al* (1992a and 1992b).

Clearly there is much room for improvement in the calculation of the physical properties of MgO at equilibrium. Both empirical and *ab initio* techniques fail to convincingly mimic the experimental results for all but the simplest test, that of predicting the lattice constant. If we are to make calculations of the properties of MgO at high pressure that can be considered in any way reliable we must first calculate results for equilibrium MgO that are very much closer to experiment than has hitherto been achieved.

4.3 Set-up on Computer

The pseudopotentials used to simulate MgO in calculations utilising the CETEP code are the ones described in the last chapter. The Kerker (1980) pseudopotential is used for the magnesium ion and the optimised potential of Lin *et al* (1993) for the oxygen potential. These are chosen mainly so our work can complement that of other groups who are attempting similar calculations with these pseudopotentials. The magnesium potential generated from the data given by Bachelet, Hamann and Schlüter (1982) and the optimised oxygen potential generated by the method of Troullier and Martins (1991) are also used on occasion as an extra check on the results.

Magnesium Oxide at equilibrium has the rock salt structure. It is face-centred cubic with a basis consisting of a magnesium ion and an oxygen ion. This is shown in figure 4.1. The black and white circles distinguish the Mg and the O atoms from each other. The primitive cell contains just these two ions. The primitive lattice vectors **a** are given by,

$$\mathbf{a} = a_0 \begin{pmatrix} 0.5 & 0.5 & 0.0 \\ 0.5 & 0.0 & 0.5 \\ 0.0 & 0.5 & 0.5 \end{pmatrix} \begin{pmatrix} \mathbf{i} \\ \mathbf{j} \\ \mathbf{k} \end{pmatrix}, \tag{4.1}$$

where a_0 is the lattice parameter of the full (cubic) cell. This leads to a set of reciprocal lattice vectors **b** of the form,

$$\mathbf{b} = \frac{2\pi}{a_0} \begin{pmatrix} 1 & 1 & -1 \\ 1 & -1 & 1 \\ -1 & 1 & 1 \end{pmatrix} \begin{pmatrix} \mathbf{i} \\ \mathbf{j} \\ \mathbf{k} \end{pmatrix}. \tag{4.2}$$

The k-point sampling scheme used with this reciprocal space cell is that of Monkhorst and Pack (1976). After considerable testing a mesh of sixteen k-points was found to be sufficient for all calculations. This is obtained by using the 64 point Monkhorst-Pack set and applying the symmetry of the fcc crystal

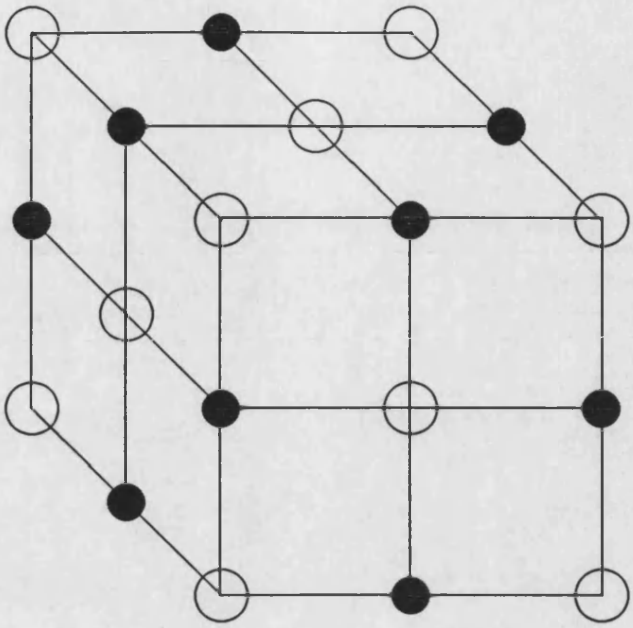

Figure 4.1: The rock salt structure of MgO at equilibrium.

to remove equivalent points. Those points remaining are located at the following positions referred to the reciprocal lattice vectors **b** in **k**-space,

$$(0.25, 0.25, 0.25), (0.50, 0.50, 0.25), (0.50, 0.25, 0.50), (0.25, 0.50, 0.50),$$

$$(0.00, 0.00, 0.25), (0.00, 0.25, 0.00), (0.25, 0.00, 0.00), (-0.25, -0.25, 0.25),$$

$$(-0.25, 0.25, -0.25), (0.25, -0.25, -0.25), (0.25, 0.50, 0.00), (0.50, 0.00, 0.25),$$

$$(0.00, 0.25, 0.50), (0.50, 0.25, 0.00), (0.25, 0.00, 0.50), (0.00, 0.50, 0.25).$$

All these points have a weighting of 1/16. As an alternative a much smaller set of only four **k**-points is used if an answer is required quickly. This, of course, runs the risk of the energy not being fully converged with respect to **k**-points. In practice it is found to cause a problem only when the cell is given a monoclinic or trigonal distortion as part of the procedure for calculating the C_{44} elastic constant. In this case the full 16 **k**-point set is used to keep the correct symmetry for the mesh. The four **k**-points used as the reduced set are,

$$(0.25, 0.25, 0.25), (-0.25, -0.25, 0.25), (-0.25, 0.25, -0.25), (0.25, -0.25, -0.25).$$

The weight for each of these points is 1/4.

With the pseudopotentials being used an energy cut-off of 1000 eV is considered sufficient for the calculations (see chapter 3 for details). The experimental value for the lattice parameter of magnesium oxide is 4.21 Å and it is expected that most of the calculations will be close to this point so reciprocal space grid of volume $(32)^3$ is chosen. This provides a grid with a side length comfortably larger than four times the radius of the sphere of energies with less than a 1000 eV cut-off energy. See chapter 2 for details of this. The calculations run from this set-up typically use $\sim$ 1500 plane wave coefficients per k-point and the CETEP code on the Edinburgh parallel computer can converge the total energy in between twelve and fifteen iterations. This takes about twenty minutes for a 4 k-point calculation or one hour and twenty minutes for a full 16 k-point calculation if sixteen nodes of the parallel surface are used.

Core corrected calculations made of the properties of MgO show small differences from the uncorrected results and are neglected in this chapter. This effect was also found to be small in MgO by De Vita *et al* (1992a and 1992b). However, they are discussed in detail in the next chapter where their effect on the properties of CaO, SrO and BaO is much larger.

4.4 Equilibrium Properties

The first calculations performed are those to establish the lattice parameter of magnesium oxide. As we have seen previously most of the theoretical calculations done before on MgO have been very successful in predicting this parameter. It is especially encouraging that the previous calculations involving pseudopotentials

(for example that of Chang and Cohen, 1984) have produced a lattice parameter within 1.0% of the experimental value.

A series of total energy calculations are made with the lattice parameter being varied over a range of values. The results of this are shown in figure 4.2. The data shown on this graph is taken from calculations using only four **k**-points. The equivalent energies for 16 **k**-point calculations are indistinguishable from the data in figure 4.2. The total energies from the 16 **k**-point calculations are ~ 3 meV more negative than those for 4 **k**-points. This is much too small to make a difference in the physical properties that are evaluated from these results. It can be seen from figure 4.2 that a very smooth curve is produced. This is a good indication that the energies are properly converged with respect to energy cut-off. Without this convergence the curve would be ragged. This problem is discussed by, for example, Gomes Dacosta *et al* (1986). By fitting a cubic polynomial to these data points a figure for the lattice parameter is obtained from the calculation. The maximum residual from this fit is very small (of order 5 meV) confirming the smoothness of the data. The energy minimum is for a lattice parameter of 4.23 Å. This is about 0.5% too big and compares well with the previous attempts at its prediction.

It is possible to derive another physical property of MgO from this data. The bulk modulus B is given by,

$$B = -V\frac{\partial P}{\partial V}, \tag{4.3}$$

where V is the volume of the unit cell and P is the pressure. However, the pressure can be obtained from the total energy U using,

$$P = -\frac{\partial U}{\partial V}. \tag{4.4}$$

This is all the information necessary to calculate B as a function of the curvature (at the minimum) of an energy against volume graph. Performing this calculation

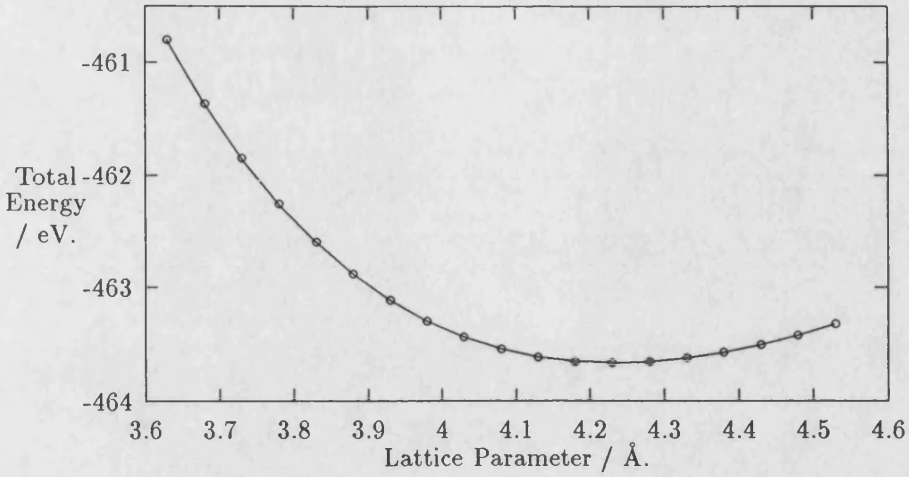

Figure 4.2: Total energy versus lattice parameter for MgO.

the bulk modulus of magnesium oxide is established to be 162.7 GPa. This is about 1.7% larger than the experimental value of 160.0 GPa (from the paper by Anderson and Andreatch, 1966). Compared with the calculated values for the bulk modulus that have been produced before this is in much greater agreement with experiment. In contrast the previous pseudopotential calculation of Chang and Cohen (1984) was almost 9% too small. The best of the other calculations (the LAPW work by Mehl, Cohen and Krakauer, 1988) is 7.5% away from the experimental value.

The next stage is to calculate the individual elastic constants. See the appendix given after this chapter for a brief summary of the equations governing elastic behaviour. From the appendix (and also Nye, 1985) the strain energy U of a distortion is given by,

$$\frac{U}{V} = \frac{1}{2} \sum_{i,j=1}^{6} C_{ij} \epsilon_i \epsilon_j, \tag{4.5}$$

where V is the cell volume, C_{ij} is the elastic constant tensor and ϵ_i is the strain applied. By applying different strains to to the unit cell energy changes from

equilibrium are obtained which can be related to the elastic constants by equation (4.5). In fact one combination of C_{11} and C_{12} has been calculated already. The calculations made to establish the lattice parameter and bulk modulus of MgO can be considered a distortion of the crystal away from equilibrium with a strain ϵ given by,

$$\epsilon = (\eta, \eta, \eta, 0, 0, 0), \tag{4.6}$$

where η is the relative change in lattice parameter from equilibrium. By substituting this into equation (4.5) it can be shown that the bulk modulus of a cubic material is given by,

$$B = \frac{1}{3}(C_{11} + 2C_{12}), \tag{4.7}$$

so $C_{11} + 2C_{12} = 488.1$ GPa. Other calculations must be performed to separate out these constants from each other. Tetragonal and orthorhombic strains are applied to the unit cell at equilibrium volume to provide different combinations of C_{11} and C_{12}. Two volume-conserving distortions are chosen for this. The strains ϵ_i for these are,

$$\epsilon_i = (\eta, \eta, -2\eta, 0, 0, 0), \tag{4.8}$$

and,

$$\epsilon_i = (\eta, -\eta, 0, 0, 0, 0). \tag{4.9}$$

Both of these, when substituted into equation (4.5), provide us with the combination $C_{11} - C_{12}$ in terms of the curvature of the energy against strain graph. If the ϵ_i given in equation (4.8) is used this leads to a strain energy given by,

$$U = 3\eta^2 V(C_{11} - C_{12}). \tag{4.10}$$

Alternatively if equation (4.9) is used then the strain energy yielded is,

$$U = \eta^2 V(C_{11} - C_{12}). \tag{4.11}$$

A non volume-conserving tetragonal distortion is used as well. In this case the strain ϵ_i is given by,

$$\epsilon_i = (\eta, \eta, 0, 0, 0, 0). \tag{4.12}$$

By substituting this into equation (4.5) once more U is obtained,

$$U = \eta^2 V(C_{11} + C_{12}). \tag{4.13}$$

As mentioned previously the data used to establish the lattice parameter is effectively another (non volume-conserving) strain so there are four ways of calculating combinations of these two parameters. The results of these calculations are shown in figure 4.3. As well as the three new sets of data points the previous $(\eta, \eta, \eta, 0, 0, 0)$ distortion data is shown against the strain parameter η. All of these calculations were made using four special **k**-points, but are again indistinguishable from 16 **k**-point calculations.

Once more smooth curves are obtained from the calculations indicating that there are no energy convergence problems. As before a cubic polynomial is fitted through the data points and the curvatures are calculated. The residuals obtained from the fitting process are of the same magnitude as those encountered before ($\sim$ 5 meV). This gives the following range of values for the elastic constants,

$$C_{11} + 2C_{12} = 488.1, \tag{4.14}$$

$$C_{11} - C_{12} = 213.5, \tag{4.15}$$

$$C_{11} - C_{12} = 210.7, \tag{4.16}$$

$$C_{11} + C_{12} = 393.9. \tag{4.17}$$

All values are in GPa. These figures all show a consistency in the values of the individual elastic constants indicating that all the calculations are well converged. By evaluating the elastic constants from all possible combinations and averaging, solutions for these two elastic constants are forthcoming. In this case the mean C_{11} is found to be 302.8 GPa and the mean C_{12} is 92.0 GPa. The individual values range between 299.7 GPa and 305.0 GPa for C_{11} and between 90.2 GPa and 94.2 GPa for C_{12}. If these are compared with the experimental values in

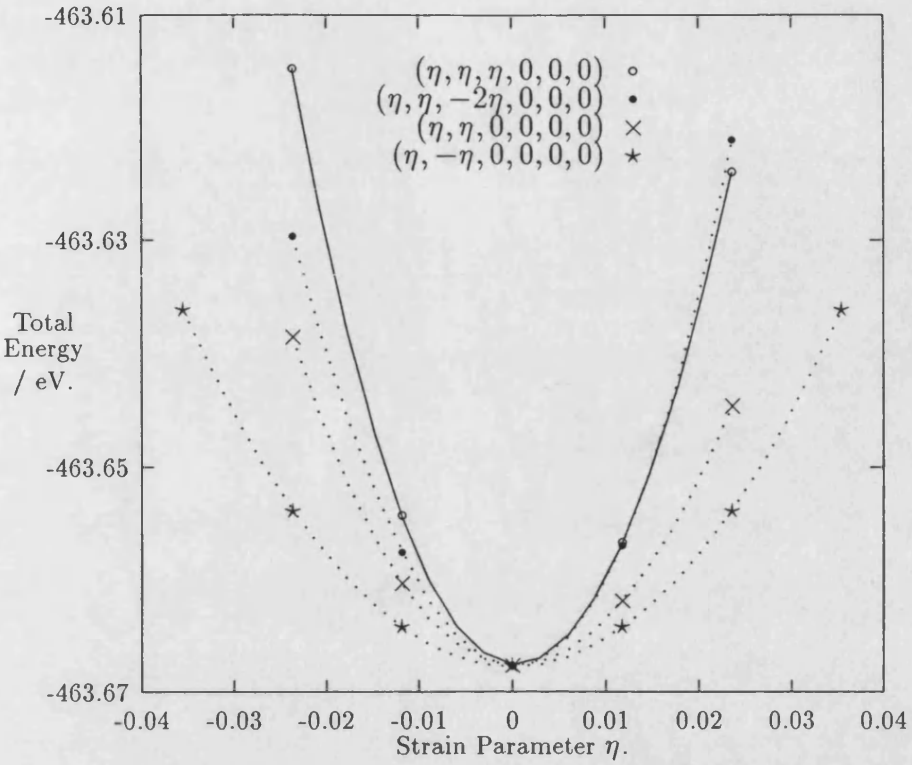

Figure 4.3: Total energy for tetragonal strains on MgO.

table 4.1 they are seen to be very close. The value for C_{11} is 3% too large and the value for C_{12} is 1% too small.

The final independent elastic constant C_{44} is evaluated in a similar manner to the procedure above. This can be obtained from the curvature of two further sets of calculations. However, now monoclinic and trigonal distortions are applied to the unit cell, rather than the tetragonal and orthorhombic ones used before. There is no problem this time with producing combinations of elastic constants as C_{44} can be calculated directly. Two distortions are made to ensure consistency. These are,

$$\epsilon_i = (0,0,0,\eta,\eta,\eta), \tag{4.18}$$

the trigonal distortion and,

$$\epsilon_i = (0, 0, 0, \eta, 0, 0), \tag{4.19}$$

which is monoclinic. Substituting these into equation (4.5) gives strain energies of,

$$U = \frac{3}{2} V \eta^2 C_{44}, \tag{4.20}$$

and,

$$U = \frac{1}{2} V \eta^2 C_{44}. \tag{4.21}$$

On this occasion the sixteen **k**-point set is used and the resulting curves are shown in figure 4.4. As before, they are very smooth. The curvatures are calculated in a similar manner to above to obtain values for C_{44} of 138.8 GPa and 140.0 GPa respectively. Taking an average of these yields a final value of 139.4 GPa for C_{44}. Compared with the experimental result of 155 GPa this is about 10% too small. Although this is not as accurate as our previous calculations it is still sufficiently close to experiment to believe that we are correctly describing the essential physics and chemistry of MgO.

As a final check on the validity of the results a quick series of calculations are made with a Troullier (1991) oxygen pseudopotential and a Hamann, Schlüter and Chiang (1979) magnesium pseudopotential. This latter potential is generated from the data provided in the paper by Bachelet, Hamann and Schlüter (1982). A 1000 eV energy cut-off is used with the reduced four **k**-point set. The results for total energy against lattice parameter are shown in figure 4.5.

As can be seen from figure 4.5 the energy minimum is, once again, very close to the experimental value for the lattice parameter. Fitting a third order polynomial to this data the lattice parameter is found to be 4.15 Å and the bulk modulus to be 175 GPa. These values demonstrate that the potentials that have been used

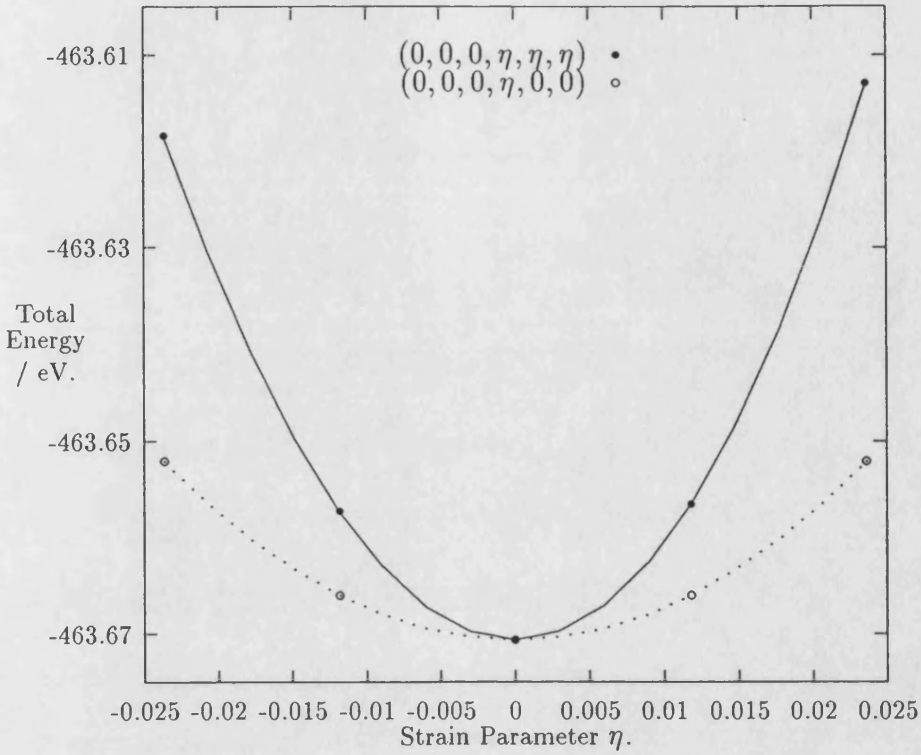

Figure 4.4: Total energy for monoclinic strains on MgO.

can provide consistent results for the parameters of interest. However, errors of a few percent are to be expected in such calculations.

These results for the most basic physical parameters of magnesium oxide are very encouraging. The equilibrium values obtained for the lattice parameter, bulk modulus and elastic constants are not only close to those found experimentally, but are also much better than the results obtained by other calculations on magnesium oxide. With this degree of accuracy it is possible to move on to calculations of the properties of MgO at high pressure. Here, of course, there are few experimental results that can be used as a guide.

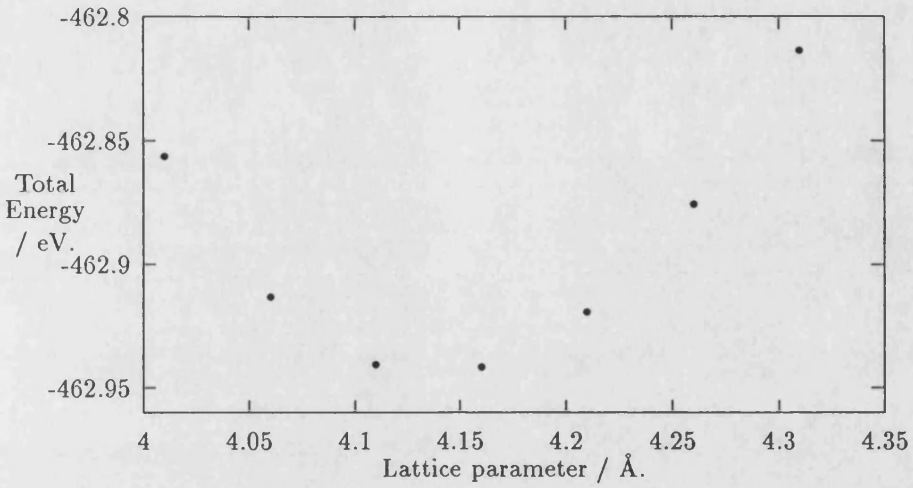

Figure 4.5: Total energy against lattice parameter for Troullier O potential.

4.5 Properties at High Pressure

We are now in a position to make calculations of the properties of magnesium oxide at high pressures. As MgO is a major constituent of the Earth's lower mantle its physical parameters within this region are of particular interest. The lower mantle exists between approximately 600 and 2800 km below the surface of the Earth. It is a crystalline aggregate with perovskite magnesium silicon oxide (olivine) and MgO as its major constituents. Pressures of up to about 1.4 Mbar ($\sim$ 140 GPa) are found within it. The high pressure calculations will be to measure the properties of MgO up to this limit in order to be of relevance to geologists and geophysicists. The first task is to establish whether or not there is a phase change in MgO due to this pressure increase. Other oxides have been shown to change phase from the B1 (NaCl type) structure to the B2 (CsCl type) structure if pressure is applied. This is due to increased packing efficiency of the B2 structure with differently sized atoms. Jeanloz and Ahrens (1980) showed

with shock-wave and diamond-cell experiments that CaO and FeO possess this B1-B2 transformation at pressures of around 700 kbar (70 GPa). Liu and Bassett (1972) discovered that BaO would change to a distorted B2 structure at pressures as low as 140 kbar (14 GPa). It is especially significant that CaO and BaO exhibit this behaviour as, like MgO, they are earth-metal oxides. By analogy it would be expected that if enough pressure is applied to MgO it would undergo the same phase change.

Experimentalists have already attempted to discover the pressure required to provoke this phase change in MgO. Carter *et al* (1971) have showed that there is no evidence for this transition up to 1.2 Mbar using shock-wave data. Similarly, Mao and Bell (1979) have found no phase change below 0.95 Mbar in diamond-cell experiments. There have also been several theoretical calculations of this transition pressure. Cohen and Gordon (1976) found the B1-B2 change at 3.7 Mbar using their modified electron-gas technique. This is greater than the maximum pressure within the lower mantle ($\sim$ 1.4 Mbar) and beyond the bounds of this work. However, an empirical calculation by Singh and Sanyal (1982) predicted that the transition pressure would be 1.17 Mbar. As well as being very much lower than the prediction of Cohen and Gordon (above) it is also within the range of pressures found in the lower mantle. Chang and Cohen (1984) used a pseudopotential technique to determine this parameter. They found that the pressure required to cause the phase change was around 10 Mbar. While this is reassuringly high it also demonstrates just how little consistency there has been in these theoretical predictions. Other calculations have placed the B1-B2 transformation at 5.15 Mbar (Mehl, Cohen and Krakauer, 1988) and 2.05 Mbar (Bukowinski, 1985). As it is not clear whether or not a B1-B2 phase change is likely at lower mantle pressures, calculations are performed to search for evidence of such a transformation within this region.

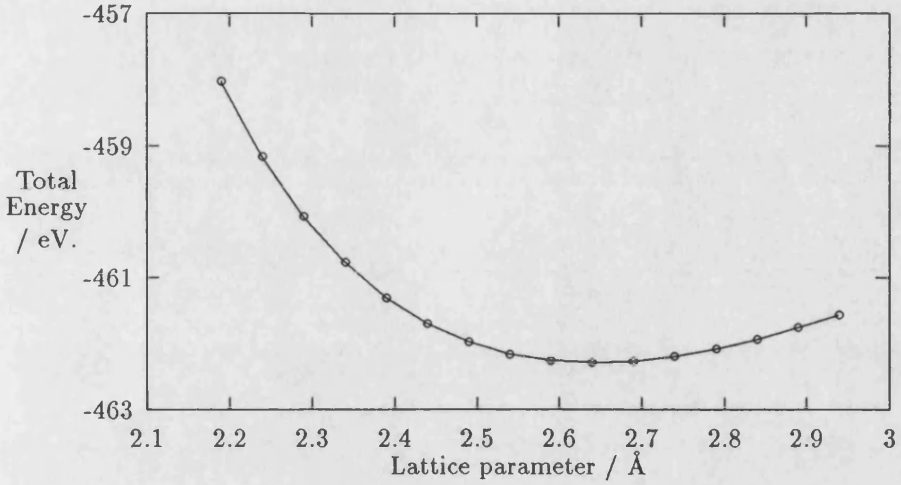

Figure 4.6: Energy versus lattice parameter for MgO in B2 phase.

The first step is to find the equilibrium lattice parameter for magnesium oxide in the B2 (CsCl) structure. This calculation is carried out using the same Kerker (1980) magnesium potential and Lin *et al* (1993) oxygen potential used before. The primitive cell is set up with the magnesium ion at the (0,0,0) point and the oxygen ion at the (0.5,0.5,0.5) point. Due to the change in symmetry (body-centred cubic rather than face-centred cubic) a set of 32 special k-points is used. The results of this are shown in figure 4.6.

By fitting a (cubic) polynomial to this the lattice parameter is calculated to be 2.63 Å for MgO in this phase. There are no experimental results with which this can be matched, but several theoretical calculations have been made with which the answer can be compared. The pseudopotential method of Chang and Cohen (1984) found the equilibrium point to be 2.63 Å also. Cohen and Gordon (1976) calculated two different lattice parameters depending upon which wave functions their modified electron-gas technique used. The equilibrium point was at 2.59 Å if they used the O^{2-} wave functions of Yamashita and Asano (1970) and it was

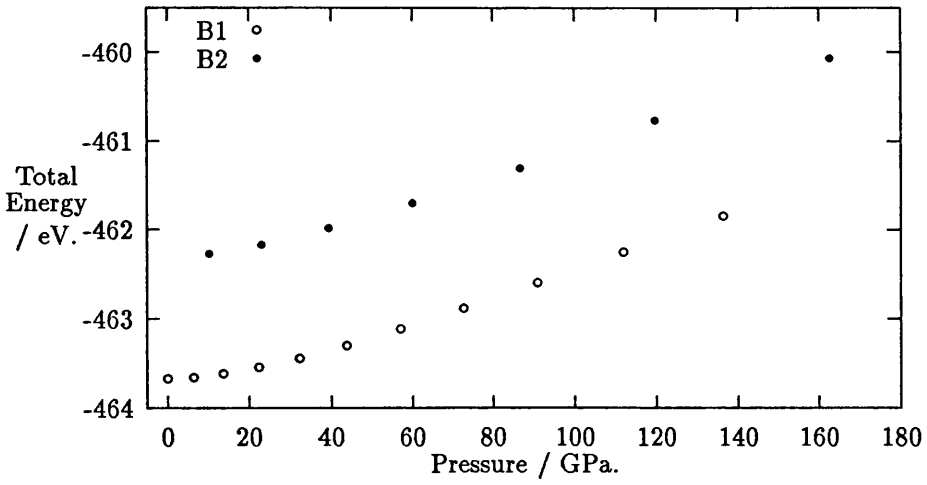

Figure 4.7: Energy of MgO in B1 and B2 phases against pressure.

found to be at 2.81 Å if the wave functions of Watson (1958) were used instead. Singh and Sanyal (1982) predicted that the lattice parameter would be 2.83 Å from their empirical calculations. Finally Yamashita and Asano (1983) obtained a value of 2.59 Å from their Korringa, Kohn, Rostoker (KKR) method. As can be seen from these predictions the value for the lattice parameter is certainly consistent with those calculations that have been made before.

The pressure that a unit cell is under can be obtained from equation (4.4) as before,

$$P = -\frac{\partial U}{\partial V},$$

where P is the pressure, U is the energy and V is the volume of the unit cell. All the data necessary to construct energy against volume graphs for MgO in both the B1 and B2 phases have been calculated already. From the gradient of these curves at a particular volume it is easy to obtain the associated pressure. The total energy of MgO in the two phases can then be plotted against pressure and the curves compared. This is shown in figure 4.7.

As can be seen from figure 4.7 there is no phase transformation within the bounds of this calculation. As the pressures up to $\sim$ 1.4 Mbar (140 GPa) have been covered we can now be confident that there will be no B1-B2 transformation of MgO within the Earth's lower mantle. There is some evidence from figure 4.7 of the difference between the two curves narrowing. If the same trend continues it is possible that a phase change would result. This could conceivably happen around the 10 Mbar (1000 GPa) predicted by Chang and Cohen (1984). This is well outside the range of pressures found with the Earth's lower mantle and beyond the scope of these calculations.

Having established that there is no B1-B2 phase change in MgO subjected to pressures occurring within the Earth's lower mantle the pressure dependence of the elastic constants are now calculated. As before a number of attempts have been made to tackle this problem already. Cohen and Gordon (1976) evaluated the variation of all three elastic constants up to pressures of 10 Mbar (1000 GPa). They found both C_{11} and C_{12} to increase roughly linearly with pressure. In contrast C_{44} was found to rise to a peak with respect to pressure at around 1 Mbar before decreasing to zero. These results are somewhat suspect because, as previously noted, there is no Cauchy violation observed at equilibrium. Isaak, Cohen and Mehl (1990) also calculated the pressure dependence of the elastic constants (up to 1.5 Mbar) using the PIB method. This method had been considerably more successful than the MEG technique (above) at predicting the equilibrium properties of MgO. Once more C_{11} and C_{12} increased with pressure. This time, however, C_{44} also rose with increasing pressure, with the curve flattening out when the pressure reached 1 Mbar. The result of this was that C_{12} had become larger than C_{44} by the time 1.4 Mbar was reached reversing the sign of the Cauchy violation. The last set of theoretical predictions were made by McCammon, Brown and Meagher (1991) with their molecular orbital calculations.

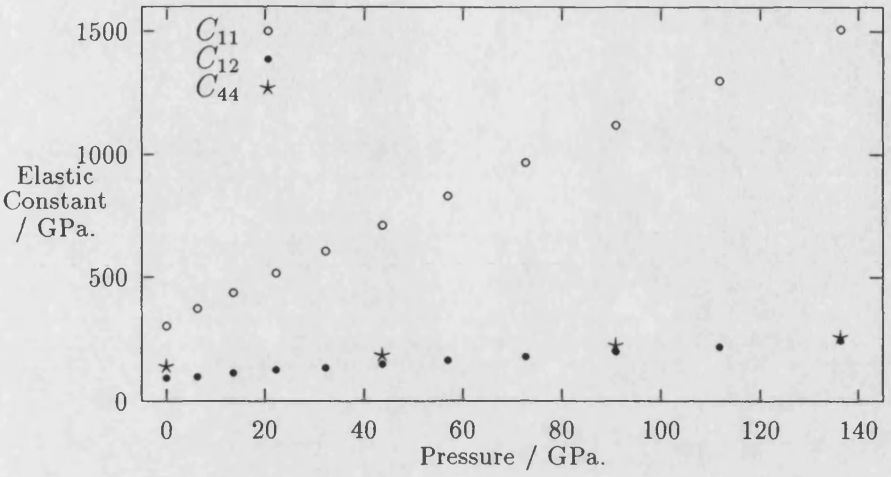

Figure 4.8: Variation of elastic constants with pressure.

The results from this were broadly similar to those of the PIB model with one important exception. On this occasion it was C_{12} whose curve slowly flattened with pressure rather than C_{44}. This ensured that there was no change to the sign of the Cauchy violation in their data. Once more it should be noted that the MO technique failed to provide good predictions of the properties of MgO at equilibrium and so cannot be expected to produce better results at high pressure.

To evaluate the variation of the elastic constants with pressure a series of calculations are made centred around increasingly small lattice parameters. The gradient of the graph of total energy against volume is used to evaluate the pressures as before. Tetragonal (for C_{11} and C_{12}) and monoclinic (for C_{44}) distortions are then placed on the cell around these volumes at which the pressure is known. The four special k-points set is used for calculations tetragonal strains while the sixteen k-points set is used, once more, for the monoclinic calculations. Evaluating the individual constants as before their values up to 1.4 Mbar (140 GPa) are obtained. These are shown in figure 4.8.

It can be easily seen from figure 4.8 that all the constants increase with pressure. The rate of increase of C_{44} is the slowest and it has almost been overhauled by C_{12} by the time 1.4 Mbar is reached. This is very reminiscent of the results of Isaak, Cohen and Mehl (1990) for their PIB model of MgO. The only major discrepancy between the two calculations being the point at which the Cauchy violation is reversed. Our results indicate that this point should be reached for pressures a little greater than 1.4 Mbar. The PIB calculations, however, show this to have happened at around 0.8 Mbar.

It is possible to derive other physical properties of MgO from the results evaluated so far. As curves of elastic constants against pressure have been calculated the pressure constants Pc_{ij} can be obtained from the gradient of the curve at zero pressure. These are defined as,

$$Pc_{ij} = \frac{\partial}{\partial P} \ln C_{ij}, \tag{4.22}$$

where P is the pressure, or,

$$Pc_{ij} = \frac{1}{C_{ij}} \frac{\partial C_{ij}}{\partial P}. \tag{4.23}$$

These are evaluated at $P = 0$. Table 4.2 summarises these along with all the earlier results in one table. The experimental results are those quoted by Hearmon (1979). The pressure derivatives (at $P = 0$) of the bulk modulus B and C' are also given alongside their experimental counterparts. As before these are averaged data from the sources quoted above. The exceptions to this are the combinations of third order elastic constants C_I, C_{II} and C_{III} which are taken from the paper by Bogardus (1965) only.

It is possible to use the data acquired to obtain three combinations of the third order elastic constants, although it is impossible to evaluate any single third order constant independently. These are obviously closely related to the pressure

Parameter	Calculated	Experimental
a_0	4.232 Å	4.213 Å
B	162.7 GPa	160.0 GPa
C_{11}	302.8 GPa	294.0 GPa
C_{12}	92.0 GPa	93.0 GPa
C_{44}	139.4 GPa	155.0 GPa
$\frac{\partial B}{\partial P}$	4.2117	3.894
$\frac{\partial C'}{\partial P}$	4.0252	3.823
Pc_{11}	33.525 $(TPa)^{-1}$	31.0 $(TPa)^{-1}$
Pc_{12}	16.466 $(TPa)^{-1}$	17.7 $(TPa)^{-1}$
Pc_{44}	8.291 $(TPa)^{-1}$	7.5 $(TPa)^{-1}$
C_I	-5463.1 GPa	-5090.0 GPa
C_{II}	-66.0 GPa	-1205.0 GPa
C_{III}	-350.2 GPa	-259.0 GPa

$B = \frac{1}{3}(C_{11} + 2C_{12})$, $C' = \frac{1}{2}(C_{11} - C_{12})$,
$Pc_{ij} = \frac{\partial}{\partial P} \ln C_{ij}$,
$C_I = C_{111} + 2C_{112}$, $C_{II} = C_{144} + 2C_{166}$,
$C_{III} = C_{123} + 2C_{112}$.

Table 4.2: Summary of MgO physical parameters calculated.

constants already calculated. For a cubic material there are six independent third order elastic constants. They are C_{111}, C_{112}, C_{123}, C_{144}, C_{155} and C_{456}. We can relate these to the parameters that have already been calculated by using the expressions developed by Birch (1947),

$$\frac{\partial C_{44}}{\partial P} = -\frac{(C_{11} + 2C_{12} + C_{44} + C_{144} + 2C_{166})}{(C_{11} + 2C_{12})}, \tag{4.24}$$

$$\frac{\partial C'}{\partial P} = -\frac{(3C_{11} + 3C_{12} + C_{111} - C_{123})}{2(C_{11} + 2C_{12})}, \tag{4.25}$$

and,

$$\frac{\partial B}{\partial P} = -\frac{(C_{111} + 6C_{112} + 2C_{123})}{3(C_{11} + 2C_{12})}. \tag{4.26}$$

The three combinations can then be calculated directly as equation (4.24) is written in terms of $C_{144} + 2C_{166}$ which is termed C_{II}. Equations (4.25) and (4.26) are expressed in terms of $C_I - C_{III}$ and $C_I + 2C_{III}$ respectively, where $C_I = C_{111} + 2C_{112}$ and $C_{III} = C_{123} + 2C_{112}$. Three combinations of third order elastic constants have been evaluated which include five of the individual constants between them.

From the calculations performed there is no way to establish the sixth third order constant C_{456}. For more information on the derivation of these equations see the papers by Thakur (1980) or Walker, Saunders and Schäl (1987). As can be seen from table 4.2 good predictions have been made for both C_I and C_{III} and if nothing else the sign is correct for C_{II}.

As good accuracy has been achieved in the calculation of pressure constants Pc_{ij} and other high pressure properties it is possible to derive some geophysical properties of MgO within the Earth's lower mantle. Of great interest to geologists and geophysicists are the velocities of seismic waves as they travel through the mantle. These can be calculated from the data that has been acquired already. The two most important wave velocities are known as V_p and V_s. They are (respectively) the velocity of a compressional wave and a shear wave travelling through the mantle due to seismic activity. These are given by,

$$V_p = \sqrt{\frac{B + \frac{4}{3}G}{\rho}}, \tag{4.27}$$

$$V_s = \sqrt{\frac{G}{\rho}}. \tag{4.28}$$

Here B is the bulk modulus of the aggregate, G is the Hill average (see Hill, 1952) of the rigidity modulus and ρ is the density of the polycrystalline solid. All of these are evaluated at a constant pressure. There is one final velocity that can be calculated from the results so far,

$$V_\phi = \sqrt{\frac{B}{\rho}}. \tag{4.29}$$

This velocity is of less interest to geophysicists. The Hill average rigidity modulus is the average of the rigidity moduli derived by Voigt (1928) G_v and that of Reuss (1929) G_r. These are given by,

$$5G_v = (C_{11} - C_{12}) + 3C_{44}, \tag{4.30}$$

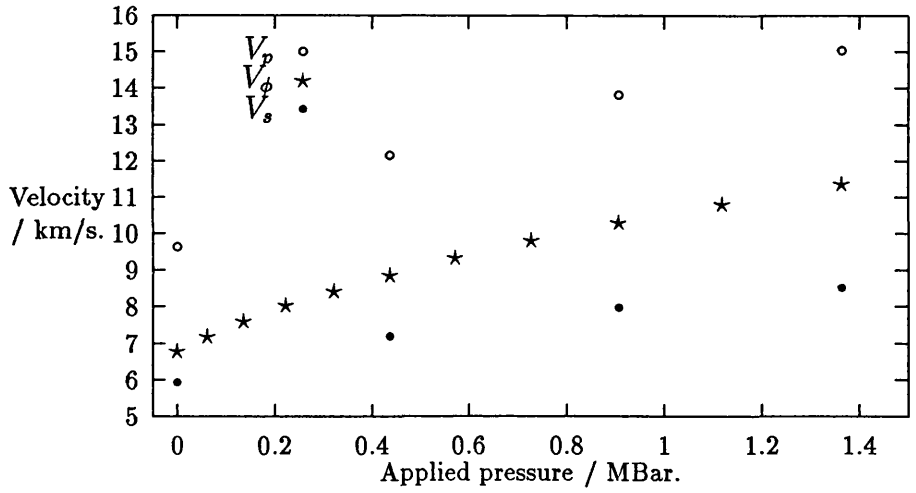

Figure 4.9: Variation of velocities V_p, V_ϕ and V_s with pressure in MgO.

$$\frac{5}{G_r} = 4(S_{11} - S_{12}) + 3S_{44}. \tag{4.31}$$

The C_{ij} are the elastic constants as before, the S_{ij} are the complimentary elastic moduli. Hill (1952) showed that the actual rigidity modulus of a polycrystalline material G lay between these two values and suggested taking a simple average of the two. Figure 4.9 shows the results obtained for the three wave velocities as the pressure increases to 1.4 Mbar (140 GPa).

Although no experimental work exists for the wave velocities of MgO at high pressure the curves obtained do bear a striking resemblance in form and magnitude to those obtained for crystalline aggregates (including MgO) within the lower mantle. Duffy and Anderson (1989) show curves for both compressional and shear wave velocities against depth below the Earth's crust (effectively pressure) for magnesium rich aggregates. These are reproduced in figures 4.10 and 4.11.

Both of these figures show seismic wave velocities for depths up to 1000 km below

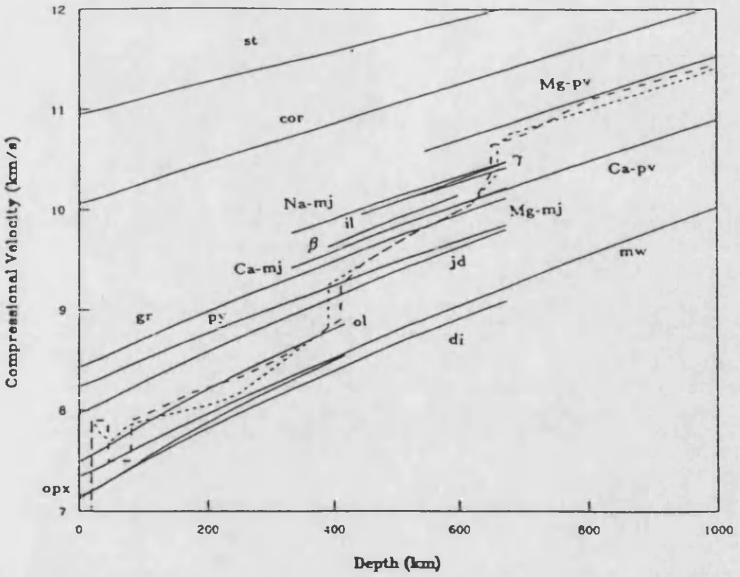

Figure 4.10: Compressional wave velocity versus depth from Duffy and Anderson (1989).

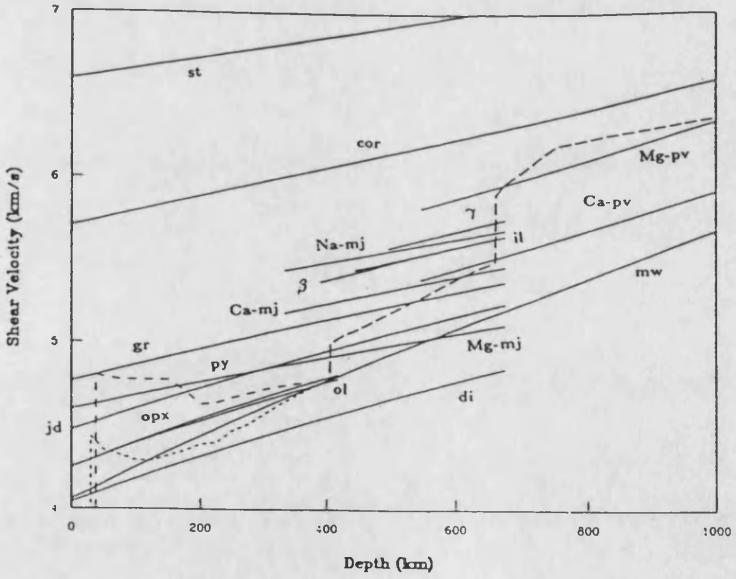

Figure 4.11: Shear wave velocity versus depth from Duffy and Anderson (1989).

the surface of the Earth. This is the equivalent to a pressure of 0.5 Mbar. Of particular interest in figures 4.10 and 4.11 are the curves labelled *mw*. These are the wave velocities in *magnesiowürstite* which is a polycrystalline aggregate made from MgO and FeO. In figure 4.10 the compressional wave velocity is shown to be $\sim$ 7.5 km/s at the surface, and rises to $\sim$ 10 km/s at a depth of 1000 km (0.5 Mbar). These are slightly smaller than the corresponding values calculated for MgO in figure 4.9. Similarly figure 4.11 shows the shear wave velocity rising from $\sim$ 4 km/s at the surface to $\sim$ 5.5 km/s at a depth of 1000 km below the crust. Once again these are slightly smaller than the calculated values in figure 4.9.

Seismic tomography is used to provide data for modelling the density changes that occur as part of the Earth's structure (see, for example, Richards and Hager, 1984 or Hong and Yuen, 1990). Small frequency changes in the measured seismic waves are a functional of the density ρ, the compressional wave velocity V_p and the shear wave velocity V_s. In order to produce results that are meaningful in relation to known mantle properties the perturbations in density and wave velocity must be correctly scaled to each other (Masters *et al*, 1984). These seismic velocity perturbations against density perturbations within the lower mantle, R, are given by,

$$R = \frac{\partial \ln V}{\partial \ln \rho}, \tag{4.32}$$

where V is a seismic velocity and ρ is the density. There are three sets of data from this corresponding to the three velocities V_p, V_s and V_ϕ. Many workers (such as Masters *et al*, 1982; Ricard *et al*, 1984 and Richards and Hager, 1984) have taken these R to be constant. More recently Ricard *et al* (1989) allowed R to vary with pressure in their calculations. By using the values of seismic velocities calculated earlier along with their respective densities in equation (4.32) it is possible to produce three curves for R_p, R_s and R_ϕ. Figure 4.12 shows all of these curves together.

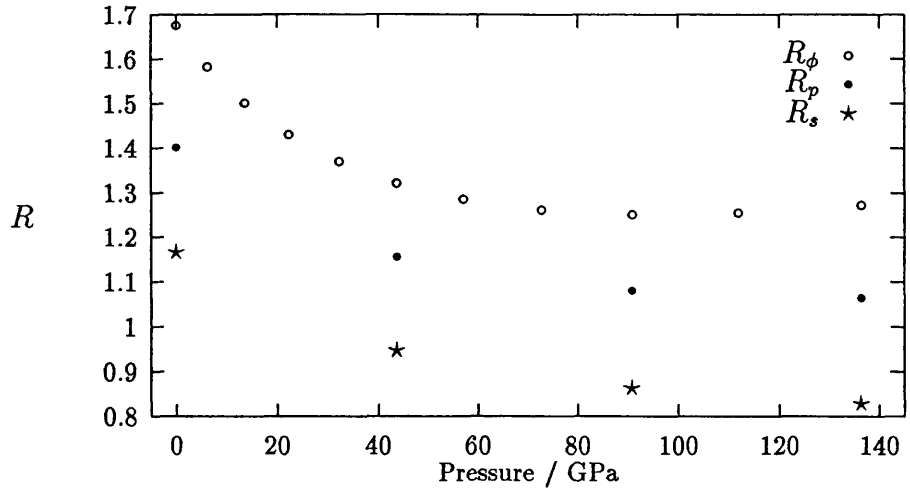

Figure 4.12: Variation of seismic velocity perturbation with pressure in MgO.

All three data sets shown on figure 4.12 are in broad agreement with work that has been done before by Parker and Wall (1991) and Isaak, Cohen and Mehl (1990). According to the values calculated here the ratio of R_s to R_p remains fairly constant at around 0.80. It is interesting to compare this with the prediction of Agnon and Bukowinski (1990) that this ratio should be ≥ 2.0. It is possible that this discrepancy is caused by localised temperature differences within the lower mantle postulated by Dziewonski and Woodhouse (1987). This is beyond the scope of the CETEP codes to simulate.

4.6 Charge Distribution and Bonding

When the CETEP code has fully converged the total energy the charge density can then be examined. The full sixteen k-point set must be used to ensure the full convergence of the results in this respect. For example figure 4.13 shows the pseudo-charge density in the [100] plane of MgO at its calculated equilibrium

lattice constant of 4.23 Å. There are oxygen ions at each corner of the cell, and in the centre. Magnesium ions are to be found half way along each edge. As the original calculation is of the primitive cell with only one magnesium and one oxygen ion data must be transformed to the full fcc cell. To do this the planes which had been stored on separate nodes in the calculation are unscrambled. They are then transferred to their correct positions on a $(64)^3$ grid and the three lattice transformations are used to fill out the rest of the mesh. This completed grid can then be sliced in any way desired to be displayed like figure 4.13.

As this method is a pseudopotential one it is only the pseudo-valence charge that is seen in figure 4.13. Only valence electrons are present in the calculation as core electrons are considered frozen on to the ion cores. The valence charge density is also not properly modelled within the core radius r_c of the pseudopotential, because the pseudo-wave functions are not constrained to mimic the true wave functions within this region. The scale used is electrons (times $(32)^3$, the size of the mesh used in the calculation) per Angstrom^3. The contours displayed are only those which enclose the magnesium ion sites and the first three that enclose the oxygen ion sites. The charge on the oxygen sites rises very quickly and the vast majority of the charge is (as might be expected) enclosed within the contours numbered 6. As this is a pseudo-valence charge there is a charge density minimum on each magnesium ion site. The valence electrons have been drawn away from the magnesium ions and towards the oxygen ions as would be expected in any ionic crystal. It should be noted that the number six contour is almost perfectly circular. The charge cloud around the oxygen ion sites is spherical from this point onwards. Comparison shows these charge densities to be in all respects similar to those generated by other theoretical techniques. Xu and Ching (1990) have produced charge density plots showing all electrons (including the core) in MgO rather than just the valence bands. This leads to charge density being present

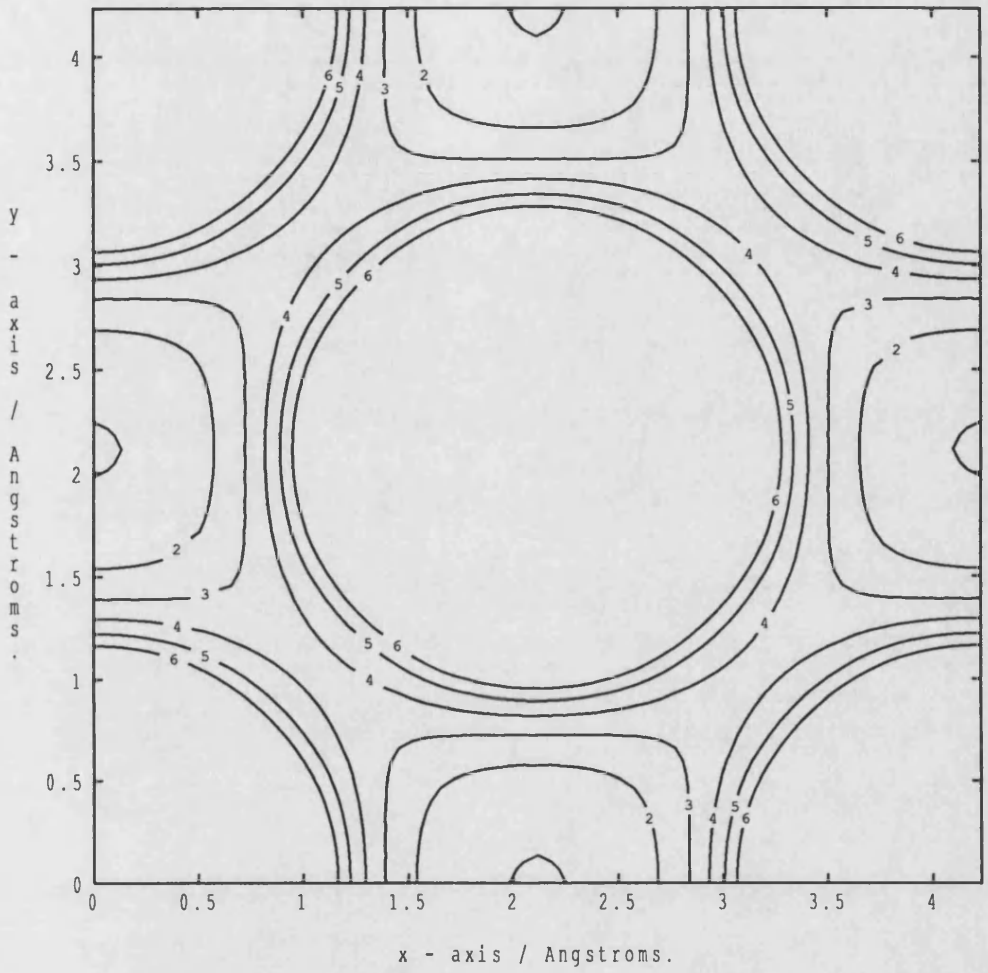

CONTOUR KEY	
1	0.1000E+00
2	0.8800E+00
3	0.1660E+01
4	0.2440E+01
5	0.3220E+01
6	0.4000E+01

Figure 4.13: Charge Density of MgO at equilibrium.

on the Magnesium ion sites. The shape of the contours in the interstitial region is very similar to those of figure 4.13, though. Mehl, Cohen and Krakauer (1988) produced valence charge densities for MgO from their LAPW calculations. Once more the contours are very similar to those calculated here.

In order to ascertain the mechanism for the violation of the Cauchy condition it is instructive to look at charge density patterns from cells that have been given a volume-conserving tetragonal distortion away from equilibrium. This should establish whether the oxygen charge cloud remains spherical, or distorts with the unit cell. Figure 4.14 shows the charge density pattern for the [001] plane for MgO with a tetragonal strain applied.

The scale for figure 4.14 is the same as that for 4.13 so the two patterns can be compared directly. Once again the number six contour is found to be almost perfectly circular and its radius is exactly the same of its counterpart in figure 4.13. This is qualitative evidence that the oxygen charge clouds remain spherical when volume-conserving distortions are applied to the unit cell. There is, however, a marked change in the shape of the charge around the Mg atom sites.

By counting up all the charge within the contours enclosing the oxygen and the magnesium ion sites a measure of the ionicity of the compound is obtained. In this case it is found that the crystal is composed of $Mg^{1.3+}$ and $O^{1.3-}$ ions. However it would be equally valid interpretation to say that all the charge is contained within $O^{2.0-}$ spheres which overlap slightly. To investigate this and the shape of the oxygen charge cloud more rigorously the charge distribution in reciprocal space must be analysed.

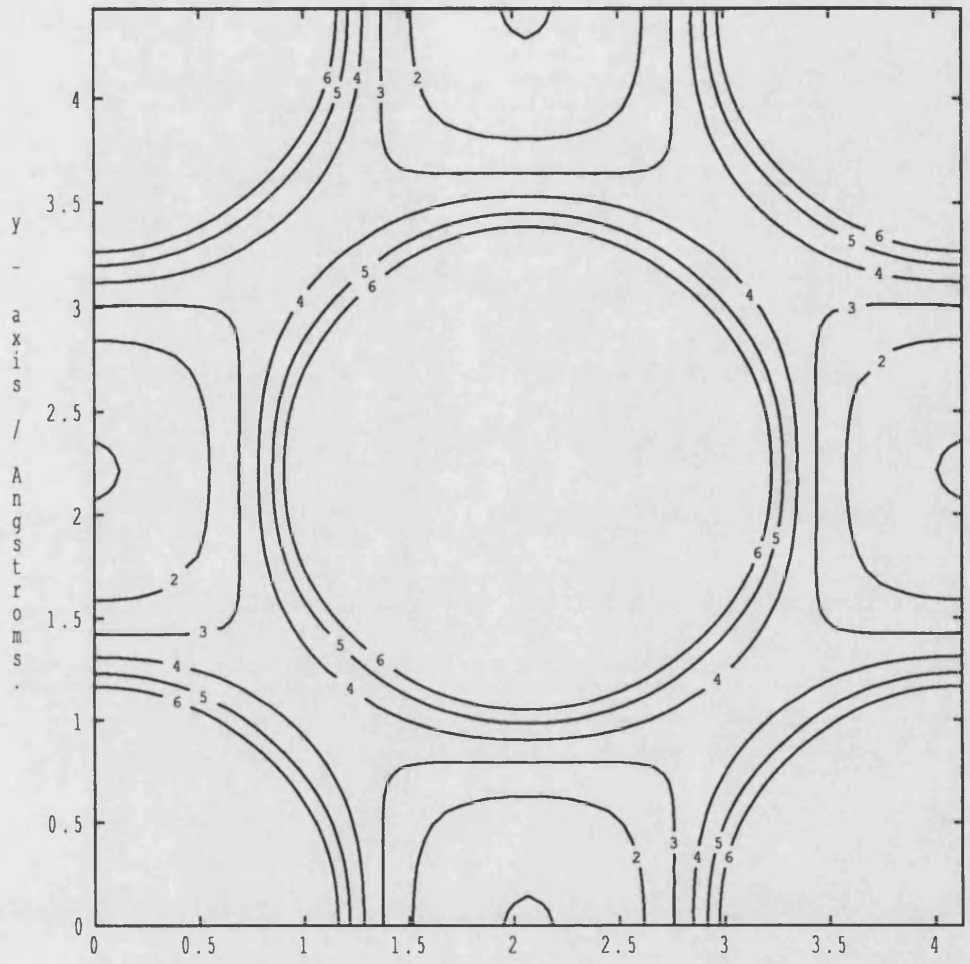

CONTOUR KEY	
1	0.1000E+00
2	0.8800E+00
3	0.1660E+01
4	0.2440E+01
5	0.3220E+01
6	0.4000E+01

Figure 4.14: Charge density of MgO with tetragonal strain applied.

In real space the charge density can be expressed as the following equation,

$$\rho(\mathbf{r}) = \sum_{\mathbf{l}} [\rho_O(\mathbf{r} - \mathbf{l} - \mathbf{r}_O) + \rho_{Mg}(\mathbf{r} - \mathbf{l} - \mathbf{r}_{Mg})], \tag{4.33}$$

where l is a lattice vector, ρ_O is a charge density object centred on the oxygen ion site and ρ_{Mg} is a similar charge density object centred on the magnesium ion site. In MgO $\mathbf{r}_O = (0,0,0)$ and $\mathbf{r}_{Mg} = (0.5,0.5,0.5)$. In terms of the reciprocal space charge density $\rho_\mathbf{g}$,

$$\rho(\mathbf{r}) = \sum_{\mathbf{g}} \rho_\mathbf{g} \exp(i\mathbf{g} \cdot \mathbf{r}), \tag{4.34}$$

where,

$$\rho_\mathbf{g} = \sum_i \rho_i(\mathbf{g}) \exp(-i\mathbf{g} \cdot \mathbf{r}_i), \tag{4.35}$$

i denotes each atom in the unit cell and,

$$\rho_i(\mathbf{g}) = \int dr \rho_i(\mathbf{r}) \exp(-i\mathbf{g} \cdot \mathbf{r}). \tag{4.36}$$

Therefore, in the case of MgO,

$$\rho_\mathbf{g} = [\rho_O(\mathbf{g}) + \rho_{Mg}(\mathbf{g}) \exp\{i2\pi(h/2 + k/2 + l/2)\}], \tag{4.37}$$

or,

$$\rho(\mathbf{g}) = \rho_O(\mathbf{g}) \pm \rho_{Mg}(\mathbf{g}), \tag{4.38}$$

where $\rho_O(\mathbf{g})$ and $\rho_{Mg}(\mathbf{g})$ describe the full (reciprocal space) charge density in terms of objects centred on the oxygen and magnesium sites. The $\pm$ arises from the allowed reflections in a fcc crystal. Those reflections with h,k,l even lead to charge density of the form $\rho_O + \rho_{Mg}$ while those with h,k,l odd yields the solution in the form $\rho_O - \rho_{Mg}$. If $\rho_O(\mathbf{r})$ and $\rho_{Mg}(\mathbf{r})$ are spherical and smooth, then $\rho_O(\mathbf{g})$ and $\rho_{Mg}(\mathbf{g})$ will also be spherical and smooth in reciprocal space. The breakup of density into ρ_O and ρ_{Mg} is not unique. Their reciprocal space forms will reveal which divisions are reasonable, and whether the description in terms of overlapping spheres is a good one.

The overall charge density $\rho(\mathbf{g})$ is then examined to see how it is made up of the contributions from ρ_O and ρ_{Mg}. Figure 4.15 shows how ρ varies against g-vector for MgO at equilibrium and tetragonally strained (a volume-conserving action) from this point. It is useful to compare these data points with the equivalents for neutral pseudo-atoms on the same atom sites. For this the charge densities of individual magnesium and oxygen atoms are calculated in very large unit cells so the atoms are effectively isolated. All other parameters in the calculation (such as cut-off energy) are given the same values as in the previous MgO calculation. The individual pseudo-atom charge densities can now be combined to give the total reciprocal space charge density for magnesium and oxygen atoms that occupy the correct lattice positions for MgO, but do not bond. All points will lie on either the + or − curve.

The neutral atom data is shown in figure 4.15 as the solid and dotted lines. The points for the equilibrium MgO calculation lie close to the neutral atom lines, the process of bonding having moved the electrons around a little as expected. All the equilibrium points seem to lie on a single smooth curve. Therefore, to first approximation a density can be constructed from overlapping atoms like those in equation (4.33). As there is no clear separation into two curves (for $\rho_O \pm \rho_{Mg}$) oxygen atoms only are needed. This description of the density is not unique, but it is as good as any other.

Figure 4.15 also shows the charge density obtained from a crystal with a volume-conserving tetragonal distortion applied. If equation (4.33) still holds, with the same distribution $\rho_O(\mathbf{r})$, then ρ_g will simply be given by $\rho_\mathrm{g} = \rho_O(\mathrm{g})$ and the data points will lie on the same curve as for the basic cubic case. If figure 4.15 is examined this is indeed what is seen. The model of overlapping spherical oxygen ions looks to be good even when a volume-conserving tetragonal strain is applied.

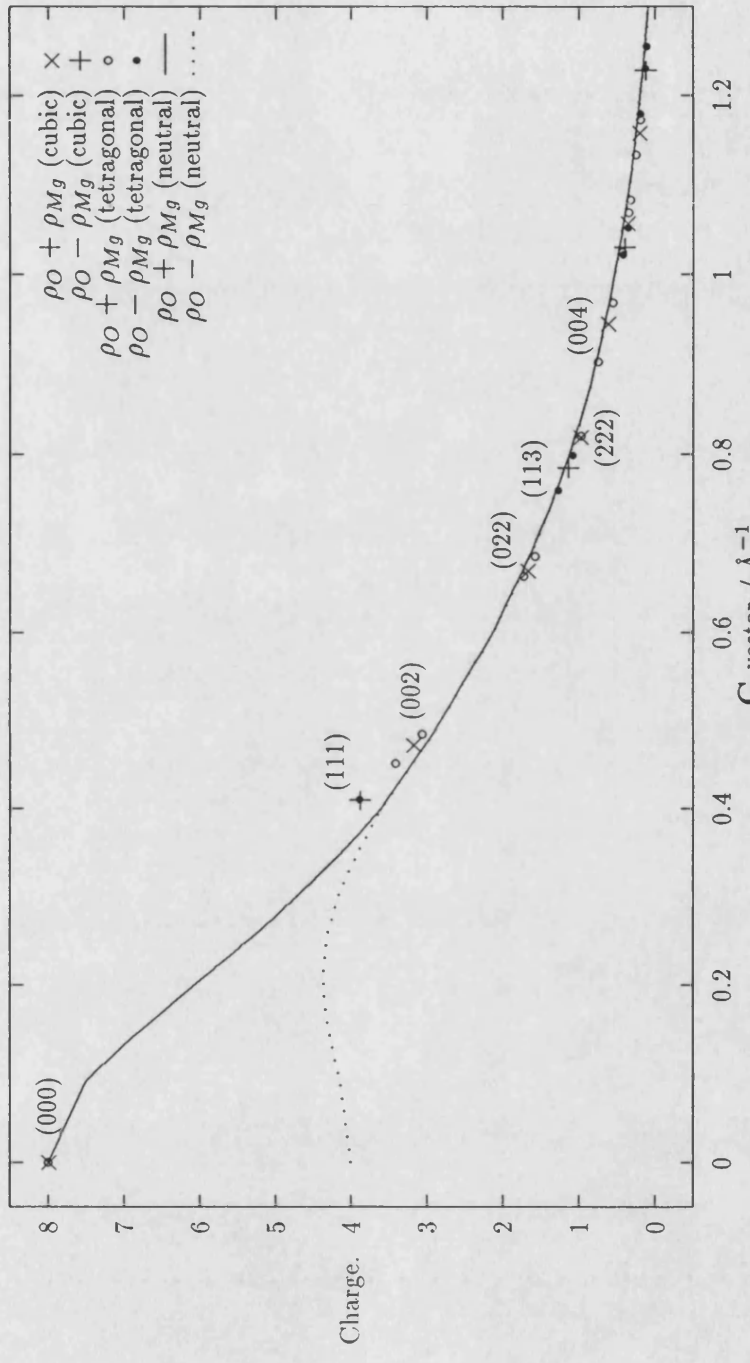

Figure 4.15: Charge density in **G**-space for MgO strained around equilibrium.

The alternate hypothesis is that the charge density distorts with the unit cell as the strain is applied. In this case a point $\mathbf{r}$ in the original cell goes to $\mathbf{r}' = (\mathbf{1}+\epsilon)\mathbf{r}$ in the distorted cell, where ϵ is the strain tensor for the volume-conserving tetragonal distortion. The charge density at $\mathbf{r}'$ is the same as it was at the equivalent point $\mathbf{r}$ in the original cell. This is $\rho([\mathbf{1}-\epsilon]\mathbf{r}')$ to first order. The reciprocal lattice vectors of the new cell $\mathbf{g}'$ are given by,

$$\mathbf{g}' = (\mathbf{1}-\epsilon)\mathbf{g}, \tag{4.39}$$

where the $\mathbf{g}$ are the original reciprocal lattice vectors. Therefore, the Fourier transform in the new cell is,

$$\rho'_O(\mathbf{g}') = \int d\mathbf{r}'\rho'_O(\mathbf{r}')\exp(-i\mathbf{g}'\cdot\mathbf{r}'), \tag{4.40}$$

so,

$$\rho'_O(\mathbf{g}') = \int d\mathbf{r}'\rho_O([\mathbf{1}-\epsilon]\mathbf{r}')\exp(-i[\mathbf{1}-\epsilon]\mathbf{g}\cdot\mathbf{r}'). \tag{4.41}$$

If the variable is now changed so that $\mathbf{r}'' = (\mathbf{1}-\epsilon)\mathbf{r}'$ then (as $d\mathbf{r}'' = d\mathbf{r}'$ to first order),

$$\rho'_O(\mathbf{g}') = \int d\mathbf{r}''\rho_O(\mathbf{r}'')\exp(-i[\mathbf{1}-\epsilon]\mathbf{g}\cdot[\mathbf{1}+\epsilon]\mathbf{r}''). \tag{4.42}$$

Therefore,

$$\rho'_O(\mathbf{g}') = \int d\mathbf{r}''\rho_O(\mathbf{r}'')\exp(-i\mathbf{g}\cdot\mathbf{r}''). \tag{4.43}$$

This is equal to $\rho_O(\mathbf{g})$ for the original g-vectors. In other words the points would split horizontally in figure 4.15 if the charge density were distorted. As this does not occur the model of spherical overlapping oxygen ions is supported for the case of the volume-conserving distortion.

Figure 4.16 shows a blow-up of a similar graph of charge density against g-vector. This time the volume of the unit cell has been changed for each calculation. At each volume points from calculations on cubic MgO have been made together with those of volume-conserving strains calculated about each volume. Once

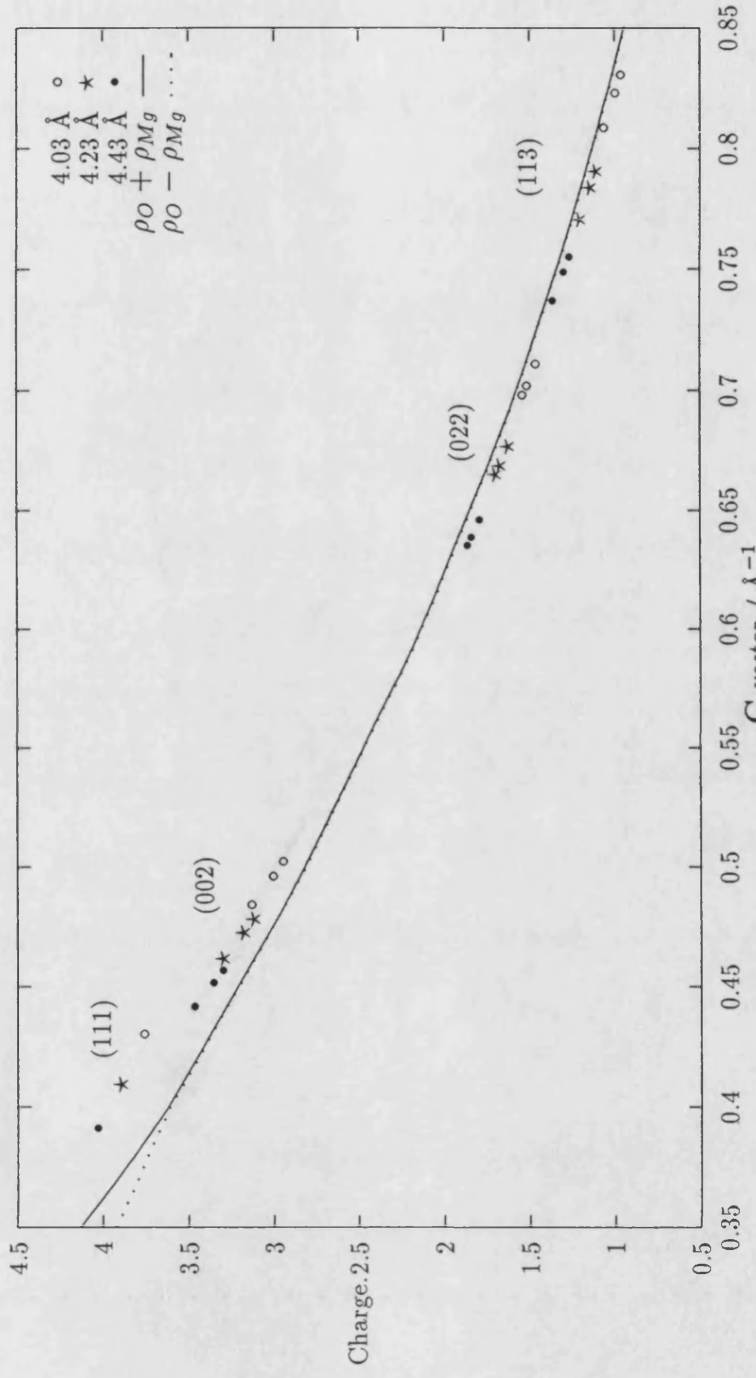

Figure 4.16: Charge density in **G**-space for MgO with changing cell volumes.

again the curves for neutral Mg and O atoms at equilibrium positions are shown for comparison. This time the data is split into three curves corresponding to the three unit cell volumes used. This indicates that the charge cloud around an oxygen ion has not remained the same size, it must be distorting in some way. If it is distorting with the change in cell volume then the above analysis is repeated to yield,

$$\rho'_O(\mathbf{g}') = \rho_O(\mathbf{g}), \tag{4.44}$$

as before. Once more this is a horizontal splitting of the data points. If figure 4.16 is examined it can be seen that this is indeed what occurs in this case. The three curves from the calculations with different unit cell volumes are of similar basic shapes but they are now shifted away from each other. The curve from the largest cell volume is moved closer to the origin in **g**-space while that of the smallest cell volume is moved away from the origin in the way predicted by equation (4.44). The change in $\rho_O(\mathbf{g})$ is not as large as equation (4.44) predicts. This is not surprising as it is unlikely that the whole ion is distorted when the unit cell volume is changed. Only the outermost electrons in the oxygen charge density are distorted in this way.

The charge cloud around an oxygen ion appears undistorted when a volume-conserving distortion is placed on the unit cell. When a volume-changing distortion is applied, however, the charge cloud distorts with the strain on the unit cell. This is support for the *breathing shell* model as the mechanism for the Cauchy violation in MgO.

Finally, by subtracting the g-space charge density from the equilibrium MgO calculation from the neutral atom data the movement of the charge density during bonding is investigated. When this is transformed back into real space the charge density contours shown in figure 4.17 are obtained.

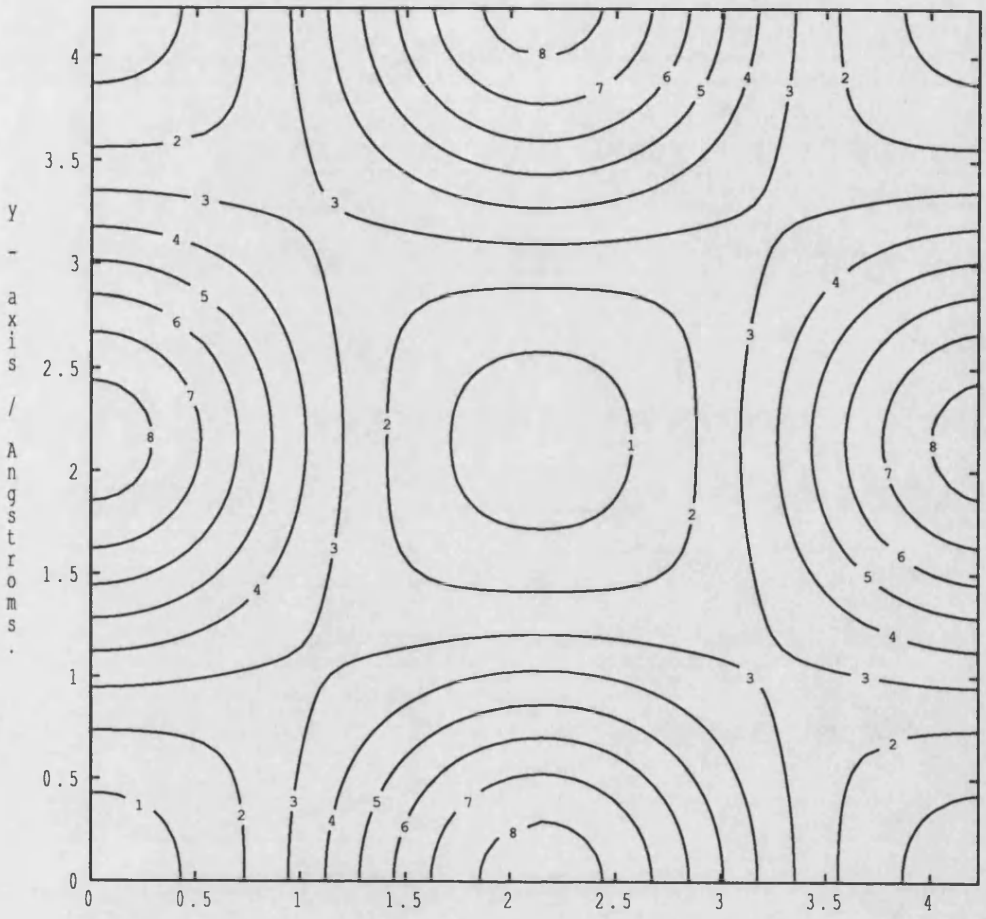

CONTOUR KEY	
1	-0.17E+01
2	-0.99E+00
3	-0.25E+00
4	0.50E+00
5	0.12E+01
6	0.20E+01
7	0.27E+01
8	0.35E+01

Figure 4.17: Changes in charge density as bonding occurs in MgO.

Figure 4.17 shows the relative change in the amount of charge density in MgO before and after bonding. Once more this is the [100] plane. This time the magnesium ion sites are at the centre and at each corner while the oxygen ion sites are half way along each edge. As would be expected figure 4.17 reveals that charge has been moved away from the magnesium sites and piled on or around the oxygen sites. The movement of charge shown in this figure is the equivalent of ~ 1.3 electrons being lost by each magnesium atom to each oxygen atom. This is the same result that was found earlier.

4.7 Summary

In summary we have successfully used the CETEP code to investigate the properties of magnesium oxide. Our predictions of the basic physical parameters of MgO at equilibrium are extremely close to those found experimentally. They are also more accurate than any other previous theoretical prediction of these parameters, in some cases significantly so. As our results at equilibrium were sufficiently good we felt confident enough in our method to attempt calculations of the properties of MgO at the high pressures to be found within the Earth's lower mantle. From these we were able to obtain curves for the elastic constants with increasing pressure. These curves are broadly similar to the best of the previous calculations. We are also able to obtain values for the pressure constants of MgO which matched experiment well, and useful values for three independent combinations of third order elastic constants.

Examination of the charge density of MgO in both real and reciprocal space allowed us to understand the mechanism for the violation of the Cauchy condition. Volume-conserving tetragonal strains around the equilibrium structure showed

that the charge cloud centred on the oxygen ion sites remained nearly spherical at all times rather than distorting with the unit cell. Volume-changing strains revealed that the spheres of charge density around each oxygen ion increased and decreased their volume as the volume of the unit cell was changed. This is support for the breathing shell model. It is important to justify this as empirical calculations (especially the potential-induced breathing shell model) have already made use of this behaviour in their work on MgO.

4.8 Appendix: Summary of the Equations of Elastic Theory

For a full account of definitions and the derivations of the equations of elastic theory see any of the text books on this subject, for example Nye (1985). Forces exerted on the surface of a volume element in a body are proportional to the area of the element and are represented by the stress tensor σ_{ij}. The force per unit area exerted on a surface perpendicular to the Ox_1-axis in the direction of the Ox_1-axis is given by σ_{11}. Similarily for the other normal components of the stress; σ_{22} and σ_{33}. The force per unit area exerted on a surface perpendicular to the Ox_1-axis in the direction of the Ox_2-axis is given by σ_{21}. Once again this is repeated for the other shear components of the stress; σ_{12}, σ_{13}, σ_{32} etc. At equilibrium (as the turning moment must be zero) $\sigma_{ij} = \sigma_{ji}$ so the stress tensor is,

$$\sigma_{ij} = \begin{bmatrix} \sigma_{11} & \sigma_{12} & \sigma_{31} \\ \sigma_{12} & \sigma_{22} & \sigma_{23} \\ \sigma_{31} & \sigma_{23} & \sigma_{33} \end{bmatrix}. \tag{4.45}$$

As there are only six independent stress components this is often written in the form of a (row or column) matrix σ_i where i now runs from one to six such that,

$$\begin{bmatrix} \sigma_{11} & \sigma_{12} & \sigma_{31} \\ \sigma_{12} & \sigma_{22} & \sigma_{23} \\ \sigma_{31} & \sigma_{23} & \sigma_{33} \end{bmatrix} \rightarrow \begin{bmatrix} \sigma_1 & \sigma_6 & \sigma_5 \\ \sigma_6 & \sigma_2 & \sigma_4 \\ \sigma_5 & \sigma_4 & \sigma_3 \end{bmatrix}. \tag{4.46}$$

When a body is acted upon by stress σ_{ij} it will be deformed. This distortion is represented by the strain tensor ϵ_{ij}. This is defined in terms of another tensor $\mathbf{e}_{ij}$ where,

$$\mathbf{e}_{ij} = \frac{\partial u_i}{\partial x_j}. \tag{4.47}$$

The u_i are the displacements of the positions x_i so that e_{11} is an extension parallel to the Ox_1-axis and e_{12} is a rotation about the Ox_3-axis of a line element parallel to the Ox_2-axis towards the Ox_1-axis. This tensor is unsymmetrical. The strain tensor ϵ_{ij} is now defined as the symmetrical part of $\mathbf{e}_{ij}$ which is $\frac{1}{2}(\mathbf{e}_{ij} + \mathbf{e}_{ji})$. In full,

$$\begin{bmatrix} \epsilon_{11} & \epsilon_{12} & \epsilon_{31} \\ \epsilon_{12} & \epsilon_{22} & \epsilon_{23} \\ \epsilon_{31} & \epsilon_{23} & \epsilon_{33} \end{bmatrix} = \begin{bmatrix} e_{11} & \frac{1}{2}(e_{12}+e_{21}) & \frac{1}{2}(e_{31}+e_{13}) \\ \frac{1}{2}(e_{12}+e_{21}) & e_{22} & \frac{1}{2}(e_{23}+e_{32}) \\ \frac{1}{2}(e_{31}+e_{13}) & \frac{1}{2}(e_{23}+e_{32}) & e_{33} \end{bmatrix} \tag{4.48}$$

Once more there are only six independent components to this tensor so it is often written as a matrix in a similar way to the stress tensor above. In this case,

$$\begin{bmatrix} \epsilon_{11} & \epsilon_{12} & \epsilon_{31} \\ \epsilon_{12} & \epsilon_{22} & \epsilon_{23} \\ \epsilon_{31} & \epsilon_{23} & \epsilon_{33} \end{bmatrix} \rightarrow \begin{bmatrix} \epsilon_1 & \frac{1}{2}\epsilon_6 & \frac{1}{2}\epsilon_5 \\ \frac{1}{2}\epsilon_6 & \epsilon_2 & \frac{1}{2}\epsilon_4 \\ \frac{1}{2}\epsilon_5 & \frac{1}{2}\epsilon_4 & \epsilon_3 \end{bmatrix}. \tag{4.49}$$

The stress and strain matrices are linked via Hooke's Law,

$$\epsilon_i = S_{ij}\sigma_j, \tag{4.50}$$

where S_{ij} are the elastic moduli, or alternatively,

$$\sigma_i = C_{ij}\epsilon_j, \tag{4.51}$$

where C_{ij} are the elastic constants. In cubic materials (such as MgO or the other earth-metal oxides) there are only three independent elastic constants; C_{11}, C_{12} and C_{44}. This is now of the form,

$$C_{ij} = \begin{pmatrix} C_{11} & C_{12} & C_{12} & 0 & 0 & 0 \\ C_{12} & C_{11} & C_{12} & 0 & 0 & 0 \\ C_{12} & C_{12} & C_{11} & 0 & 0 & 0 \\ 0 & 0 & 0 & C_{44} & 0 & 0 \\ 0 & 0 & 0 & 0 & C_{44} & 0 \\ 0 & 0 & 0 & 0 & 0 & C_{44} \end{pmatrix}. \tag{4.52}$$

The final important relation needed by this work is that of the energy U necessary to induce the strain ϵ_i in the crystal. This is given by,

$$U = \frac{1}{2} V \sum_{i,j=1}^{6} C_{ij} \epsilon_i \epsilon_j, \tag{4.53}$$

where V is the volume of the crystal. The ϵ_i and ϵ_j are both the vector forms of the strain and the elastic constant tensor C_{ij} is of the form of equation (4.52) above.

Chapter 5

OTHER EARTH-METAL OXIDES

The CETEP codes have been successful in simulating the properties of magnesium oxide at equilibrium and at high pressure within the Earth's lower mantle. Continuing this the other earth-metal oxides CaO, SrO and BaO are now investigated. In this chapter these compounds will be introduced and previous experimental and theoretical work on them is discussed. The computer set-up for calculations involving these oxides is then described, followed by their equilibrium properties. After this the effect of using pseudopotentials generated from different electronic configurations is studied along with that of applying non-linear core corrections to the potentials. Finally the fully converged charge densities are examined to learn more about the bonding in these earth-metal oxides.

5.1 Introduction

As might be expected many of the physical properties of the earth metal oxides are much like those of MgO. With similar high melting points, low coefficients of

expansion and small thermal conductivities they have applications as thin-film substrates, optical materials and in microelectronics in the same way as MgO.

Unlike MgO, however, the other earth metal oxides are not found within the lower mantle and as a consequence their properties at high pressure are not of as much interest. Calcium silicon oxide (in its various forms) is found as a constituent of the Earth's lower mantle, but according to Duffy and Anderson (1989) the simple oxide is not present. As mentioned in chapter 4 there is a phase change from the rock salt B1 structure to the cesium chloride B2 structure in these oxides as pressure is applied. Jeanloz and Ahrens (1980) showed this transformation to exist in CaO at around 700 kbar (70 GPa) and Liu and Bassett (1972) demonstrated the same behaviour in BaO at pressures of only 140 kbar (14 GPa). As these are both much lower than the maximum pressure of 1.4 Mbar (140 GPa) found in the lower mantle it is unlikely that any earth-metal oxide, other than MgO, exists here in a rock salt structure.

In chapter 4 an investigation into the mechanism responsible for the Cauchy violation in MgO was carried out. The examination of the electron structure indicated that the *breathing* of the charge cloud around the oxygen ions is a likely cause of this behaviour. In both CaO and SrO the same effect is observed. However, although C_{44} is greater than C_{12} the difference between them is markedly less than for MgO. Finally in BaO the Cauchy violation is present but now C_{12} is greater than C_{44} so the sign of the violation has been reversed. The motivation for this study is to calculate the elastic constants of these oxides and to see if there is any basis for understanding the Cauchy violation as we move down the series. We shall find, however, that the conclusions draw are much more tentative than those made for MgO.

5.2 Previous work on CaO, SrO and BaO

Whereas many attempts have been made to calculate the physical properties of MgO there have been few similar calculations of the properties of the other earth-metal oxides. Two of the papers that were discussed in chapter 4 with respect to their predictions of the properties of magnesium oxide have also investigated the properties of calcium oxide. Cohen and Gordon (1976) made modified electron-gas (MEG) calculations of the equilibrium and high pressure properties of CaO as well as MgO. Mehl, Cohen and Krakauer (1988) also repeated their linearised augmented plane wave (LAPW) calculations of the electron structure of MgO for CaO. Apart from these two pieces of work introduced earlier Mehl, Hemley and Boyer (1986) used the empirical potential induced breathing (PIB) model to predict the physical properties of all the earth-metal oxides, and Mackrodt *et al* (1992) used a Hartree-Fock (HF) method to calculate the properties of a number of metal oxides including CaO. Some of the results from these papers are summarised in table 5.1.

In order to make a comparison table 5.1 also includes experimental values for the physical properties in question. The principal sources for the CaO data are the papers by Son and Bartels (1972); Chang and Graham (1977) and Dragoo and Spain (1977). As in chapter 4 these values were collated and averaged by Hearmon (1979). Sources for the SrO data include those above plus the papers of Johnston, Thrasher and Kearney (1970) and Pai and Sivertson (1976). Those for BaO also include Vetter and Bartels (1973) and Park and Sivertson (1975). Once again there is a spread in the experimental values. There is a difference of 1.3% between the value of C_{11} in CaO quoted by Dragoo and Spain (1977) of 226.2 GPa and that quoted by Chang and Graham (1977) of 221.9 GPa. Similar differences of 6.7% and 1.2% exist in the quoted values for, respectively, C_{12} and

		a_0/Å	B/GPa	C_{11}/GPa	C_{12}/GPa	C_{44}/GPa
CaO	expt	4.81	115	224	60	81
	PIB[a]	4.82	102	206	50	60
	MEG[b]	4.58 - 4.96	169 - 292	207 - 369	88 - 133	88 - 133
	LAPW[c]	4.71	129	-	-	-
	HF [d]	4.94	117	-	-	-
SrO	expt	5.16	87	170	46	56
	PIB[a]	5.13	80	171	34	49
BaO	expt	5.54	70	121	44	34
	PIB[a]	5.49	66	133	33	31

[a] Mehl, Hemley and Boyer, 1986.
[b] Cohen and Gordon, 1976.
[c] Mehl, Cohen and Krakauer, 1988.
[d] Mackrodt *et al*, 1992.

Table 5.1: Comparison of previous earth metal oxide calculations.

C_{44} in CaO. These discrepancies are magnified for the elastic constants of SrO and BaO. The spread about the mean value for the three elastic constants C_{11}, C_{12} and C_{44} is 2.9%, 17.4% and 14.3% for SrO and 11.6%, 31.8% and 5.9% for BaO. Some of these errors are quite large. When comparing calculated values to these experimental results it is necessary to bear these differences in mind. The reversal of the Cauchy violation in BaO is present in all three pieces of experimental work and is not merely a product of the averaging process.

It can be seen from table 5.1 that, as with MgO, good predictions are made of the lattice parameters of the other earth-metal oxides. The PIB model of Mehl *et al* (1986) is within 1% of the experimental value of the lattice parameter of all three oxides. The predictions made by the PIB model for the bulk modulus of the oxides range from 12% too large in the case of CaO to 8% too small in the case of SrO. It is a more modest 5% too small for the final case of BaO. The values of the individual elastic constants calculated by the PIB method vary considerably from their experimental counterparts. Most are 10% or more away

from the values given by Hearmon (1979). This could simply be a reflection of the inconsistencies in the data from the various experimental sources. The reversal of the sign of the Cauchy violation in BaO is, however, correctly predicted by the PIB calculations. The LAPW model of Mehl *et al* (1988) attempted to calculate the lattice parameter and bulk modulus of CaO only. The predictions from this method were about 2% too small for the lattice parameter and 12% too big for the bulk modulus. Although these errors are larger than those from the PIB model it should be remembered that the LAPW results for MgO were amongst the most accurate and they were considerably closer to experimental values than the corresponding PIB predictions. It is entirely possible that experimental errors are responsible for this seeming reversal of accuracy. As with MgO the MEG calculations of Cohen and Gordon (1976) provide a wide range of values for the physical parameters depending on which wave functions and how many nearest neighbours they allowed to interact. Relatively good predictions are made by this method for the lattice parameter. Values range from about 5% too small to 3% too big. This is considerably better than this technique achieved in its calculations on MgO. The results for the bulk modulus are much more disappointing. The smallest value is about 50% too large. The values of the individual elastic constants are equally far from experiment. Once again this method fails to predict the violation of the Cauchy condition in any of its calculations. The Hartree-Fock calculations of Mackrodt *et al* (1992) are quite close to experiment. Their prediction of the lattice parameter is $\sim$ 3% too large and the bulk modulus is also $\sim$ 3% away from experiment. Unfortunately no further physical properties of CaO were calculated in this work.

Hartree-Fock calculations of the band structure and density of states of the earth-metal oxides have been undertaken by Pandey, Jaffe and Kunz (1991). As with their MgO predictions it is not possible to make a comparison with their results

as these properties are not derived as part of this work.

5.3 Set-up on Computer

The pseudopotentials used to represent the metal ion in the earth-metal oxides are similar to those used in chapter 4 for magnesium oxide. To represent the oxygen ion the potential of Lin *et al* (1993) is used once more. This potential has already been successfully used in the MgO calculations. For the metal ions unoptimised norm-conserving pseudopotentials are used. These are generated in a similar manner to the magnesium potentials formulated in chapter 3. Initially non-linear core corrections are not applied to the pseudopotentials, but as we shall see later, they do play a significant role here.

Norm-conserving pseudopotentials generated by both the Hamann, Schlüter and Chiang (1979) and the Kerker (1980) methods are used in the following calculations. In the first instance the potentials are formulated from the same electronic configurations. As examples we shall discuss the HSC potentials in detail, but the Kerker potentials are similar. Figure 5.1 shows a calcium pseudopotential generated by the HSC method. To allow comparison the full bare-ion potential, $-2Z_v/r$ (the energy is in Rydbergs), is also shown on this figure. The configurations used to generate the individual angular momentum dependent components are those suggested by Bachelet, Hamann and Schlüter (1982). The $l = 0$ potential and wave functions are generated using the ground state of calcium ($4s^2$). For the $l = 1$ and $l = 2$ components the configuration $4s^{0.5}\ 4p^{0.25}\ 4d^{0.25}$ is used. The core radii used in the generation of this potential are 1.85 a.u. for the $l = 0$ term, 2.43 a.u. for the $l = 1$ term and 0.43 a.u. for the $l = 2$ term. This last core radius is very small indeed and leads to an $l = 2$ potential that is very hard-core

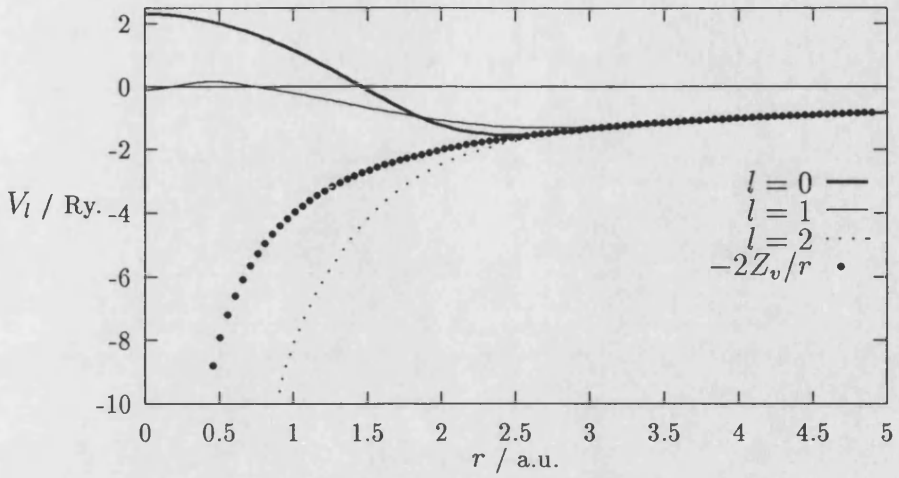

Figure 5.1: Ca pseudopotential generated using the HSC method.

in character.

All of the potential terms shown in figure 5.1 converge rapidly to the full potential close to the core radii. The $l = 0$ and $l = 1$ components of the potential are very soft at the origin. The $l = 2$ component, however, is considerably more hard-core in character. Although it is not shown in figure 5.1 the $l = 2$ potential finally reaches the origin at an energy of ~ -30 Ry. This is reminiscent of the unoptimised oxygen potential that was generated in chapter 3. It is likely that there is a similar cause for this behaviour. As with the p-state in oxygen, there are no electrons within the core of calcium that could be orthogonalised with valence d-electrons. When the energy convergence of this pseudopotential is examined it is no surprise that it is the $l = 2$ term that requires the largest energy cut-off. The convergence of the wave functions with respect to plane wave cut-off energy can be analysed in a similar way to chapter 3. The energy of this component is within 100 meV of the converged value if a cut-off of ~ 400 eV is used. This rises to ~ 600 eV when convergence to 10 meV is required. Finally an energy cut-off

of $\sim$ 800 eV is needed to bring it within 1 meV of convergence. These values are high, but they will not affect the calculations drastically. The Lin *et al* (1993) oxygen pseudopotential requires an energy cut-off of 1000 eV already.

Figures 5.2, 5.3 and 5.4 show the energy dependence of the logarithmic derivatives of the $l = 0$, $l = 1$ and $l = 2$ pseudo-wave functions of the calcium HSC pseudopotential. The solid line (marked AE) shows the corresponding results for the true all-electron potential. The derivatives are calculated at $r = 5.0$ a.u. for all angular momentum quantum numbers. The points marked HSC are for the potential generated by the Hamann, Schlüter and Chiang (1979) method and those marked KB are those resulting from the Kleinman and Bylander (1982) form of the same potential. The $l = 0$ term is chosen to be local, which explains why the KB and HSC curves are identical for this component. As can be observed from these figures there is reasonable agreement between the all-electron and the pseudo-logarithmic derivatives in the energy range studied. The $l = 2$ component is seen to deviate from the all-electron curve. This occurs at energies greater than $\sim$ 1 Rydberg. If these curves are compared with figures 3.4, 3.5 and 3.6, the equivalent curves for magnesium, it can be seen that the calcium logarithmic derivatives are not in as good agreement as was found before. This is probably to be expected as equation (3.1), which links the norm-conservation condition to the logarithmic derivatives, only ensures that the energy dependence is matched to first order at the atomic eigenvalue. Even with calcium the reproduction of the scattering properties is better than this over a wide energy range. It can also be observed that there are no ghost-states (see the paper by Gonze, Käckell and Schleffler, 1990, for details) present within the energy range examined.

Figure 5.5 shows the norm-conserving pseudopotential for strontium. Once again the method of Hamann, Schlüter and Chiang (1979) is used to generate the

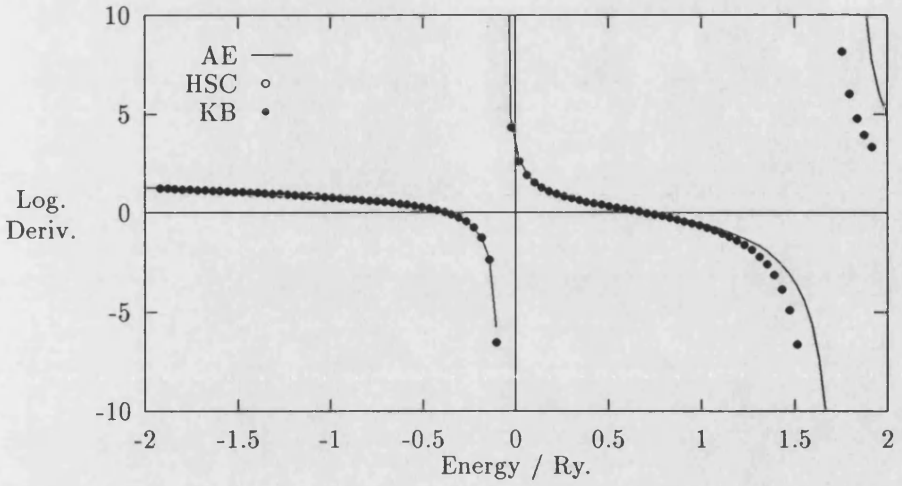

Figure 5.2: Logarithmic derivatives for $l = 0$ part of HSC potential for Ca.

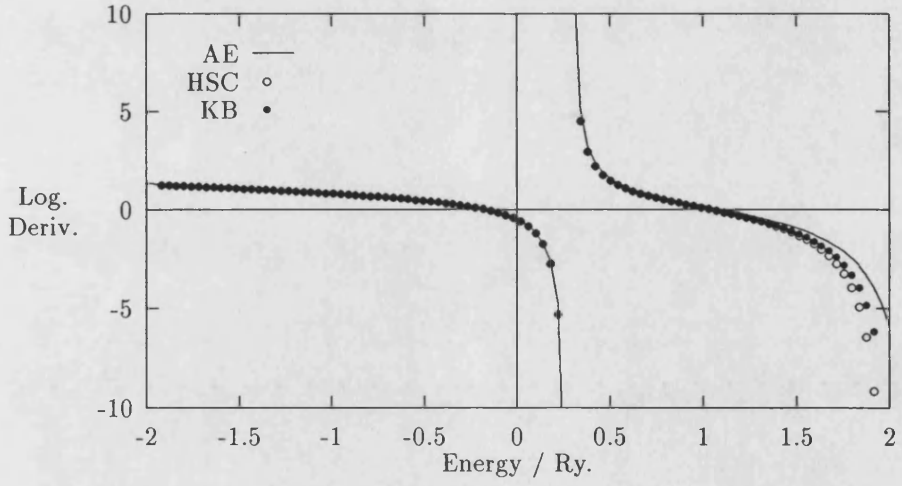

Figure 5.3: Logarithmic derivatives for $l = 1$ part of HSC potential for Ca.

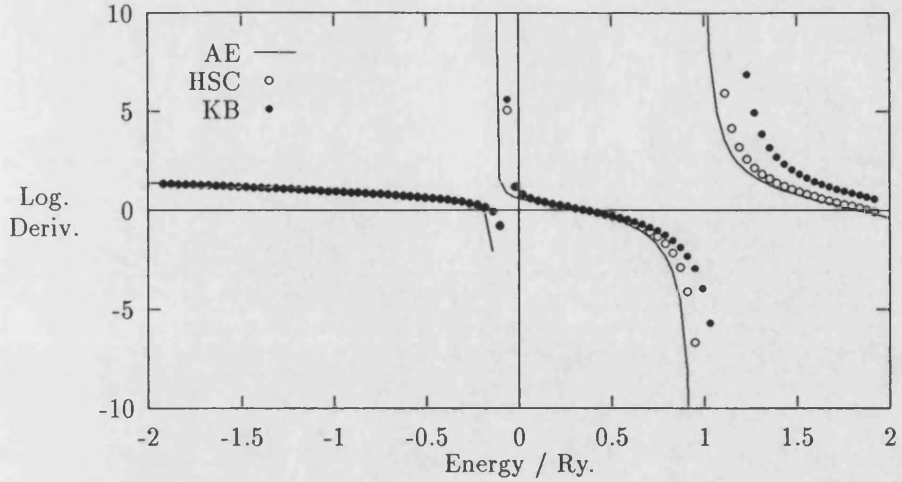

Figure 5.4: Logarithmic derivatives for $l = 2$ part of HSC potential for Ca.

pseudopotential. The ground state configuration ($5s^2$) is used to formulate the $l = 0$ component of the potential. The $l = 1$ and $l = 2$ components are generated from the configuration $5s^{0.5}\ 5p^{0.25}\ 5d^{0.25}$ as suggested by Bachelet, Hamann and Schlüter (1982). The core radii used in the generation of this potential are 2.01 a.u. for the $l = 0$ term, 2.53 a.u. for the $l = 1$ term and 1.22 a.u. for the $l = 2$ term. The $l = 2$ core radius is considerably larger than that used for calcium. This has the effect of allowing the relevant potential component to be much softer in character.

All of the potential terms are very soft and converge to the all-electron curve close to their core radii. As might be expected the cut-off energy required for convergence of this pseudopotential is very much smaller than that required for either the previous calcium potential or the Lin *et al* (1993) oxygen potential. Examination of the convergence data shows that the $l = 2$ component is the last to converge. This is probably because the $l = 2$ term is of greater magnitude than either of the other two terms. To obtain convergence to within 1 meV an energy

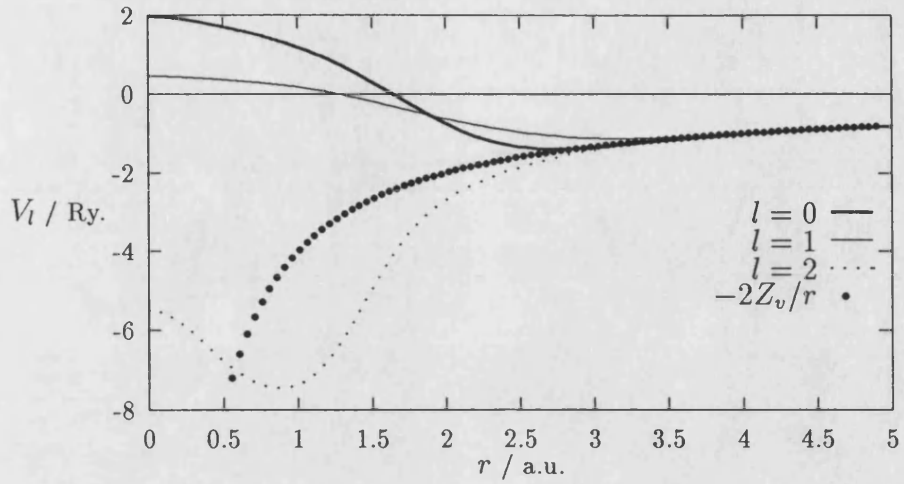

Figure 5.5: Sr pseudopotential generated using the HSC method.

cut-off of ~ 280 eV is required. As this energy is much smaller than the 1000 eV cut-off required by the oxygen pseudopotential there should be no problems with energy convergence if this potential is used in calculations.

Figures 5.6, 5.7 and 5.8 show the energy dependence of the $l = 0$, $l = 1$ and $l = 2$ pseudo-wave functions for the HSC strontium pseudopotential. The acronyms are the same as those for the previous logarithmic derivative curves. Once more the $l = 0$ term is taken as local and the HSC and KB curves for this component are identical. The derivatives are calculated at $r = 5.0$ a.u. for all angular momentum quantum numbers. The agreement between the pseudopotential curves and those from the all-electron calculation is once again reasonable, except at the high energy end of the range studied. Here there is a noticeable deviation from the all-electron curve by both the HSC and the KB data for all three components. Pseudopotentials generated by the Kerker method also exhibit this effect which is most marked for the KB form of the $l = 2$ term.

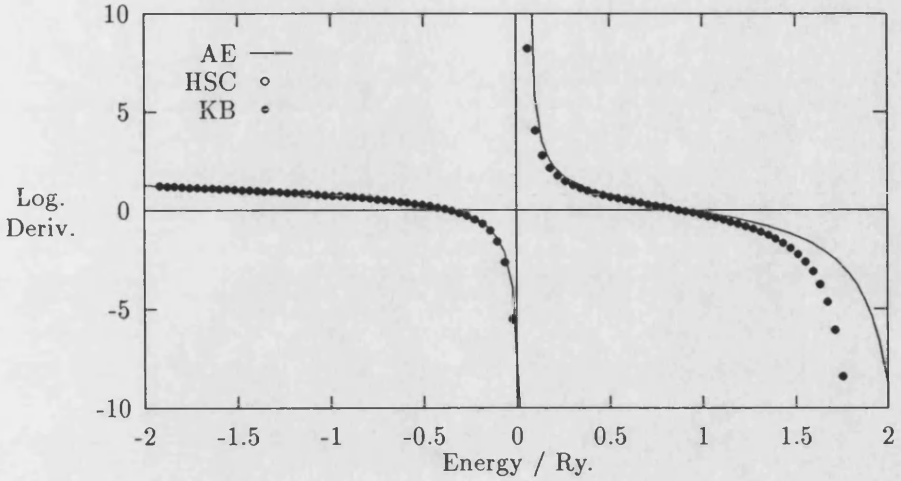

Figure 5.6: Logarithmic derivatives for $l = 0$ part of HSC potential for Sr.

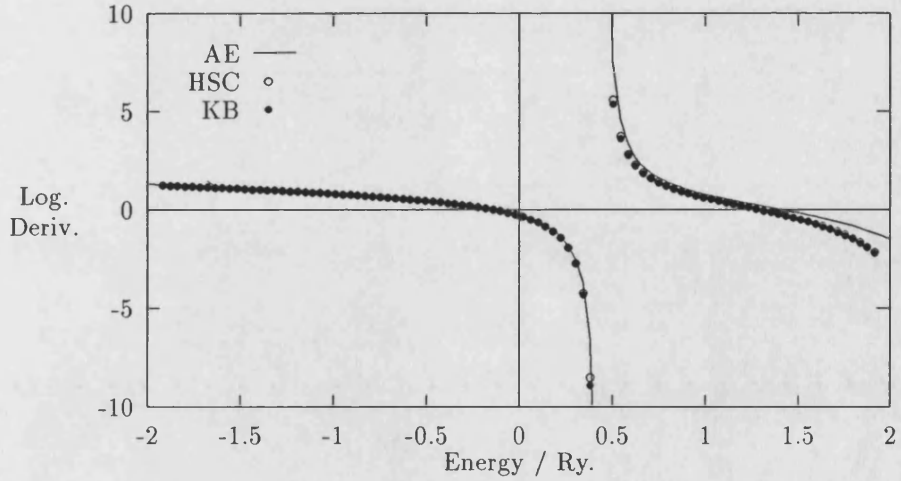

Figure 5.7: Logarithmic derivatives for $l = 1$ part of HSC potential for Sr.

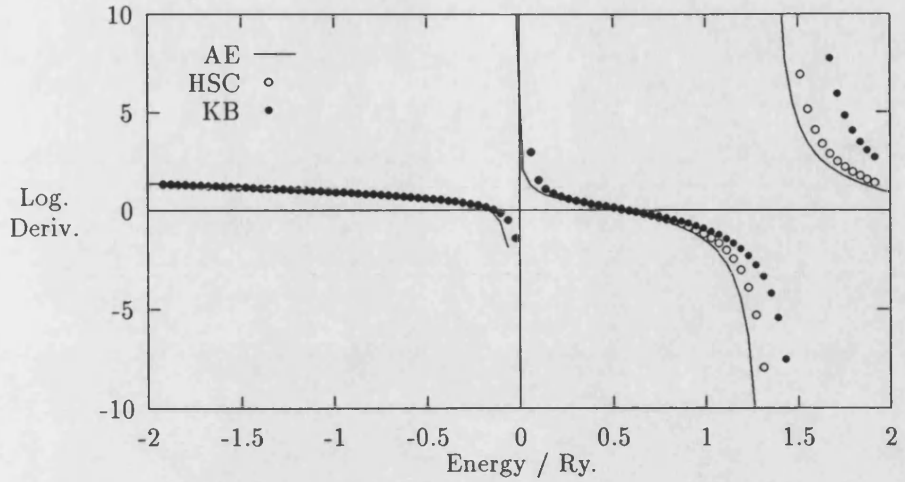

Figure 5.8: Logarithmic derivatives for $l = 2$ part of HSC potential for Sr.

Figure 5.9 shows the norm-conserving pseudopotential for barium generated, once more, by the method of Hamann, Schlüter and Chiang (1979). The ground state configuration of barium ($6s^2$) is used to formulate the $l = 0$ component of the pseudopotential. The other terms are generated according to the scheme of Bachelet, Hamann and Schlüter (1982). The $l = 1$ component is generated with the configuration $6s^{0.75}\ 6p^{0.25}$ and the $l = 2$ term is derived from the configuration $6s^{0.75}\ 6d^{0.25}$. Bachelet, Hamann and Schlüter (1982) recommend a configuration of $6s^{0.75}\ 6f^{0.25}$ to generate an $l = 3$ term for the pseudopotential. This is ignored as it is not expected that f-electrons will play any role in the behaviour of BaO and the CETEP codes are unable to handle an $l = 3$ component to the potential. The core radii used in the generation of this potential are 2.25 a.u. for the $l = 0$ term, 2.80 a.u. for the $l = 1$ term and 1.68 a.u. for the $l = 2$ term. These are all greater than their counterparts in the calcium and strontium pseudopotentials leading to softer potentials. Examination of figure 5.9 shows that this is indeed the case. Once again the individual potential terms converge on to the full potential close to their core radii.

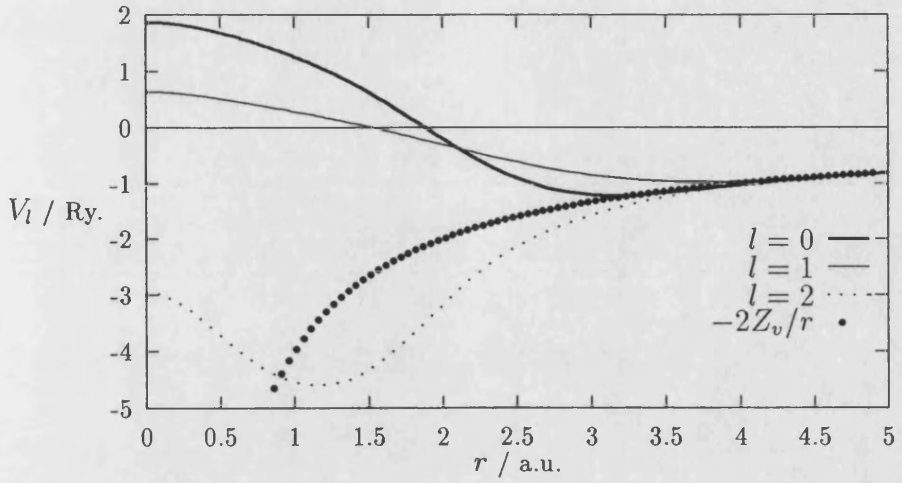

Figure 5.9: Ba pseudopotential generated using the HSC method.

The softness of all three potential terms leads to rapid convergence of the barium pseudopotential in terms of the energy cut-off. As with the other potentials it is the $l = 2$ component that is last to converge. This term is still the hardest so this is probably to be expected. Examination of the convergence data shows that the energy cut-off required by the barium pseudopotential are very small indeed. To achieve convergence to within 1 meV an energy cut-off of only $\sim$ 160 eV is needed. Once again this value shows that the pseudopotential should be very well converged when used in a calculation with an energy cut-off of 1000 eV.

Figures 5.10, 5.11 and 5.12 show the energy dependence of the logarithmic derivatives of the $l = 0$, $l = 1$ and $l = 2$ pseudo-wave functions of the HSC barium pseudopotential. The acronyms used are the same as before. The derivatives are calculated at $r = 5.0$ a.u. for all angular momentum quantum numbers and the $l = 0$ term is taken to be local. Once more there are no ghost-states to be found within the energy range studied. The agreement between the all-electron curve and the HSC and KB data is once more reasonable. The trend towards

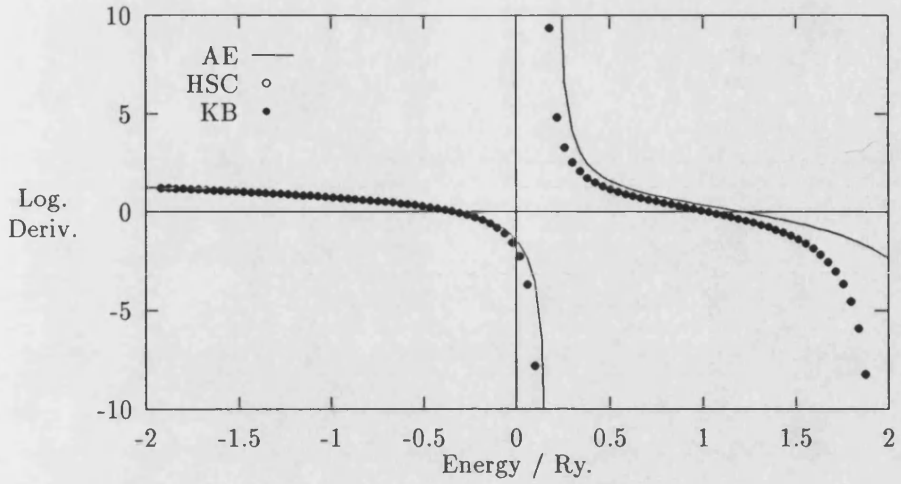

Figure 5.10: Logarithmic derivatives for $l = 0$ part of HSC potential for Ba.

inaccuracies at the higher energies continues. The $l = 2$ curve of the KB form of the pseudopotential is particularly badly behaved at energies greater than ~ 1 Rydberg. These results for HSC pseudopotentials are typical for all potential types. Similar differences between all-electron and pseudopotential logarithmic derivatives are found for potentials generated by the Kerker method also.

The earth-metal oxides all exist in a rock salt structure at equilibrium. This is face-centred cubic with a basis consisting of a metal ion and an oxygen ion. Figure 4.1 shows this structure. Experimental work (such as that by Jeanloz and Ahrens, 1980, or Liu and Bassett, 1972) has shown that these oxides exhibit a phase change to the cesium chloride structure when pressure is applied. The primitive lattice vectors **a** are similar to those for MgO and are given by equation (4.1). The lattice parameter a_0 of the full (cubic) cell is the only changing element. The only differences in structure between the oxides in the family are the increasing the lattice parameters as the metal ions get larger. Whereas MgO has an experimental lattice parameter of 4.21 Å, in CaO this is increased to 4.81

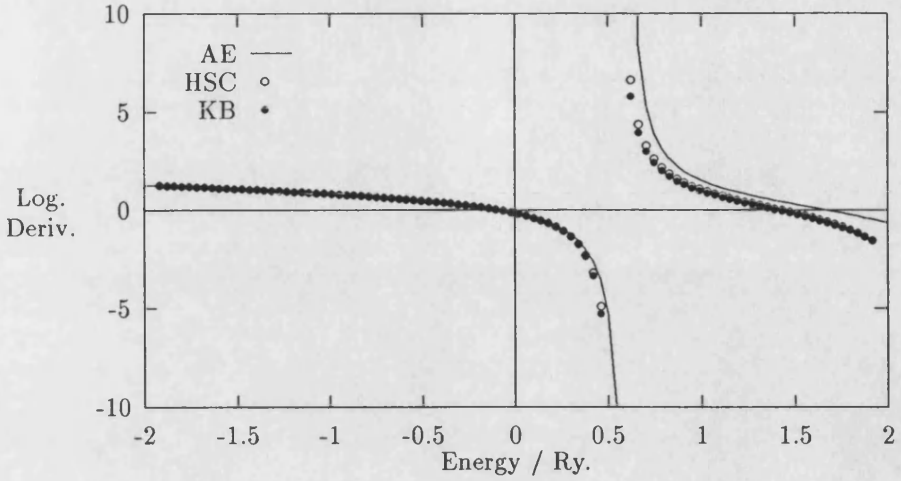

Figure 5.11: Logarithmic derivatives for $l = 1$ part of HSC potential for Ba.

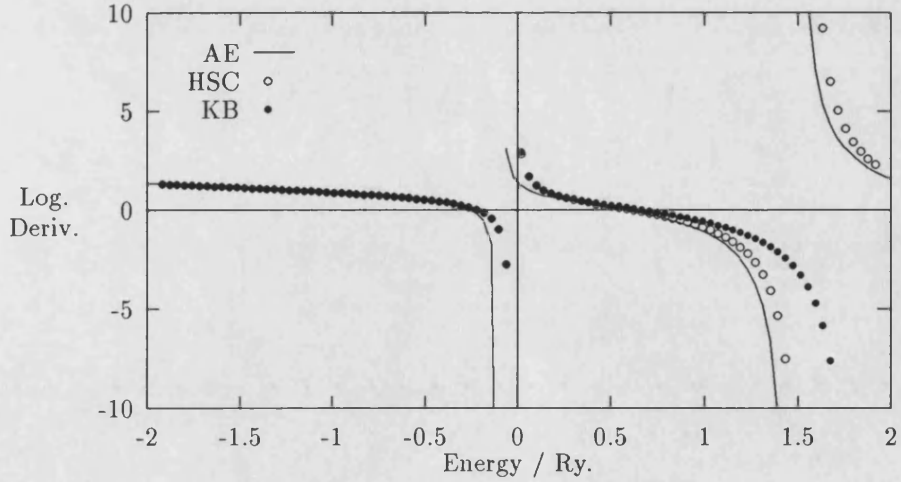

Figure 5.12: Logarithmic derivatives for $l = 2$ part of HSC potential for Ba.

Å, to 5.16 Å in SrO and finally it reaches 5.54 Å in BaO. The reciprocal lattice vectors **b** are also identical to those for MgO. These can be found from equation (4.2) in the previous chapter.

The same two sets of special **k**-points are used in calculations of these materials. Once again the sixteen point set is used for rigorous calculations, especially when monoclinic strains are present. The four point set is used for quick calculations at other times. The energy cut-off of 1000 eV is used again in order to properly converge the oxygen potential of Lin *et al* (1993). The reciprocal space grid is retained at $(32)^3$ for the calculations involving CaO and SrO. The increase in size of the unit cell forces the reciprocal space grid to be enlarged to $(36)^3$ for calculations on BaO. The calculations run with this set-up typically use between $\sim$ 2000 and $\sim$ 4000 plane waves per special **k**-point. The CETEP code is able to converge these within about fifteen iterations as before. Because of the increased number of plane waves in the calculation this takes a little longer than with MgO. On average a four **k**-point calculation now takes thirty minutes and a sixteen **k**-point calculation takes two hours to achieve convergence if sixteen nodes of the parallel surface are used.

5.4 Equilibrium Properties

As in chapter 4 the first calculations performed on the earth-metal oxides are those to establish their equilibrium lattice parameters. Table 5.1 shows that previous empirical calculations using the PIB model have been quite successful at predicting this parameter. *Ab initio* methods have only been used to study the properties of calcium oxide and on the whole they have not been so successful. With the exception of the MgO calculations discussed earlier there appears to

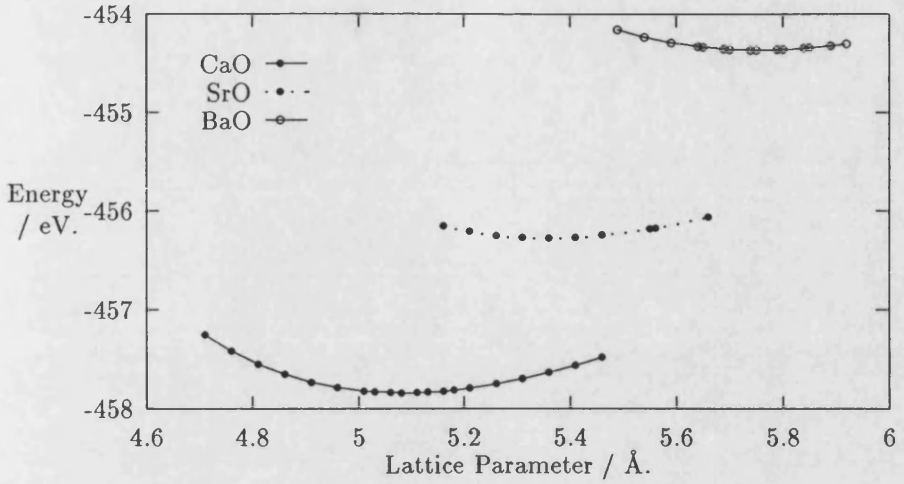

Figure 5.13: Total energy versus lattice parameter for the earth-metal oxides.

have been no published work on the earth-metal oxides involving pseudopotentials.

A series of total energy calculations are made for each material with the lattice parameter being varied over a range of values in each case. The full sixteen special **k**-point set is used for this calculation and the results are shown in figure 5.13. Initially the HSC type of pseudopotential is used to represent the metal ion. It can be seen from this figure that all the curves are, once again, very smooth. This indicates that all the pseudopotentials are well converged with respect to cut-off energy. A cubic polynomial is fitted through these data points in order to obtain the lattice parameter from these calculations. As with the magnesium oxide calculations performed in chapter 4 the maximum residuals from these fits are of order 5 meV. This is very small compared with the energy changes being studied confirming, once more, the smoothness of the data. As well as the lattice parameter the bulk modulus B is also be obtained from this data via the curvature at the equilibrium point. The results of both these calculations for all

	a_0/Å			B/GPa		
	expt.	calc.	error	expt.	calc.	error
CaO	4.81	5.08	+5.6%	115	92	-20.0%
SrO	5.16	5.36	+3.8%	87	77	-11.5%
BaO	5.54	5.75	+3.8%	70	64	-8.6%

Table 5.2: Lattice parameters and bulk moduli from HSC potential metal ions.

three materials are summarised in table 5.2.

It can be seen from table 5.2 that the results for these oxides are not as close to experiment as the results in chapter 4 for magnesium oxide. The lattice parameter predicted for CaO is $\sim$ 5.6% too large while the predictions for SrO and BaO are both $\sim$ 3.8% too big. These compare badly with the empirical calculations of Mehl, Hemley and Boyer (1986) (using a PIB model for their work) who obtained lattice parameters to within $\sim$ 1% of the experimental value. The theoretical calculations of Mehl, Cohen and Krakauer (1988) and Cohen and Gordon (these dealing only with CaO) are not so good, however. The bulk moduli shown in table 5.2 are also not as close to experiment as the MgO results. The value predicted for B in CaO is the furthest away probably reflecting the relative inaccuracy in the lattice parameter calculation. The values for the bulk moduli of SrO and BaO are rather closer to experiment and actually compare rather well with the predictions of the PIB model. All the bulk moduli are smaller than their experimental counterparts. This is a result consistent with the larger equilibrium volumes that have been calculated.

To establish the individual elastic constants calculations are made (as before with MgO) with various distortions placed on the unit cell about the calculated equilibrium position. Tetragonal and orthorhombic strains are required to isolate C_{11} and C_{12} while monoclinic and trigonal strains give a value for C_{44}. The results

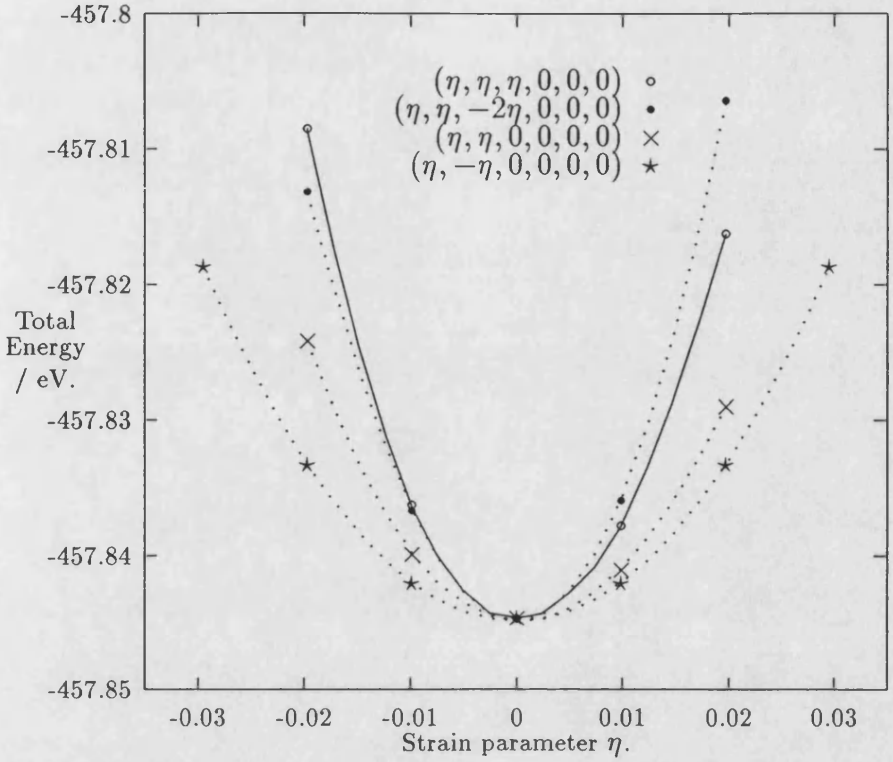

Figure 5.14: Total energy for tetragonal strains on CaO.

for the $\epsilon_i = (\eta,\eta,\eta,0,0,0)$, $\epsilon_i = (\eta,\eta,-2\eta,0,0,0)$, $\epsilon_i = (\eta,-\eta,0,0,0,0)$ and $\epsilon_i = (\eta,\eta,0,0,0,0)$ distortions are shown in figure 5.14 for calcium oxide. When these strains are substituted into equation (4.5) they give the strain energies U shown in equations (4.7), (4.10), (4.11) and (4.13) respectively. The curves displayed in figure 5.14 are all very smooth and the residuals are all of order ~ 5 meV indicating no energy convergence problems. As in chapter 4 the curvatures at equilibrium can be used to yield different combinations of the elastic constants C_{11} and C_{12}. Graphs can be drawn for tetragonal or orthorhombic strains on strontium oxide and barium oxide at equilibrium. These are very similar to the curves shown in figures 5.14 and 4.3. They also have small residuals (of order ~ 5 meV) when cubic polynomials are fitted through the data points.

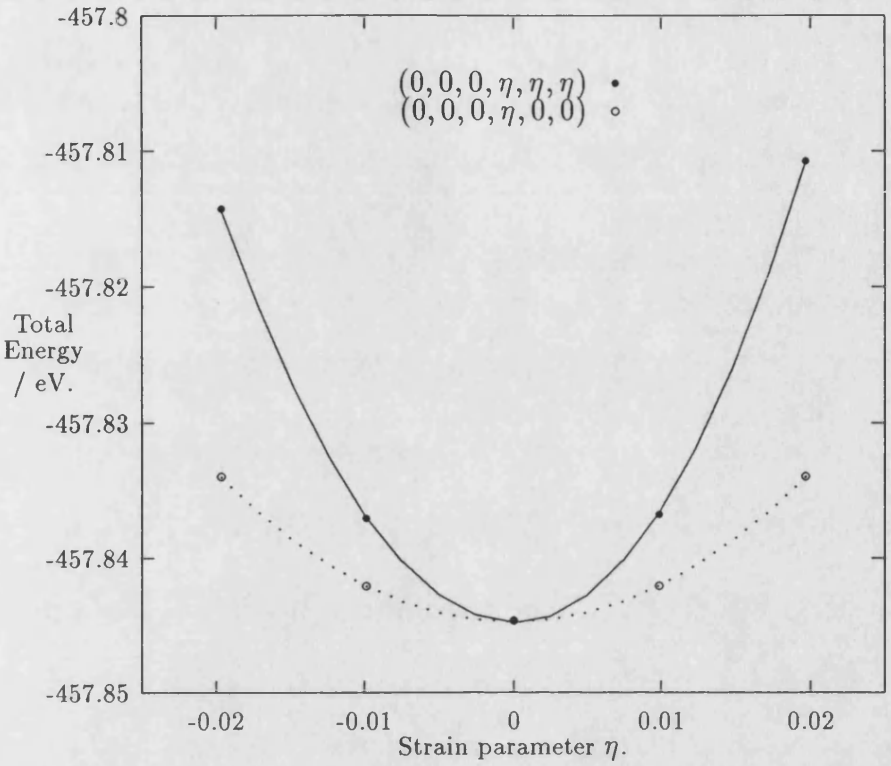

Figure 5.15: Total energy for monoclinic strains on CaO.

In a similar way to this the trigonal $\epsilon_i = (0,0,0,\eta,\eta,\eta)$ and the monoclinic $\epsilon_i = (0,0,0,\eta,0,0)$ distortions are also applied to the oxides at the calculated equilibrium position in order to establish the value of the final elastic constant C_{44}. The strain energies U associated with these distortions are given by equations (4.20) and (4.21) respectively in chapter 4. The results of calculations involving these strains on calcium oxide are shown in figure 5.15. Once again the curves described by these points are very smooth. When a cubic polynomial is fitted to this data the residuals are of order ~ 5 meV once more. Similar graphs can be drawn for the same strains applied to strontium oxide and barium oxide at equilibrium. Their residuals, when fitted with cubic polynomials, are of the same order of magnitude.

	C_{11}/GPa			C_{12}/GPa			C_{44}/GPa		
	expt.	calc.	error	expt.	calc.	error	expt.	calc.	error
CaO	224	188	-16.1%	60	43	-28.3%	80	68	-15.6%
SrO	170	156	-8.2%	46	35	-23.9%	59	65	+16.9%
BaO	121	134	+10.7%	44	28	-36.4%	35	45	+28.6%

Table 5.3: Elastic constants from HSC potential metal ions.

The curvatures at equilibrium of the data shown in figures 5.14 and 5.15 (and the similar results for SrO and BaO) are calculated and from these values the individual elastic constants are isolated. These are displayed in table 5.3 for all three materials along with their experimental counterparts. Once again there is excellent consistency in the values of the elastic constants calculated from these different strains. As can easily be seen from this table the values obtained for the individual elastic constants are not as accurate as those obtained for magnesium oxide in chapter 4. This is probably not surprising in the light of the generally poor lattice parameters and bulk moduli that have been calculated previously. All the predictions of the elastic constants shown in table 5.3 are between ten and twenty percent away from the experimental values. Typically LDA calculations obtain lattice parameters to within two or three percent and elastic constants to within ten percent or so. These results are generally worse than this. It is also disappointing that these results do not predict the reversal of the Cauchy violation in BaO that is shown by the experimental work. Given the large errors in the calculated values of C_{12} and C_{44} it would be difficult to draw any physical conclusions from the data anyway. In comparison the PIB calculations of Mehl, Hemley and Boyer (1986) for BaO do manage just to show this reversal of the violation. However, as their prediction for C_{12} is $\sim$ 25% smaller than the experimental value it is perhaps difficult to believe that they are correctly describing the physics of BaO.

	a_0/Å			B/GPa		
	expt.	calc.	error	expt.	calc.	error
CaO	4.81	5.08	+5.6%	115	109	-5.2%
SrO	5.16	5.36	+3.8%	87	79	-9.2%
BaO	5.54	5.80	+4.7%	70	69	-1.4%

Table 5.4: Lattice parameters and bulk moduli from Kerker potential metal ions.

The results obtained for the earth-metal oxides have been rather inaccurate in calculations using an HSC metal pseudopotential and the Lin *et al* (1993) oxygen pseudopotential. Examination of figures 5.1 to 5.12 reveals that the logarithmic derivatives for these metals are not as good as for the corresponding magnesium pseudopotentials shown in figures 3.4, 3.5 and 3.6. This is especially true for the $l = 2$ components. It is possible that poor transferability is at the root of the problems. By switching to metal pseudopotentials formulated by the Kerker method (generated from the same configurations as the HSC potentials used already) it is possible to recalculate the basic properties of the earth-metal oxides. In this way it can be confirmed that the properties of the HSC and Kerker potentials are similar. All parts of the calculation (the oxygen potential, the energy cut-off, the k-space box, etc.) are kept the same as in the previous case with the exception of the metal pseudopotentials for which the Kerker method potential is now used. The lattice parameters and bulk moduli obtained from these calculations are shown in table 5.4.

It can be seen from table 5.4 that changing the metal pseudopotential has produced some differences to the predicted values of these physical parameters. The lattice parameters of CaO and SrO are virtually indistinguishable from the values obtained using the HSC potentials. The result for BaO is slightly larger than for the corresponding HSC calculation. When the bulk modulus predictions are examined, however, there are some changes in the Kerker results compared to those

	C_{11}/GPa			C_{12}/GPa			C_{44}/GPa		
	expt.	calc.	error	expt.	calc.	error	expt.	calc.	error
CaO	224	195	-12.9%	60	66	+10.0%	80	67	-16.9%
SrO	170	164	-3.5%	46	37	-19.6%	59	58	-1.7%
BaO	121	150	+24.0%	44	29	-34.1%	35	44	+25.7%

Table 5.5: Elastic constants from Kerker potential metal ions.

for the HSC potentials. In calcium oxide B is now 109 GPa compared with 92 GPa in the HSC calculations and the experimental value of 115 GPa. The Kerker result is now only 5% smaller than experiment. There is a similar improvement in B for SrO (to within 10% of experiment) and BaO (now only $\sim$ 1% from experiment). All of the bulk moduli are now within the sort of error that is usual with LDA calculations. The lattice parameters are still a little disappointing in this respect. In two cases the error in lattice parameter is now greater than the error in bulk modulus.

Table 5.5 shows the individual elastic constants calculated using the Kerker pseudopotentials. As with the lattice parameters and bulk moduli above there is a broad agreement between the results obtained with the Kerker potentials and those from the HSC potentials, certainly to within the usual limits of LDA calculations. In fact the only significant change is the value of C_{12} in CaO. Even in this case the predicted values of $C_{11} - C_{12}$ are very much closer together. The agreement with experiment is, however, rather worse than that which is typical of LDA calculations. This could be due, as mentioned previously, to poor transferability of the pseudopotentials. This is now tested by trying different configurations in the generation of Kerker pseudopotentials.

5.5 Ionised Potentials

The results so far for the earth-metal oxides have been disappointing when compared to those achieved for MgO in chapter 4. As mentioned above this might be due to the poor transferability of the norm-conserving pseudopotentials used in these calculations. If the pseudopotentials cannot be trusted to be fully transferable then may be necessary to generate new potentials based on electronic configurations closer to that which the ion is expected to possess after bonding. In particular the $l = 0$ component of the potential can be reformulated from an ionised configuration rather than the ground-state atomic configuration suggested by Bachelet, Hamann and Schlüter (1982).

5.5.1 Ionised s component

In chapter 4 examination of the real space charge density patterns (such as figure 4.11) showed that the magnesium ion was ionised to a configuration of at least $Mg^{1.3+}$. Similar inspection of the charge densities in reciprocal space (see figure 4.13) revealed that the valence charge could be represented entirely by charge density objects centred on the oxygen ion sites. In other words the magnesium ions could be completely ionised to a $Mg^{2.0+}$ state. To take this into account when formulating an ionised calcium pseudopotential the $l = 0$ part of the potential is generated using a configuration of $4s^{0.5}$. This is a $Ca^{1.5+}$ state. Figure 5.16 shows the $l = 0$ part of a calcium pseudopotential generated in this way. The core radius used for this calculation is 2.87 a.u. For comparison the $l = 0$ part of the calcium pseudopotential generated by the Kerker method from the ground state ($4s^2$) configuration (the core radius for this potential is 3.02 a.u.) is shown also along with $-2Z_v/r$ the full bare-ion potential (with the energy measured in

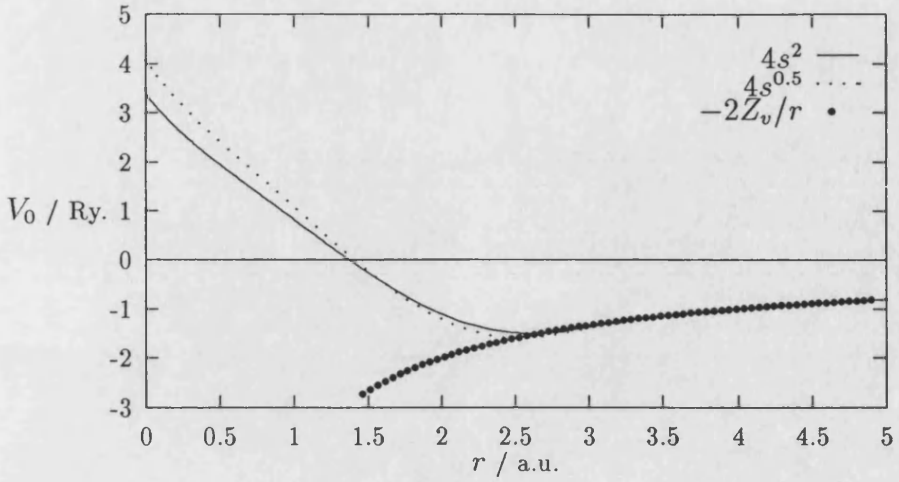

Figure 5.16: $l = 0$ component of Kerker calcium potentials.

Rydbergs).

The two potentials shown in figure 5.16 are broadly similar in form. The ionised pseudopotential has a slightly greater magnitude at the origin and converges onto the coulomb repulsion curve a little before the potential generated from the calcium ground state. This is to be expected as the core radius of the ionised pseudopotential is slightly smaller than that of the ground state potential. Examination of the wave function kinetic energy reveals that the $l = 0$ term is the slowest to achieve convergence with respect to energy cut-off. This is repeated in all earth-metal pseudopotentials generated by the Kerker (1980) method as opposed to HSC potentials in which the $l = 2$ term is often the last to be fully converged. The kinetic energy reaches to within 100 meV of convergence if an energy cut-off of only 10 eV is used. This rises to 40 eV if convergence to within 10 meV is required and 100 eV for convergence as close as 1 meV. These figures are very similar to the values (10 eV, 40 eV and 70 eV; respectively) that are needed for similar levels of convergence with the Kerker pseudopotential gen-

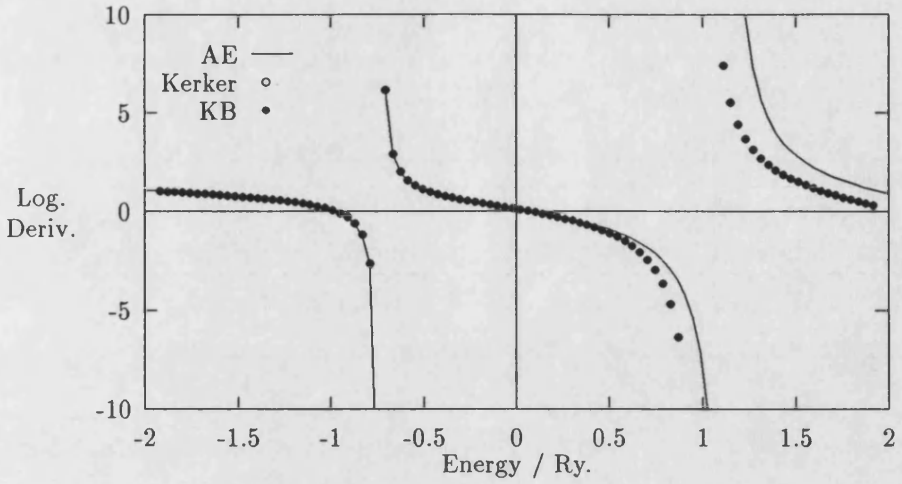

Figure 5.17: Logarithmic derivatives for $l = 0$ part of ionised Ca potential.

erated from the ground state configuration. Both these sets of cut-off energies are obviously much less than the 1000 eV value required by the Lin *et al* (1993) oxygen potential.

Figure 5.17 shows the energy dependence of the logarithmic derivatives for the $l = 0$ pseudo-wave functions of the new pseudopotential. As in other similar figures the derivatives are calculated at $r = 5.0$ a.u. The $l = 0$ component is taken as local when converting to the Kleinman and Bylander (KB) form so there is no difference in the energy dependence of it and the straight Kerker form. On this occasion the all-electron (AE) data is calculated using the calcium $4s^{0.5}$ configuration rather than the ground state used for comparison in figure 5.2 above.

The total energy of calcium oxide is now calculated over a wide range of cell volumes using the new ionised pseudopotential to represent the calcium ion. All other parts of the calculation (such as energy cut-off, k-space box size, special k-

	a_0/Å	B/GPa	C_{11}/GPa	C_{12}/GPa
expt.	4.81	114	224	60
BHS	5.08	109	195	66
error	+5.6%	-5.2%	-12.9%	+10.0%
1.5+	4.82	113	245	48
error	+0.2%	-1.2%	+9.2%	-20.8%

Table 5.6: Physical properties of CaO from calcium pseudopotentials generated from the BHS and 1.5+ ionised configurations.

point set, etc.) are kept the same as for the earlier computations used to establish the data for calcium oxide shown in figure 5.13.

When the data is analysed it provides the predictions for the physical parameters a_0 and B of CaO shown in table 5.6. The values obtained in the earlier calculation based on potentials generated from the BHS configuration are included for comparison along with the experimental results. It can be seen immediately that use of the new ionised pseudopotential has significantly changed the predictions made. The errors shown (0.2% in the lattice parameter and 1.2% in the bulk modulus) are even smaller than those obtained for MgO in chapter 4.

As these predictions for two properties of CaO using an ionised Ca pseudopotential are changed from those obtained before it is now necessary to make new calculations of the values of the individual elastic constants. In a similar way to before tetragonal and orthorhombic distortions are placed on the unit cell at equilibrium. The curvatures obtained around this point are then related, once again, to different combinations of the constants C_{11} and C_{12}. As in previous cases there is excellent internal consistency between the results obtained here. For example the $\epsilon_i = (\eta, \eta, -2\eta, 0, 0, 0)$ distortion and the $\epsilon_i = (\eta, -\eta, 0, 0, 0, 0)$ distortion are both related to the value of $C_{11} - C_{12}$. In the former this is 197.7 GPa and in the latter it becomes 197.0 GPa. The results of these calculations

are also shown in table 5.6 along with values derived earlier from the BHS configuration potential. There is no evidence of improvement in the results derived this time. Although the prediction of the value for C_{11} is slightly better than that of the BHS pseudopotential this is compensated by the more disappointing prediction of C_{12}. The use of the ionised calcium potential has resulted in large changes in the predictions made of the physical properties of CaO. These changes have actually lead to very good predictions for the lattice parameter and bulk modulus. There has not been, however, a similar improvement in the predictions of the elastic constants C_{11} and C_{12}.

This technique of using ionised configurations when generating the $l = 0$ term of a metal pseudopotential is now applied to strontium and barium. At first the same (1.5+) ionised state is used to generate the $l = 0$ components of the potentials. For strontium this is the $5s^{0.5}$ and for barium it is $6s^{0.5}$. Calculations are now made with these potentials to establish the lattice parameters and bulk moduli. The results of this are shown in table 5.7 along with the experimental and BHS values. The pattern seen in the CaO calculations is repeated here with the lattice parameters becoming smaller while the bulk moduli increase. In these cases, however, the change moves both lattice parameter predictions too far and they are now around three percent smaller than the experimental value. The bulk moduli have also overshot the experimental values. They do, in fact, become very much larger than expected. In the case of BaO over sixty percent too large.

The use of 1.5+ ionised potentials have taken the lattice parameter in the direction of the experimental value, but much too far. To produce a prediction closer to the experimental value than this it seems reasonable to try some calculations with less ionised pseudopotentials. In a similar way to before two further strontium pseudopotentials are created from the electronic configurations $5s^{0.8}$ (to produce

		a_0/Å			B/GPa		
		expt.	calc.	error	expt.	calc.	error
SrO	BHS	5.16	5.36	+3.8%	87	79	-9.2%
	0.75+		5.27	+2.1%		87	-0.7%
	1.2+		5.15	-0.2%		101	+16.1%
	1.5+		5.01	-2.9%		126	+44.8%
BaO	BHS	5.54	5.80	+4.7%	70	69	-1.4%
	0.75+		5.69	+2.7%		80	+14.3%
	1.5+		5.35	-3.4%		117	+67.1%

Table 5.7: Physical properties of SrO and BaO with pseudopotentials generated from ionised configurations.

a $Sr^{1.2+}$ potential) and $5s^{1.25}$ (for a $Sr^{0.75+}$ potential). Calculations are now made of the lattice parameter and bulk modulus of SrO using these potentials. The predictions obtained from this are shown on table 5.7 along with the data already discussed. Examining all the values reported here it is obvious that the greater the ionicity of the potential the smaller the lattice parameter and the larger the bulk modulus are predicted. Unlike the previous case with CaO a prediction of the lattice parameter close to experiment is made with a different potential (the 1.2+ one) than that which makes the prediction of the bulk modulus that was nearest to the experimental value (the 0.75+ one). Within the bounds of accuracy acceptable in an LDA calculation (within one or two percent for the lattice parameter and five to ten percent for the bulk modulus) it is obviously possible to manufacture a strontium pseudopotential that will make reasonable predictions of these physical properties in SrO. Unfortunately, as demonstrated earlier in CaO, this is no guarantee that other properties (such as the shear modulus, $(C_{11} - C_{12})/2$) will also be accurately predicted. It is difficult to have a great deal of confidence that the physics of SrO is being correctly reproduced by any of these strontium pseudopotentials.

A similar pattern emerges when calculations are made with a 0.75 barium pseu-

dopotential (the configuration used in generating the $l = 0$ component being $6s^{1.25}$). These results are also shown in table 5.7. Although the new prediction for the lattice parameter (5.69 Å) is smaller as expected than that obtained using the BHS potential, it is still $\sim 2.7\%$ larger than the experimental value. This is contrasted with the bulk modulus which has already overshot the experimental value by $\sim 14.3\%$. In order to improve these predictions it is necessary to use a potential ionised to a greater degree than 0.75+ (1.0+ say) while a good prediction of the bulk modulus could be obtained from a potential that has only a small degree of ionisation, if any at all. Unlike the ionised strontium potentials investigated earlier there is now no degree of ionisation that results in reasonable values for both the lattice parameter and bulk modulus of BaO. There seems very little hope that any of these potentials would produce good predictions for the shear modulus or any other physical parameters.

These results have demonstrated a shocking lack of transferability in both HSC and Kerker pseudopotentials for calcium, strontium and barium. By varying the configuration used in the generation of the pseudopotentials it is possible to obtain almost any prediction for the lattice parameter and bulk modulus of the respective oxide. It is necessary to apply the same techniques to magnesium to see if the same effects can be observed. A magnesium pseudopotential is generated using the Kerker method with the $l = 0$ term formulated with an electron configuration of $3s^{0.5}$. This produces a 1.5+ ionised potential similar to those already used for the other earth-metal oxides. When total energy calculations are made for MgO using this new potential the lattice parameter is found to be at 4.16 Å ($\sim 1.2\%$ too small) and the equilibrium bulk modulus is 172 GPa ($\sim 7.5\%$ too large). This is the same pattern that has been seen already with the other earth-metal oxides. The ionisation of the $l = 0$ component of the pseudopotential results in the lattice parameter becoming smaller while the bulk modulus increases. Compared to the

earlier effects, however, it is very much smaller for the case of MgO and the answers obtained are very reasonable predictions for these physical properties. This shows that the basic Mg pseudopotentials are far more transferable than those of the other earth-metals. It is important that this is the case so that the results obtained for magnesium oxide in the previous chapter are in no way invalidated.

5.5.2 Ionised p and d components

It has been observed that changing the ionicity of the $l = 0$ component of the metal pseudopotential can have a profound effect on the properties predicted for the metal oxide. This must be a symptom of poor transferability in this term. Examination of the logarithmic derivatives of the calcium, strontium and barium potentials reveals that although the $l = 0$ terms are not of the same standard as that for magnesium it is in the $l = 1$ and $l = 2$ components that large differences are to be found with respect to the all-electron calculations. It is now necessary to test the transferability of the $l = 1, 2$ terms as well.

Calcium pseudopotentials are generated with the $l = 1, 2$ terms taken from the electronic configurations $4s^0\ 4p^{0.25}\ 4d^{0.25}$ and $4s^0\ 4p^{0.1}\ 4d^{0.1}$. The core radius is 3.51 a.u. for the $l = 1$ components of both potentials. This is identical to that used by the original Kerker potential generated from the BHS configuration. In the $l = 2$ term the core radii are 5.23 a.u. for the $4s^0\ 4p^{0.1}\ 4d^{0.1}$ potential, 5.50 a.u. for the $4s^0\ 4p^{0.25}\ 4d^{0.25}$ potential compared with 6.06 a.u. for the original BHS configuration potential. The wave functions used in the formulation of these potentials are examined to establish the cut-off necessary for energy convergence. In all cases convergence to within 1 meV is achieved with an energy cut-off of

	a_0/Å	B/GPa	C_{11}/GPa	C_{12}/GPa
expt.	4.81	114	224	60
BHS	5.08	109	195	66
error	+5.6%	-5.2%	-12.9%	+10.0%
$p^{0.25}d^{0.25}$	4.95	113	214	63
error	+2.9%	-1.5%	-4.5%	+5.0%
$p^{0.1}d^{0.1}$	4.87	115	243	50
error	+1.2%	+0.3%	+8.1%	-17.2%

Table 5.8: Physical properties of CaO with pseudopotentials generated from $l = 1, 2$ ionised configurations.

$\sim$ 50 eV for both the $l = 1$ and $l = 2$ components of the potential. This is less than that required to obtain a similar degree of convergence for the $l = 0$ term ($\sim$ 100 eV) and considerably smaller than the cut-off of 1000 eV that is necessary when used in calculations involving the Lin *et al* (1993) oxygen pseudopotential. Once more the lattice parameter and bulk modulus of CaO is computed using these newly generated calcium pseudopotentials. The results are this are shown in table 5.8 along with the experimental and BHS values.

The ionisation of the p and d terms of the calcium pseudopotential has, once more, forced the lattice parameter to decrease and the bulk modulus to increase. The effect is very much smaller than that observed in the previous calculations with s term ionised potentials. A further set of calculations is made to isolate the individual elastic constants. These results are also shown in table 5.8. As in previous examples the consistency between the predictions of the individual distortions is very good.

	a_0/Å	B/GPa
expt.	4.81	114
BHS	5.08	109
error	+5.6%	-5.2%
$s^{0.1}p^{0.1}d^{0.1}$	4.47	180
error	-7.1%	+56.9%

Table 5.9: Physical properties of CaO from a pseudopotential with all three components generated from ionised configurations.

5.5.3 Potentials with all components ionised

One further step is to generate a calcium pseudopotential in which all three components are highly ionised. If the pattern discerned earlier is followed this new potential should predict a lattice parameter that is smaller than that found experimentally with a bulk modulus that is correspondingly larger. Even though these are unlikely to produce predictions that are very close to the experimental values, they will make an interesting comparison point for the core corrected calculations in section 5.6. The calcium pseudopotential is generated with the same configuration $4s^{0.1}4p^{0.1}4d^{0.1}$ for all three terms. The core radii are 2.87 a.u. for the $l = 0$ term, 3.51 a.u. for the $l = 1$ term and 5.23 for the $l = 2$ term. As with other similar potentials it is the $l = 0$ component that requires the greatest energy cut-off for convergence. Examination of the wave functions reveals that a cut-off of only $\sim$ 100 eV is necessary to achieve convergence to within 1 meV. Once more a series of calculations is made to establish the lattice parameter and bulk modulus of CaO. The results derived from these calculations are shown in table 5.9.

It can be seen from these results are broadly in line with those that had been expected. The lattice parameter of 4.47 Å is the smallest yet predicted for CaO while the bulk modulus of 180 GPa is the largest. As it is difficult to ionise the

electronic configurations used in the generation of this pseudopotential (there are only 0.3 electrons remaining split between the three components) these predictions can be seen as limiting values of those that can be obtained by altering the ionicity.

It is obvious that by altering the number of electrons in the configuration used to generate the pseudopotential that a very wide range of results can be obtained for the properties of calcium oxide and other similar oxides. This is extremely inconvenient in a supposedly *ab initio* technique. It is not even possible to empirically *fit* a potential to produce good results. A potential that will make a good prediction for the lattice parameter or even the bulk modulus of the oxide will invariably fail to make a correctly reproduce the rigidity modulus or the individual elastic constants. The problem seems to be the poor transferability of calcium, strontium and barium pseudopotentials compared with the good transferability obtained for magnesium potentials. To investigate what is causing this it is necessary to apply non-linear core corrections to the pseudopotentials.

5.6 Core corrected Calculations

The most obvious difference between magnesium and the other earth-metals is the increase in the size of the ion itself. Whereas magnesium has only three core orbitals, calcium possesses five, strontium eight and barium eleven. These extra core electrons make the neutral atoms occupy a much larger volume than the magnesium core. This will obviously affect the behaviour of the oxides. Pseudopotential theory assumes (plausibly) that the atom cores are *frozen* and contribute little towards the physical properties. The main changes between the earth-metal pseudopotentials derive from the larger radii of the extremum

of the valence electron wave functions. As the size of the frozen core increases the possibility of overlap between the core charge density and the valence charge density increases also. In particular the volume of core and valence overlap region increases quickly. These are precisely the conditions in which non-linear core corrections (see section 3.7) are important. When overlap occurs between the core and valence charge density systematic errors can creep into the exchange and correlation term of the energy due to the non-linearity in the charge density when the local density approximation (LDA) is used. This error can be rectified by adding the core density to the valence density when the exchange and correlation energy is calculated in the manner described in chapter 3.

5.6.1 Core corrections from BHS configurations.

Core corrected pseudopotentials for calcium, strontium and barium are generated in the same manner as the magnesium potential in section 3.7. As in the previous example the Kerker (1980) method is used in the formulation process along with the Bachelet, Hamann and Schlüter (1982) (BHS) electron configurations. For the calcium potential the $l = 0$ component is generated from the ground state ($4s^2$). The $l = 1$ and $l = 2$ terms are derived from the configuration $4s^{0.5}$ $4p^{0.25}$ $4d^{0.25}$. This leads to pseudopotential core radii of 3.02 a.u., 3.51 a.u. and 6.08 a.u. respectively. The radius r_0 used to cut off the core charge density is 2.47 a.u. The core corrected calcium pseudopotential is shown in figure 5.18. All parts of the potential are soft in character around the origin in contrast to the $l = 2$ term of the HSC-type calcium potential shown in figure 5.1. The $l = 0$ and $l = 1$ components both converge onto the bare ion curve close to their respective core radii. The $l = 2$ term is still not quite converged in this figure due to the size of its core radius which is slightly out of the range shown. Examination of the wave

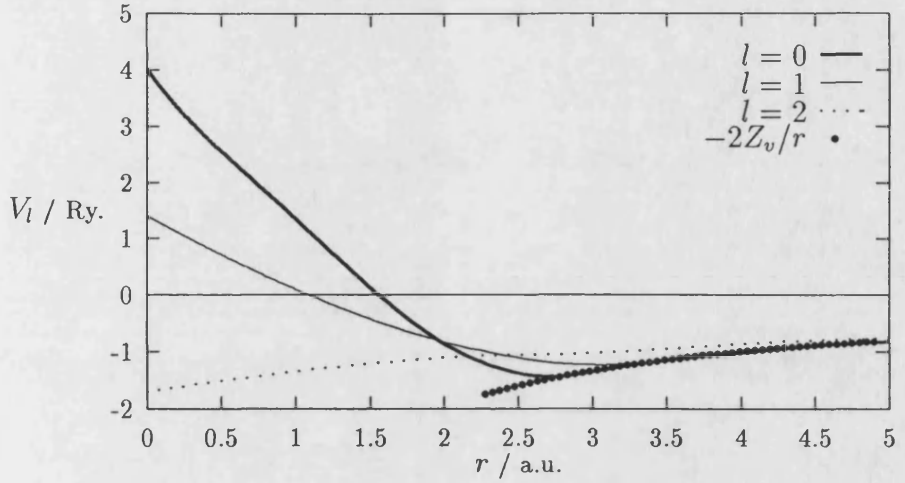

Figure 5.18: Ca pseudopotential with core corrections.

functions reveals that (as for the other Kerker-type earth-metal pseudopotentials) it is the $l = 0$ term that is last to reach energy convergence. In this case the wave function energy is within 1 meV of full energy convergence for a cut-off of only ~ 70 eV.

The strontium pseudopotential is generated in a similar manner. Once again the BHS electronic configurations are used. The ground state ($5s^2$) is used to formulate the $l = 0$ component while the configuration $5s^{0.5}\ 5p^{0.25}\ 5d^{0.25}$ is used for the other two terms. The core radii produced from this are 3.36 a.u., 4.11 a.u. and 7.12 a.u. respectively. The value of r_0 used to cut off the core charge density is 2.89 a.u. This pseudopotential is shown in figure 5.19. Its general form it is quite similar to the calcium core corrected potential displayed above in figure 5.18. Once again it is soft core in character and the $l = 0$ and $l = 1$ components are fully converged with the bare ion curve around their respective core radii. As in the previous case the convergence of the $l = 2$ term is delayed by the size of the core radius. The $l = 0$ wave functions are the last to achieve energy convergence.

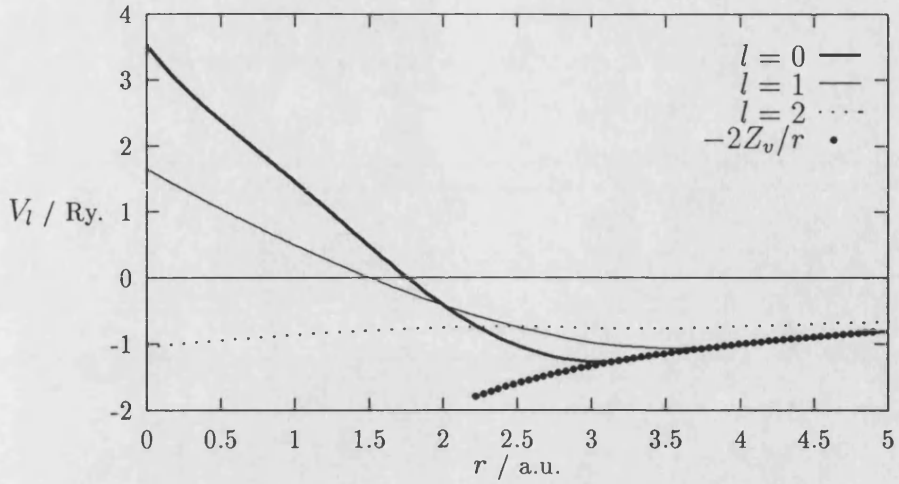

Figure 5.19: Sr pseudopotential with core corrections.

Inspection shows that they are within 1 meV of full convergence when an energy cut-off of ~ 50 eV is used.

The barium pseudopotential is also generated from the BHS electron configurations. This time there is a separate configuration for each angular momentum quantum number. Once again the ground state ($6s^2$) is used for the $l = 0$ component. This time the $l = 1$ component is generated from the configuration $6s^{0.75}$ $6p^{0.25}$ and $6s^{0.75}$ $6d^{0.25}$ is used for the $l = 2$ component. The core radii resulting from these are 3.94 a.u. for the $l = 0$ term, 4.59 a.u. for the $l = 1$ term and 7.57 a.u. for the $l = 2$ term. The value used for r_0 is 3.40 a.u. The three terms of this pseudopotential are shown in figure 5.20. As might be expected it has many of the same features apparent in the other core corrected pseudopotentials. All components of the potential are soft core in nature and the $l = 0$ and $l = 1$ terms converge rapidly onto the bare ion curve around their respective core radii. As in the other cases the magnitude of the $l = 2$ core radius prevents this convergence from occurring within the range shown in figure 5.20. The $l = 0$ wave functions

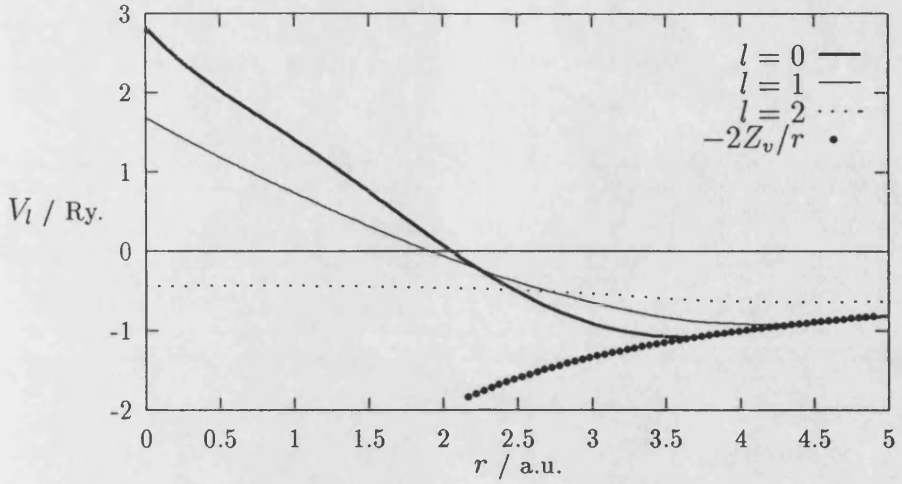

Figure 5.20: Ba pseudopotential with core corrections.

are once more the last to achieve energy convergence as the cut-off energy is increased. In this case examination of the wave functions reveals that an energy cut-off of ~ 80 eV is required to bring it to within 1 meV of full convergence.

In all cases the core density utilised is that generated by the electronic configuration of the $l = 0$ component of the pseudopotential. In the potentials initially used this is also the ground state configuration of the metal atom. Later, pseudopotentials with cores will be generated for which this is not the case. Calculations are made with each of the metal pseudopotentials in a large irregular box. As in chapter 3 when similar calculations were made for magnesium, the intention is to find out how well the CETEP code can reproduce the core charge density. Figure 5.21 shows the results of this in the case of calcium. The curve denoted AT is the data obtained from the atomic calculation while the points represent data outputted from the CETEP program. It can be clearly seen that the pseudo-core charge density is correctly reconstructed. When compared with the magnesium core (figure 3.27) the two are superficially very similar. The calcium core is,

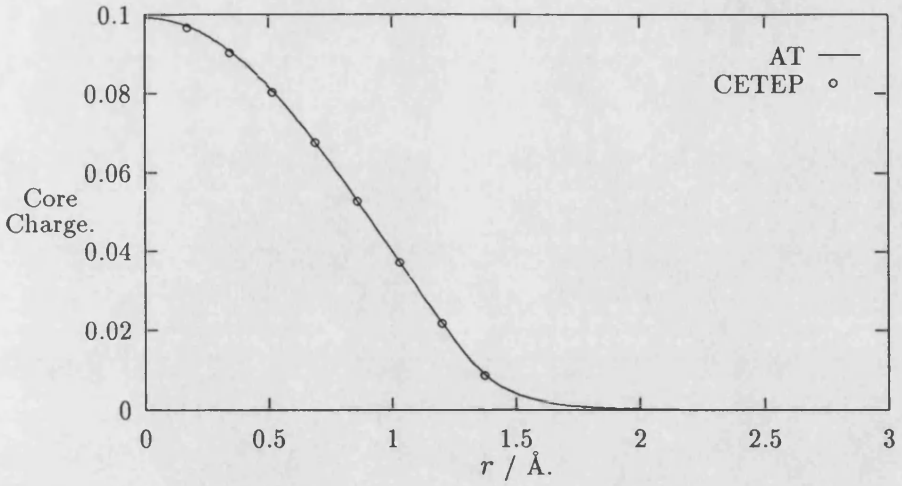

Figure 5.21: Pseudo-core density for Ca.

however, only about half the magnitude at the origin and becomes negligible at around 1.5 Å rather than 1.0 Å seen with Mg. This greater width gives an increased probability of an interaction between the core and valence charge densities. This might then result in predictions of the physical properties of CaO that are different to those calculated using non core corrected pseudopotentials.

This calculation is repeated for an isolated strontium atom in an identically sized box. The core charge density is extracted from CETEP and displayed in figure 5.22. The results of a corresponding atomic calculation (denoted AT) are also shown on this figure. Once again agreement between the two is very good demonstrating the correct reconstruction of the core charge by the CETEP program. The expected trend in shape continues with the strontium core charge density having a somewhat greater width than that possessed by calcium earlier.

Figure 5.23 shows the core charge density from a barium pseudopotential. It is calculated in the same way as before and the acronyms used are the same as those

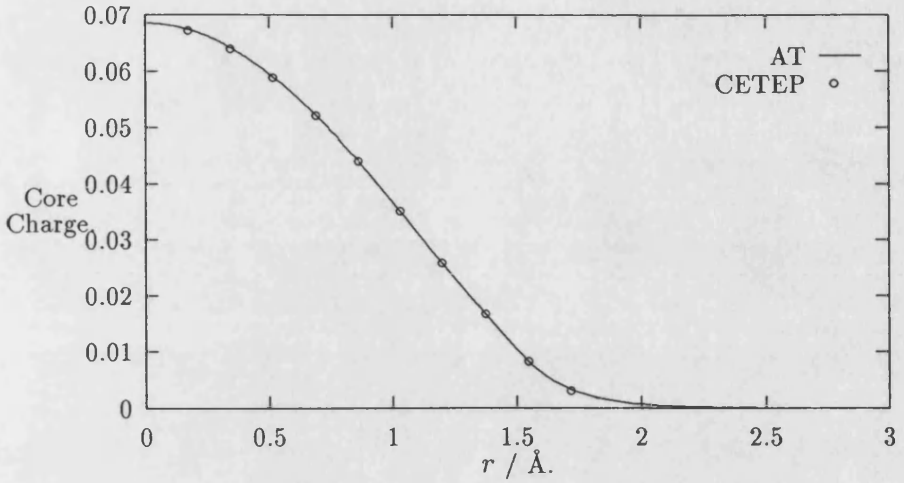

Figure 5.22: Pseudo-core density for Sr.

above. The agreement between the atomic calculations and the reconstructed CETEP values is good. Once again the charge density extends slightly further away from the atom site than for the other earth-metals.

Calculations are now made using these core corrected pseudopotentials to establish the lattice parameters and bulk moduli. With the exception of using the core charge density in the evaluation of the exchange and correlation part of the energy, this is achieved in exactly the same manner as before. All the parameters needed to set-up the problem for solution (cut-off energy, k-space box, special k-points etc.) remain unchanged. As in the previous case the increased size of the barium oxide lattice required that the k-space box be increased from $(32)^3$ to $(36)^3$. The small changes to the CETEP codes necessary to implement non-linear core corrections do not result in any measurable increase in the time required for computation and twelve to fifteen iterations is generally still sufficient to converge the energy. A four special k-point calculation still requires between twenty and thirty minutes (depending on the number of plane wave coefficients

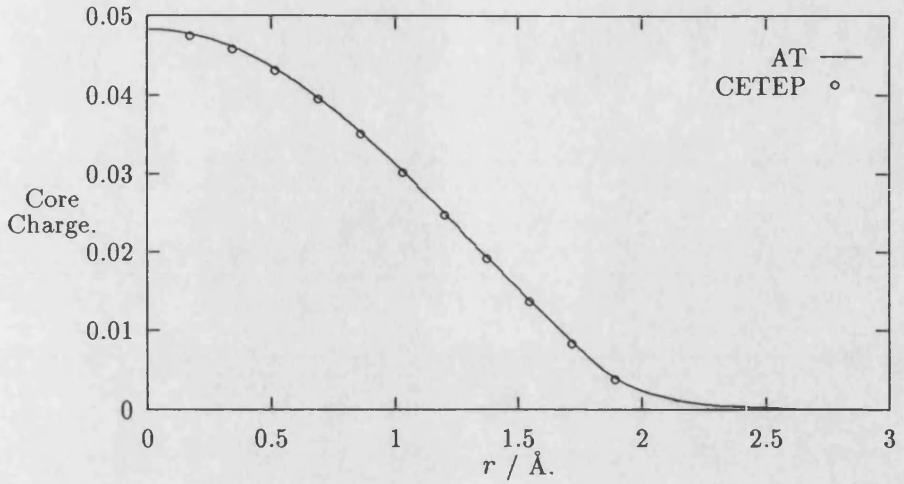

Figure 5.23: Pseudo-core density for Ba.

used) to achieve convergence. The results for calcium oxide are shown in figure 5.24 and the evaluated lattice parameters and bulk moduli for all three oxides are summarised in table 5.10. The acronym CC refers to results calculated using pseudopotentials that have had non-linear core corrections applied, similarly NC refers to the previously obtained results for which the corrections were not applied.

The physical parameters extracted from this data are shown in table 5.10 along with the results for SrO and BaO. The same pattern is followed by all three oxides. The lattice parameters are larger than the experimental values. In CaO this is by a margin of 11%, in SrO it is by 13% and by 16% in BaO. These are all much greater than the discrepancies found previously before the application of core corrections. The increase in the percentage difference as the metal ion increases in size could be an indication of the relative influence of the core corrections. With its large core charge density it is not surprising that the greatest effect is experienced in barium oxide. With the lattice parameters becoming increasingly

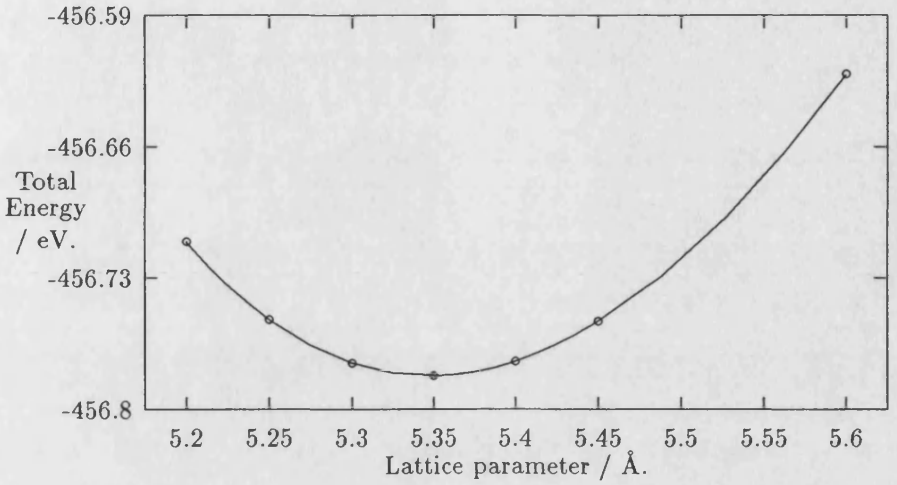

Figure 5.24: Total energy versus lattice parameter for core corrected CaO.

larger than the experimental value there is a corresponding decrease in the bulk modulus. The prediction for CaO is $\sim 30\%$ too small, that for SrO is $\sim 31\%$ too small and $\sim 40\%$ too small for BaO.

The fact that there are (quite large) differences between the physical parameters predicted with and with core corrections is justification in itself for their use. It is unfortunate that the effect of this adjustment has been to take the results further away from experiment than before. It has been observed before (see for example Qteish and Needs, 1991, or Farid and Needs, 1992) that the application of these corrections tends to increase that value of the predicted lattice parameter. The results here merely reinforce this view.

A set of calculations is made for MgO with non-linear core corrections included. The magnesium pseudopotential used in this is the one shown in figure 3.26 earlier. The results of this are also shown in table 5.10. The lattice parameter resulting from this is found to be 4.32 Å which is $\sim 2.6\%$ too large and the

		a_0/Å			B/GPa		
		expt.	calc.	error	expt.	calc.	error
MgO	NC	4.21	4.23	+0.5%	160	163	+1.9%
	CC		4.32	+2.6%		155	-3.1%
CaO	NC	4.81	5.08	+5.6%	115	109	-5.2%
	CC		5.35	+11.2%		81	-29.6%
SrO	NC	5.16	5.36	+3.8%	87	66	-9.2%
	CC		5.81	+12.6%		60	-31.0%
BaO	NC	5.54	5.80	+4.7%	70	69	-1.4%
	CC		6.43	+16.1%		42	-40.0%

Table 5.10: Lattice parameters and bulk moduli from core corrected potentials.

bulk modulus is 155 GPa, $\sim$ 3.1% too small. Although these figures show the same pattern exhibited by the other calculations in this section (a_0 increasing as B decreases), the differences are on a much smaller scale. There must be very little overlap between the magnesium core charge density and the valence charge density in MgO so the corrections do not significantly affect the predictions made for the physical properties of MgO.

5.6.2 Core corrections from ionised configurations

Non-linear core corrections are now applied to the ionised pseudopotentials that provided such a wide range of results in section 5.5 above. When these adjustments were made to the uncorrected metal pseudopotentials the result was to reduce the predicted value of the lattice parameter in all cases. This demonstrated the lack of transferability in the potentials. To investigate the effect of core-corrections on these ionised pseudopotentials two different calcium potentials are generated from electron configurations used above.

A pseudopotential is formulated with the $l = 0$ component taken from the configu-

	a_0/Å			B/GPa		
	expt.	calc.	error	expt.	calc.	error
BHS	4.81	5.35	+11.2%	115	81	-29.6%
s ionised		5.34	+11.0%		84	-27.0%
s,p,d ionised		5.32	+10.6%		82	-28.7%

Table 5.11: Lattice parameters and bulk moduli of CaO from ionised core corrected potentials.

ration $4s^{0.5}$, and the $l = 1, 2$ components generated from the (BHS) configuration $4s^{0.5}\ 4p^{0.25}\ 4d^{0.25}$. The core radii for this potential are 2.87 a.u. for the s term, 3.51 a.u. for the p term and 6.08 a.u. for the d term. These values are the same as for the uncorrected potential. The cut-off radius for the core charge density r_0 is set at 2.35 a.u. This is slightly smaller than that of the un-ionised potential.

In the previous calculation in section 5.5.1 above the results obtained for the lattice parameter and bulk modulus of CaO were very close indeed to the experimental values. A similar set of calculations using the core corrected version of this potential is now made with all other parts of the set-up remaining the same as before. The results of this are summarised in table 5.11 along with the experimental values and those derived from the full BHS configuration. It can be seen from this that the lattice parameter is 5.34 Å and the bulk modulus is 84 GPa. These figures are very different to the uncorrected results that were shown earlier in table 5.6. They are, however, very close to those obtained for the original core corrected pseudopotential.

A core corrected pseudopotential is also generated from the almost entirely ionised configuration used in section 5.5.3. All three components are derived from the same electronic configuration $4s^{0.1}\ 4p^{0.1}\ 4d^{0.1}$. The core radii for this potential are 2.78 a.u. for the $l = 0$ term, 3.51 a.u. for the $l = 1$ term and 5.23 a.u. for the $l = 2$ term. These are, once again, the same radii as for the uncorrected

		a_0/Å			B/GPa		
		expt.	calc.	error	expt.	calc.	error
SrO	BHS	5.16	5.81	+12.6%	87	60	-31.0%
	s,p,d ionised		5.77	+11.8%		62	-28.7%
BaO	BHS	5.54	6.43	+16.1%	70	42	-40.0%
	s,p,d ionised		6.39	+15.3%		42	-40.0%

Table 5.12: Lattice parameters and bulk moduli of SrO and BaO from ionised core corrected potentials.

potential. The value of r_0 is set to 2.53 a.u.

The usual calculations are now made to establish the lattice parameter and bulk modulus of calcium oxide. Once again the results of this are summarised in table 5.11. The lattice parameter calculated from this data is found to be 5.32 Å and the bulk modulus to be 82 GPa. Once again these results are much changed from those obtained by using the uncorrected potential shown earlier in table 5.9. They are also very close to the results obtained for CaO when using the other core corrected pseudopotentials.

The use of non-linear core corrections has introduced a welcome measure of consistency to the predictions made for the properties of CaO. It appears that this use has essentially restored the transferability of the calcium pseudopotentials. Calculations are now made to discover whether this effect is repeated when core corrections are applied to ionised strontium and barium pseudopotentials. Potentials are generated in the usual manner for both strontium and barium from highly ionised configurations. The strontium pseudopotential uses a configuration of $5s^{0.1}\ 5p^{0.1}\ 5d^{0.1}$ and the barium potential is generated from a configuration of $6s^{0.1}\ 6p^{0.1}\ 6d^{0.1}$. Sets of calculations are made with these potentials to predict the lattice parameter and bulk modulus of SrO and BaO. The results of this are summarised in table 5.12 along with the previous values obtained by core correct-

ing potentials generated from the BHS configurations. As can be seen from table 5.12 there is, once more, a remarkable similarity between the values predicted by the two different potentials. Although the results are not very close to the experimental values it is obvious that as with CaO the use of non-linear core corrections seems to have returned the transferability to the metal pseudopotential.

Given the generally poor agreement with experiment there is not much point in calculating separate elastic constants. This is unfortunate as this was one of the aims of this chapter.

5.6.3 Other ways of simulating the core

It is interesting to attempt to simulate the influence that a large core has on the properties of an ion without resorting to non-linear core corrections. For example, by treating the six electrons in the closed $3p$ orbital as valence electrons rather than as part of the core the large charge density close to the atom site will (hopefully) be simulated directly. Obviously the effect of only part of the core is treated here. A calcium pseudopotential is generated using the electronic configuration $3p^6\ 4s^2$ for the $l = 0$ and $l = 1$ components while the configuration $3p^6\ 4s^{0.5}\ 4d^{0.25}$ is used for the $l = 2$ component. The core radii resulting from this are 3.02 a.u. for the $l = 0$ term, 1.00 a.u. for the $l = 1$ term and 5.78 a.u. for the $l = 2$ term. This potential is shown in figure 5.25.

The most striking feature of the new potential is the hardness of the terms close to the origin. This is most evident in the $l = 1$ component which must converge with the bare ion potential very quickly indeed. As the six $3p$ electrons are now moved from core to valence the valence charge of the ion, Z_v, is now eight and

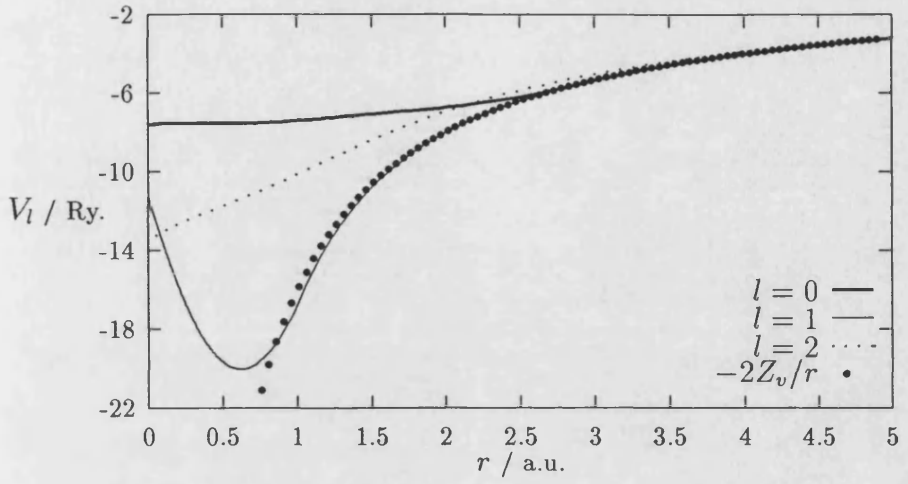

Figure 5.25: Ca pseudopotential with core p states included.

the bare ion potential becomes $-16/r$ when the energy is measured in Rydbergs. Examination of the wave functions reveals that it is now the $l = 1$ component of the potential that requires the largest energy cut-off to achieve convergence. In this case a cut-off of ~ 650 eV is needed for this.

Calculations are carried out to discover the lattice parameter and bulk modulus of CaO using this pseudopotential. As the new calcium potential has eight rather than two electrons the number of bands in the calculation is increased from four to seven. With all other parts of the set-up remaining constant this leads to an increase in the run time of the CETEP program to about forty minutes if four special k-points are used. The results of this are shown in figure 5.26. The lattice parameter is calculated to be 5.55 Å which is $\sim 15\%$ too large (compared with the core corrected value that was $\sim 11\%$ too large). The bulk modulus at this point is 74 GPa which is $\sim 35\%$ too small. In this case the previous core corrected result was $\sim 30\%$ too small. The inclusion of p core electrons in the calcium pseudopotential has had an effect similar to the use of non-linear core

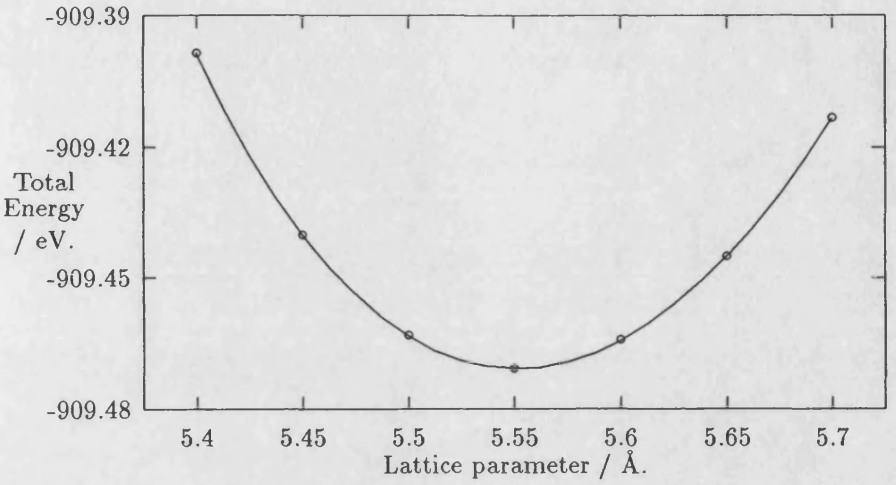

Figure 5.26: Total energy versus lattice parameter for CaO with core p states.

corrections. In both cases the lattice parameter is increased at the expense of reducing the bulk modulus. The only difference is in the magnitude of the effect.

5.7 Charge Density Calculations

In chapter 4 a greater understanding of the physical properties of MgO was obtained by examining charge density patterns at equilibrium and under a variety of different strains. Qualitative information was acquired by comparing the charge densities in real space of cubic and tetragonally strained MgO. This led us to suspect that the breathing of the electron cloud around the oxygen ion sites might be the mechanism causing the violation of the Cauchy condition. Evidence for this of a more quantitative nature was then gained through studying the charge density in reciprocal space. The magnitude (and sign in BaO) of the Cauchy violation has been shown experimentally to vary amongst the different earth-metal

oxides. It is possible that the charge density patterns of CaO, SrO and BaO could yield similar information about their bonding and elastic properties. The results of these calculations are interesting to look at, but it will probably be difficult to make definitive conclusions because of the work mentioned previously.

The pseudo-charge densities are extracted from the CETEP code in the same way as previously done for MgO. The contributions from the individual nodes are collected and sorted into the correct order. This data from the primitive cell (with only a single metal and oxygen ion) is then transferred to a full fcc cell. This can then be sliced and displayed as desired. As with the MgO patterns shown in chapter 4 it is necessary to make the calculations with the full 16 special k-point set so that the results are properly converged with respect to this.

Figure 5.27 shows the pseudo-charge density in the [100] plane of CaO. The oxygen ions are to be found in the centre and at the corners of the figure. The calcium ions are half way along each edge. There is a minimum over each of the calcium ion sites as it is a pseudo-charge density. The scale used is electrons (times $(32)^3$, the size of the mesh used) per Angstrom^3. This is calculated for an unstrained cubic lattice with the lattice parameter a_0 set to its *experimental* value of 4.81 Å although core corrections are applied. The contours reveal that the electronic structure of CaO is similar to that of MgO shown earlier in figure 4.11. As expected the charge density close to an oxygen ion site is perfectly spherical.

A volume conserving tetragonal strain is now placed on a CaO crystal. The pseudo-charge density pattern resulting from this is shown in figure 5.28. The scale used is identical to that of figure 5.27 above and the two can be compared directly. There is now a marked distortion of the contours encircling the oxygen

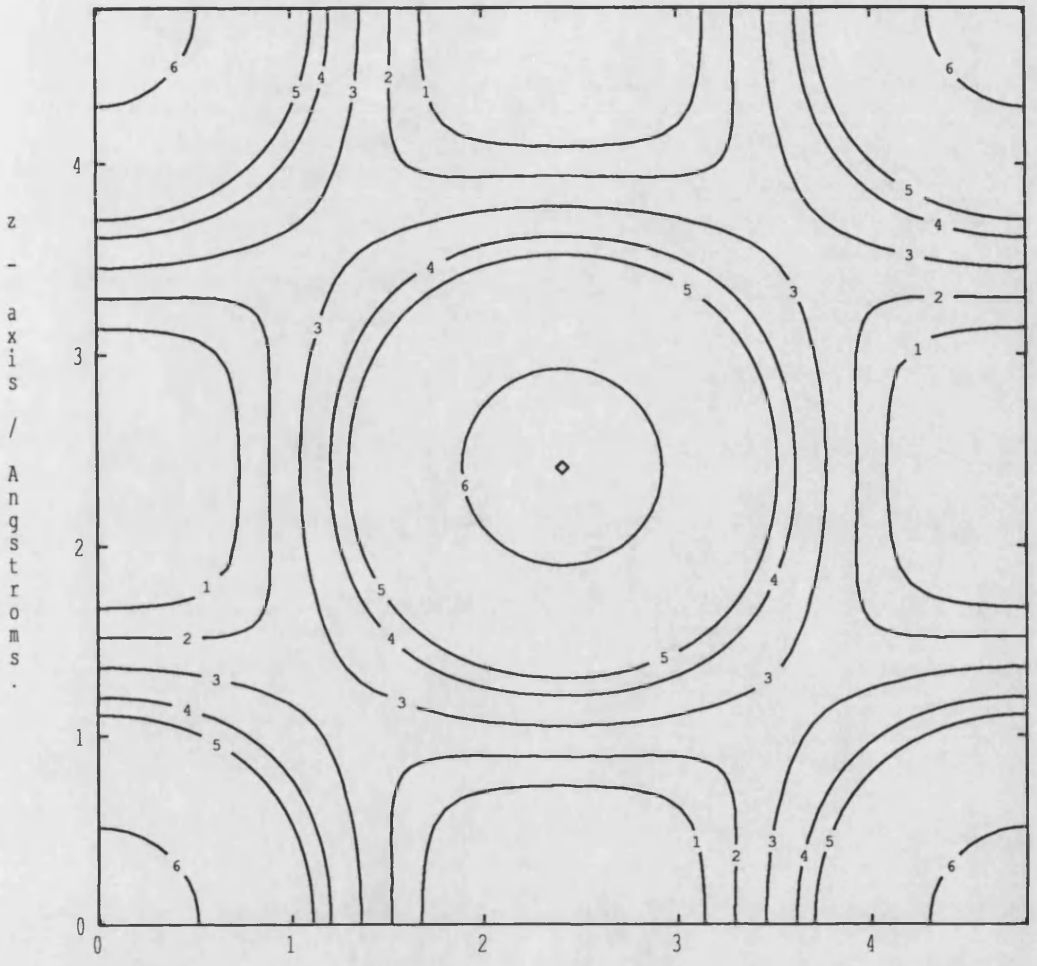

CONTOUR KEY	
1	0.5000E+00
2	0.1000E+01
3	0.2000E+01
4	0.4000E+01
5	0.6000E+01
6	0.8000E+02

Figure 5.27: Charge density of CaO at experimental equilibrium.

ion sites. This is in stark contrast to the behaviour observed earlier for MgO and shown in figure 4.12. On this occasion the charge surrounding the oxygen ions was found to remain circular even though the crystal as a whole was heavily distorted. Although there is this distortion observed in the contours it is not of the same magnitude as the distortion on the unit cell. The contours also become increasingly circular as they close in around the oxygen ion site. Indeed the contour numbered six (which is of a very much higher electron density) is circular and the charge cloud at around here is perfectly spherical.

When the data displayed in figures 5.27 and 5.28 is Fourier transformed the charge density in reciprocal space is obtained. The first few points of this are shown in figure 5.29. As might be expected this figure has many similarities with that of MgO in figure 4.13 earlier. The points obtained from the cubic crystal lie on a smooth curve and the points derived from the tetragonal strain are (in some cases) split to either side of the equivalent cubic point. These tetragonal points also lie on, or very near to, the curve described by the cubic data. This confirms that although the charge density is not breathing as perfectly as the MgO density did, it is still not distorting to anything like the extent that the cell does.

The real space pseudo-charge density of SrO is shown in figure 5.30. As before this is for an unstrained cubic crystal with the lattice parameter set to the experimental value of 5.16 Å. The computational set-up is the same as that used for CaO above and an identical [100] plane is displayed. The same features can be discerned in figure 5.30 that were seen in figures 5.27 and 4.11. The electron cloud is spherical around the oxygen ion sites and there is a minimum over each of the strontium ion sites.

As above a volume conserving tetragonal strain is placed upon the crystal at this

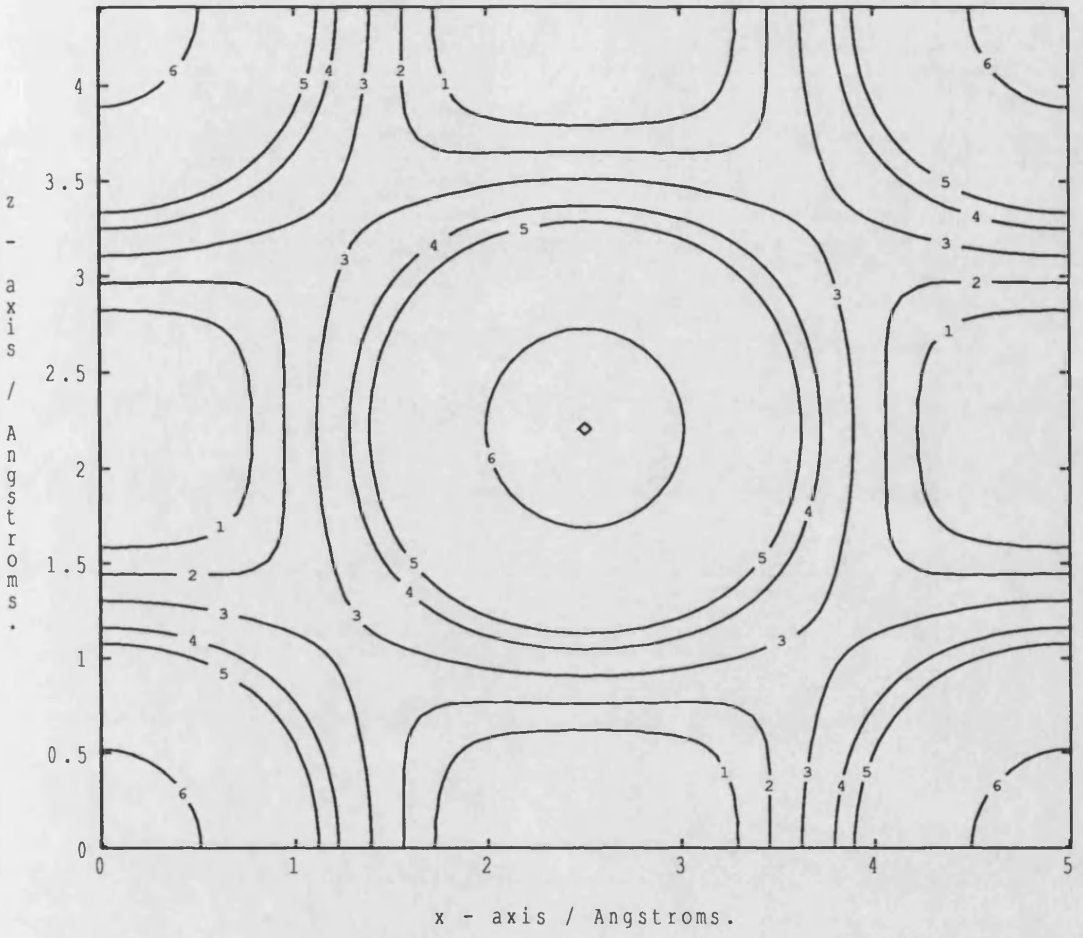

CONTOUR KEY	
1	0.5000E+00
2	0.1000E+01
3	0.2000E+01
4	0.4000E+01
5	0.6000E+01
6	0.8000E+02

Figure 5.28: Charge density of CaO with tetragonal strain applied.

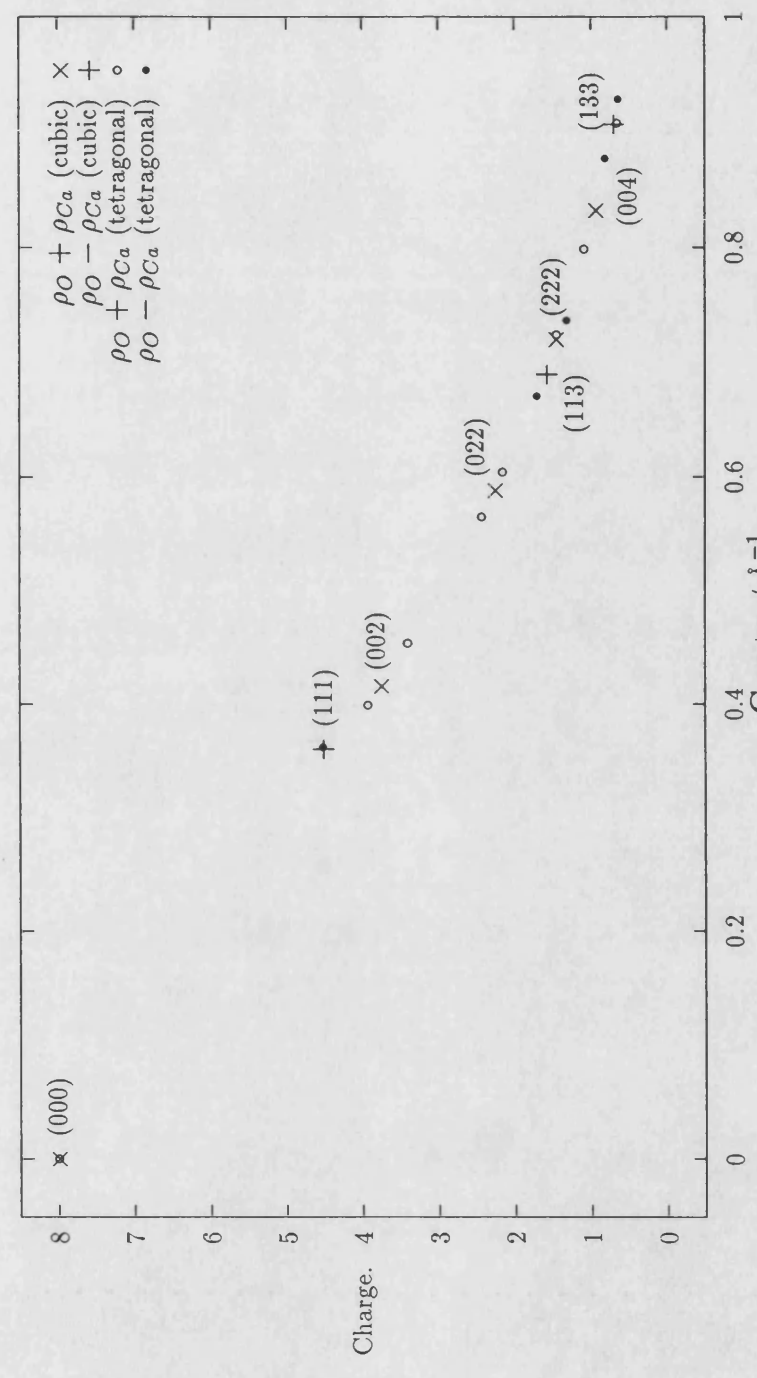

Figure 5.29: Charge density in **G**-space for CaO strained about equilibrium.

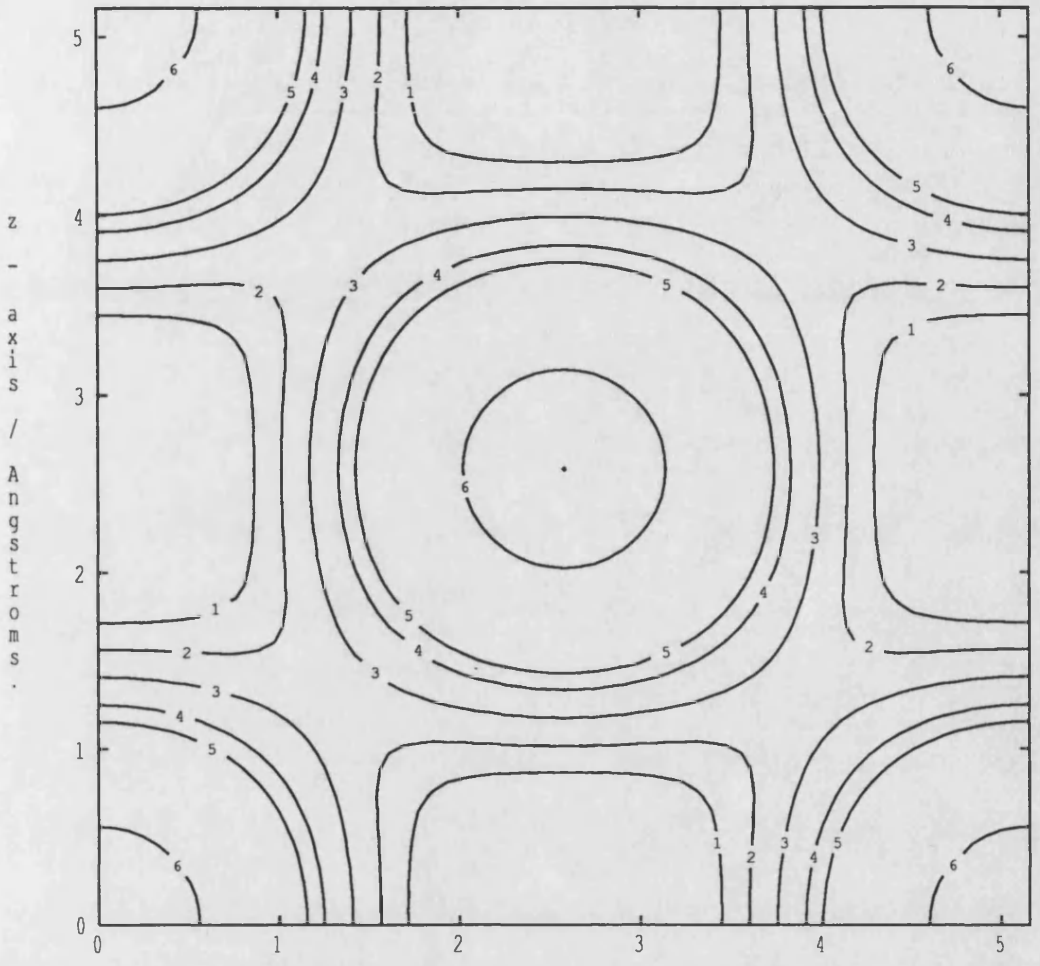

CONTOUR KEY	
1	0.5000E+00
2	0.1000E+01
3	0.2000E+01
4	0.4000E+01
5	0.6000E+01
6	0.8000E+02

Figure 5.30: Charge density of SrO at experimental equilibrium.

point. The resulting pseudo-charge density is shown in figure 5.31. Once again it is observed that the charge around the oxygen ions distorts in much the same way as it did in CaO above. As before the charge cloud eventually becomes spherical when it is close to the oxygen ion sites.

When the data from the two previous figures are Fourier transformed they yield the reciprocal space charge distribution shown in figure 5.32. As might be expected the data points derived from the cubic charge density calculation all lie on the smooth same curve. If the data points from the tetragonal strain are examined closely, however, it is possible to see that the splitting of the data points is such to move them perceptively away from the curve described by the cubic data. When the analysis from section 4.6 is applied is becomes obvious that the breathing shell model has broken down and the charge density is now distorting in the same sense as the crystal. This effect is still very small and, indeed, it is only the outermost parts of the charge cloud that behave in this way. The innermost part of the valence charge density is unaffected and remains spherical.

The real space pseudo-charge density of BaO is shown in figure 5.33. As before this is for an unstrained cubic crystal with the lattice parameter set to the experimental value of 5.54 Å. The computational set-up is the same as that used before and an identical [100] plane is displayed. Once again the same features can be discerned in figure 5.33 that were observed earlier. The electron cloud is again spherical around the oxygen ion sites and there is a minimum over each of the barium ion sites.

As before a volume conserving tetragonal strain is placed upon the crystal at this point. The resulting pseudo-charge density is shown in figure 5.34. Once again it

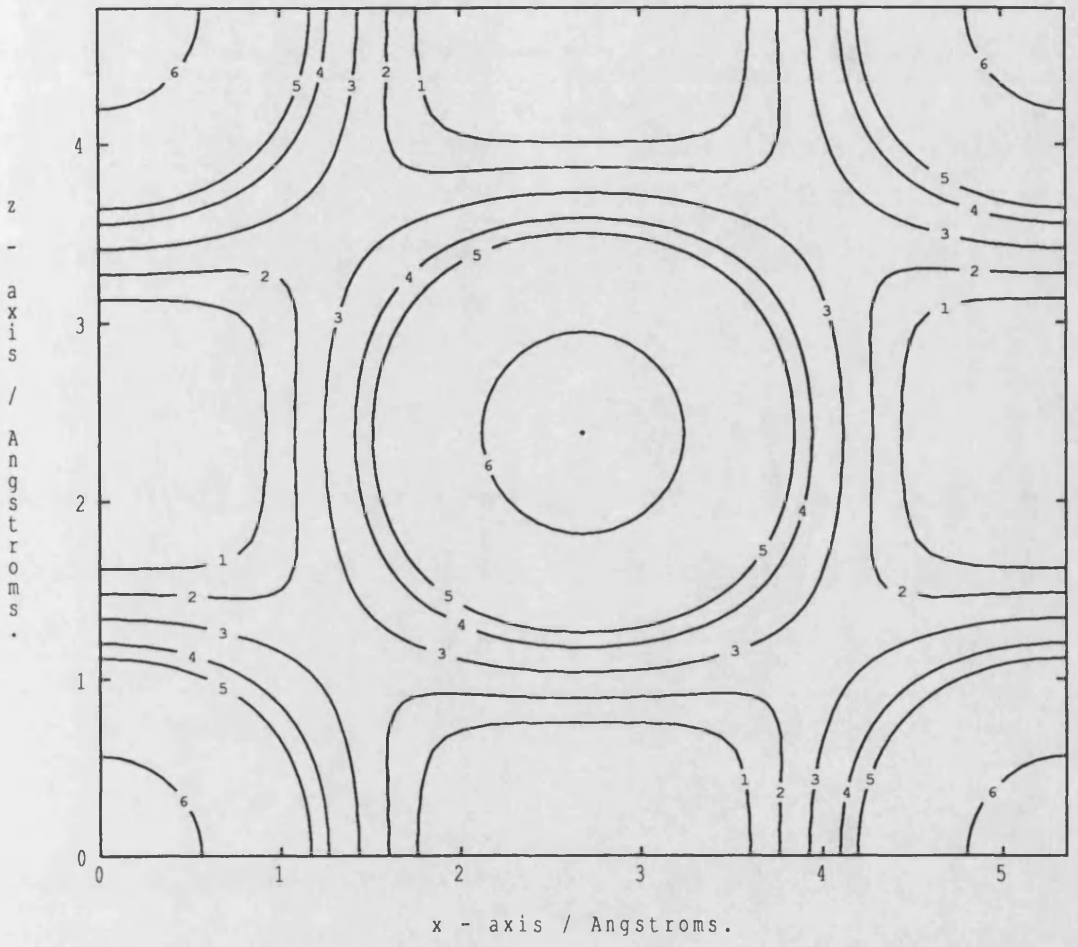

CONTOUR KEY	
1	0.5000E+00
2	0.1000E+01
3	0.2000E+01
4	0.4000E+01
5	0.6000E+01
6	0.8000E+02

Figure 5.31: Charge density of SrO with tetragonal strain applied.

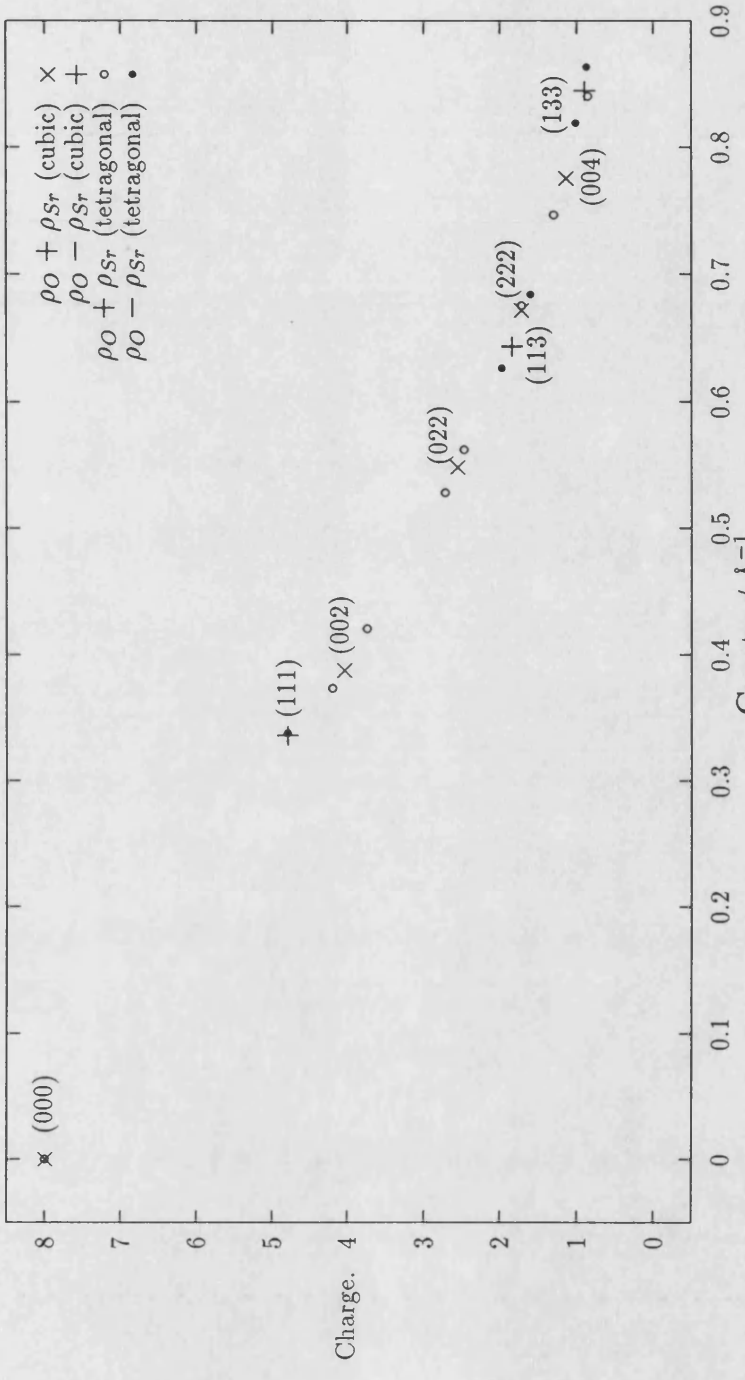

Figure 5.32: Charge density in **G**-space for SrO strained about equilibrium.

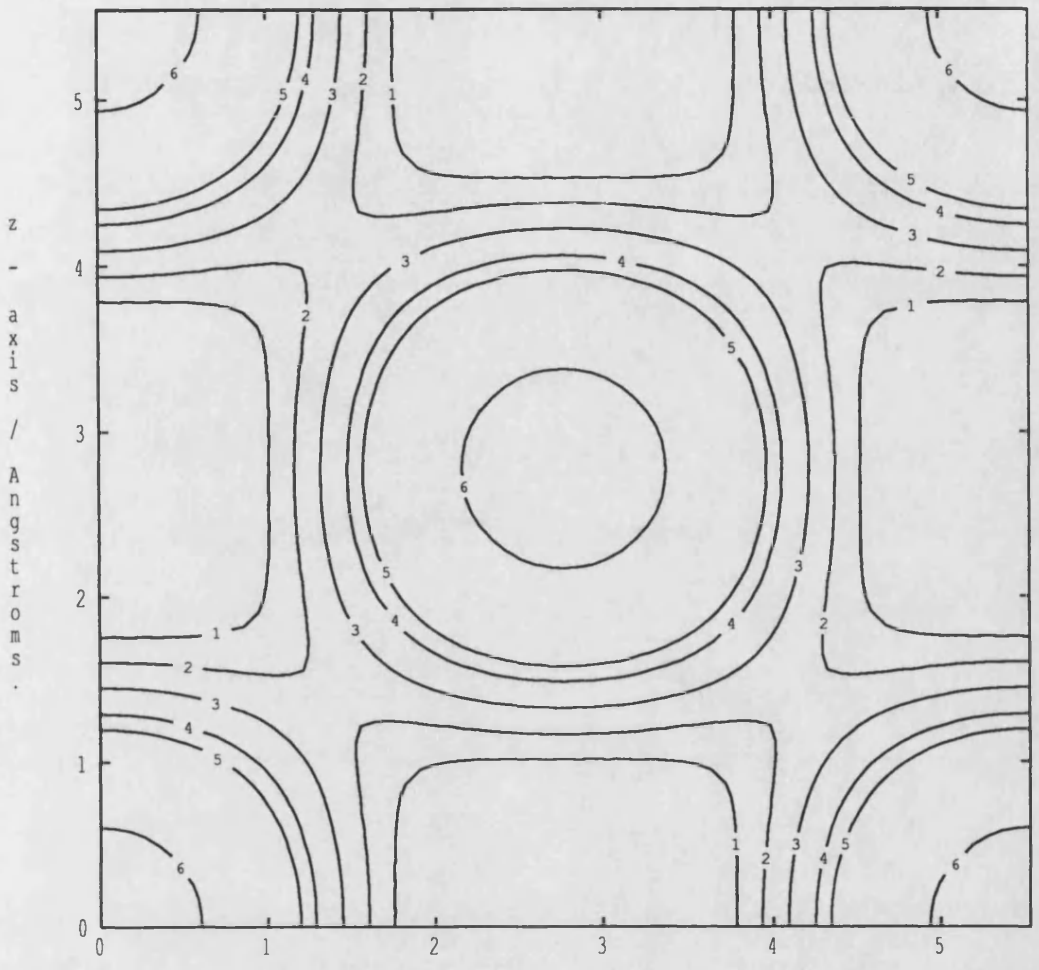

CONTOUR KEY	
1	0.5000E+00
2	0.1000E+01
3	0.2000E+01
4	0.4000E+01
5	0.6000E+01
6	0.8000E+02

Figure 5.33: Charge density of BaO at experimental equilibrium.

is observed that the charge around the oxygen ions distorts in much the same way as it did in CaO and SrO above. Once again the charge cloud eventually becomes spherical when it is close to the oxygen ion sites. If the ellipticity of the contours of figure 5.34 are measured there is evidence that the distortion is greater in this case than in the previous case of SrO. The ratio of the long diameter to the short diameter of, say, the contour labelled 4 is 1.075:1. This can be compared to the equivalent values for SrO (which is 1.070:1) and CaO (which is 1.065:1). In comparison the ratio of the sides of the unit cell vary between 1.136:1 in CaO and 1.116:1 in BaO. These differences are small but measurable if care is taken. In all cases the distortion of the oxygen charge cloud is less than that of the cell as a whole indicating that only a small amount of the outer charge cloud is being affected.

When the data from the two previous figures are Fourier transformed they yield the reciprocal space charge distribution shown in figure 5.35. As in previous the data points derived from the cubic charge density calculation all lie on the smooth same curve. This time it does not require such a close examination of the data points from the tetragonal to establish that there is a split occurs from the curve of the cubic data. This split is particularly easy to observe around the (002) data points. The effect here is much larger than the similar effect in SrO.

It should be noted that although the strains imposed on the lattices are of the same magnitude because of the differences in lattice parameter between the oxides the relative size of the strains are actually different. The distortion used in these calculations was a tetragonal one with $\epsilon = (\eta, \eta, -2\eta, 0, 0, 0)$. In all cases the length of two lattice vectors are changed by 0.2 Å while the third is altered by 0.4 Å in the opposite direction. The leads to a value of $\eta = 0.036$ in BaO, this increases to $\eta = 0.039$ in SrO, $\eta = 0.042$ in CaO and finally it was $\eta = 0.047$

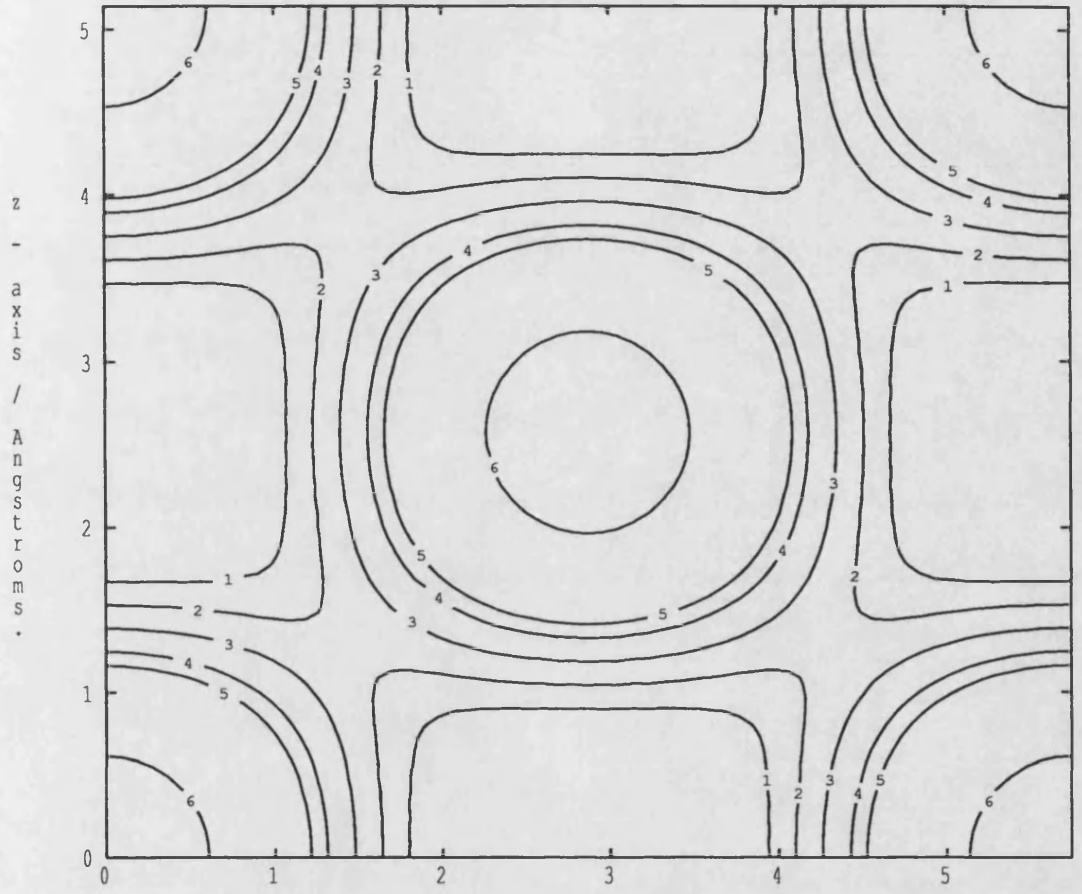

CONTOUR KEY	
1	0.5000E+00
2	0.1000E+01
3	0.2000E+01
4	0.4000E+01
5	0.6000E+01
6	0.8000E+02

Figure 5.34: Charge density of BaO with tetragonal strain applied.

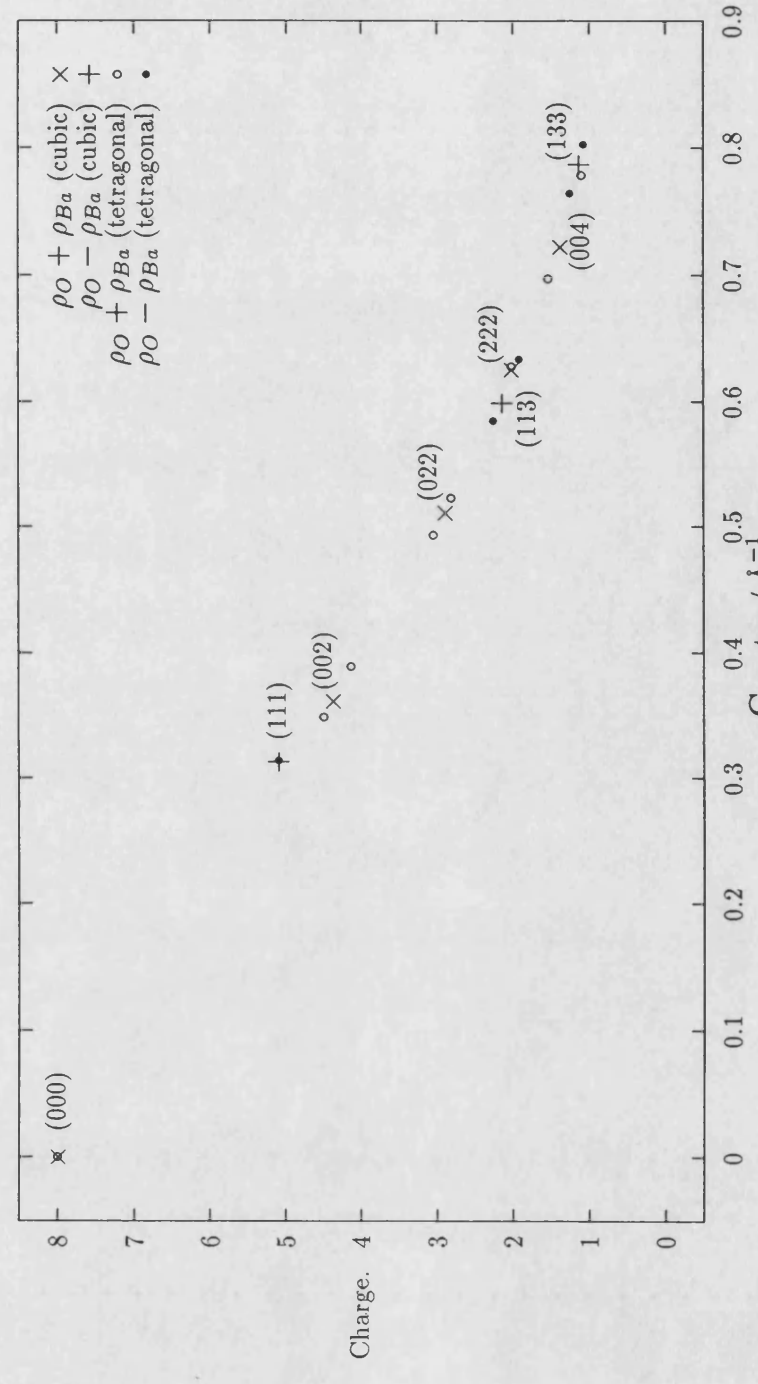

Figure 5.35: Charge density in **G**-space for BaO strained about equilibrium.

for the MgO calculations in chapter 4. Although the reciprocal space splitting of the tetragonal charge density points in BaO is only a small effect it is still easily larger than that observed for SrO. This occurs for a distortion of the unit cell that is rather smaller than that used for SrO.

5.8 Discussion

The calculations made in this chapter of the equilibrium properties of the earth-metal oxides have been different in character to those obtained for similar properties of MgO in chapter 4. Although the predictions made by the HSC type pseudopotentials and those generated by the Kerker method are consistent with each other they are not as close to the experimental values as those made for MgO. This is obviously disappointing, although attention should be drawn to the scarcity of good experimental data with which to compare these results. Certainly the previous calculations made using different techniques have been little better in this regard. It was suspected that the cause of this loss of accuracy might be due to poor transferability of the metal pseudopotentials (especially when compared to that of the magnesium potential). This was confirmed by the calculations performed with ionised pseudopotentials. These showed that by altering the electronic configuration used to generate the potentials it was possible to obtain almost any value for physical properties such as the lattice parameter or bulk modulus of the oxide.

To remedy this failing of both the HSC and the Kerker pseudopotentials non-linear core corrections were applied during the formulation of the potentials. This had the desired effect of restoring the transferability of the pseudopotentials. Irrespective of the initial electronic configuration the core corrected pseudopotential

always yields essentially the same predictions for the physical parameters of the earth-metal oxides. There is still a problem here as the predictions made for these physical parameters are every bit as poor as those made earlier without the corrections. It is, however, likely that the values obtained by this technique can in many ways be regarded as the true LDA results.

The differences between these results and those obtained experimentally must be caused by interactions beyond the capacity of LDA to simulate. One example, which is included in empirical models, arises from fluctuations in the dipole moment of large ions, giving rise to the Van der Waals attraction in solids. As this is obviously time dependent it makes no contribution to the LDA predictions. The dipole-dipole interaction is usually simulated (see for example Fowler *et al*, 1985 or Pyper, 1986) by an adjustment to the total energy of the form,

$$\Delta E \sim -S_6 \frac{C_6}{r^6}, \tag{5.1}$$

where r is the distance between the two dipoles, C_6 is the dispersion coefficient for the two dipoles and S_6 is the lattice dispersion sum constant. The value of S_6 is given by Pyper (1986) to be 6.5952 for all lattices of the rock salt structure. It is a purely geometrical factor obtained by direct summation in real space of all the r^{-6} terms in the lattice. The C_6 for two species a and b are obtained from the approximation of Slater and Kirkwood (1931),

$$C_6(a,b) \sim \frac{3\alpha_a\alpha_b}{2[(\alpha_a/P_a)^{\frac{1}{2}} + (\alpha_b/P_b)^{\frac{1}{2}}]}, \tag{5.2}$$

where P_a is the electron number (equals two for the earth-metals) of species a and α_a is the static dipole polarizability of species a. These polarizabilities can be extracted from sources such as Phillips and Williams (1965). The energy change derived from equation (5.1) neglects contributions from dipole-quadrupole interactions (which are proportional to r^{-8}) and damping terms. These effects will are small and are ignored in these calculations.

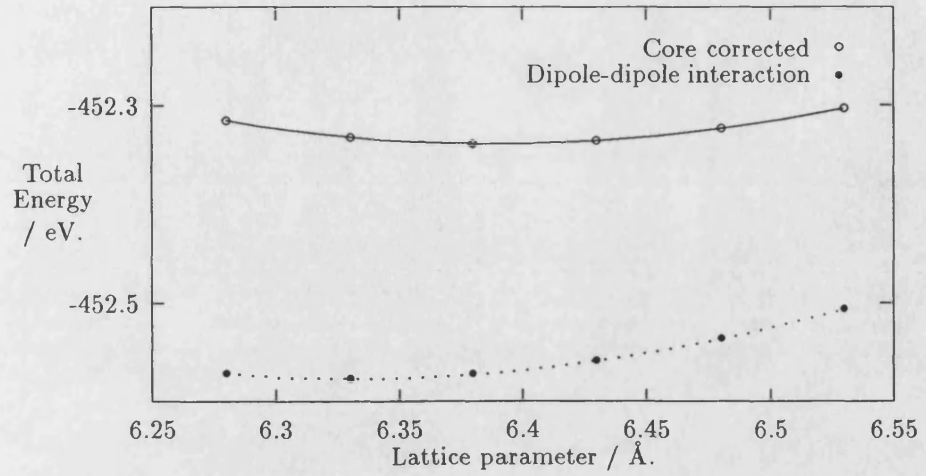

Figure 5.36: Total energy versus lattice parameter for BaO before and after the addition of the Van der Waals correction.

When the energies calculated from equation (5.1) are added to those calculated by the CETEP codes the effect is as expected. In all cases the lattice parameter is decreased with a corresponding increase in the bulk modulus. This is illustrated for BaO in figure 5.36. The curve described by the data points obtained by applying the Van der Waals correction are around one quarter of an electron volt more negative than those previously obtained in the (core corrected) CETEP calculation. The minimum has perceptively moved to a smaller value of the lattice parameter.

In the case of MgO the lattice parameter falls to 4.26 Å (from 4.32 Å, the core corrected result). This is very close to the experimental value of 4.21 Å. The lattice parameter decreases by larger amounts in the other oxides. In CaO there is a drop of 0.08 Å in the value of a_0 to 5.25 Å (compared to the experimental value of 4.81 Å). SrO has a drop of 0.10 Å to make a_0 become 5.71 Å (compared with 5.16 Å in experiment) and in BaO the increase in the dipole-dipole interaction brings the lattice parameter down by 0.11 Å to 6.32 Å (compared to 5.54 Å in

experiment). In none of these cases is the reduction in the lattice parameter enough to bring the prediction close to the experimental value. Although this effect is small, it is by no means negligible, and presumably it must form a part of the solution to this problem. However, either the above analysis has been simplified too much, or other (possibly more important) interactions are at work.

The disagreement between our LDA calculations and experiment is the main result of this chapter. As the predictions for the values of the lattice parameter and bulk modulus are so wrong there was little point calculating the individual elastic constants. It was impossible, therefore, to properly address the original problem of the mechanism behind the change in the Cauchy violation from MgO to BaO. However, the charge density plots are interesting and might well point to part of the explanation. Examination of the charge density patterns (in real and reciprocal space) has yielded much information about the nature of the earth-metal oxides. The increasingly visible splitting of the tetragonally strained points in reciprocal space is reflected by the distortion of the oxygen charge cloud in real space. It is this predilection of the charge cloud to distort as well as breathe in the oxides of the largest earth-metals which could provide a mechanism for the lessening of the Cauchy violation in these materials.

Chapter 6

CONCLUSION

The purpose of this thesis was to calculate from first principles the physical properties of earth-metal oxides. There were broadly three strands of this work with which we were interested.

The CETEP codes needed to be tested on as many different materials as possible. The comparison made in chapter 4 between the physical properties of MgO predicted by the CETEP codes and those obtained previously by other methods shows that the advantage in accuracy has been maintained. The values predicted are easily the closest to experiment obtained so far. Not only are the basic results for lattice parameter and bulk modulus well within the range of accuracy expected in LDA calculations, but the predictions for the individual elastic constants are also to be found within an acceptable range of the experimental values. The only rival work that are in any way comparable are also based on the pseudopotential approach. In particular the proximity of the elastic constants to the experimental values is very convincing evidence that the physics of MgO is being correctly modeled by these calculations. There can be little doubt that the pseudopotential approach of the CETEP codes can be used to successfully investigate

the properties of materials other than the semiconductors and covalent oxides that have thus far been the main focus of activity.

The results achieved in the work on magnesium oxide have been most satisfactory. The success in predicting the equilibrium properties discussed above enabled meaningful calculations to be made at high pressure. Where it is possible to compare these to reliable experimental data (for example with the pressure derivatives of the elastic constants) the agreement is, once more, excellent. The geophysical properties calculated have also been very encouraging. The seismic wave velocities match those measured by Duffy and Anderson (1989) within the observed range of pressures. Other results are consistent with the best of the empirical calculations that have been made before. These results have a great deal to offer to those making empirical computations as an independent way to fix some of the parameters in their high pressure calculations. The study of the charge density patterns of MgO illustrated very graphically the breathing of the electron cloud surrounding the oxygen ions. The reciprocal space distributions, in particular, are very convincing as they show the charge cloud unchanged by volume-conserving distortions whilst any change in the volume of the unit cell causes a similar change in the volume of the charge cloud. The cloud remains spherical at all times. This effect is now established as a very plausible explanation for the violation of the Cauchy condition in MgO.

The predictions made of the properties of the other earth-metal oxides were very disappointing in comparison to those for MgO. The initial equilibrium predictions were not within the customary limits of accuracy expected of LDA calculations. Although there is a paucity of reliable experimental work on the elastic constants leading to a fair degree of uncertainty as to their actual value, this is certainly not true of the lattice constants and the errors of between three and five percent are

not of the expected accuracy. The transferability of the metal pseudopotentials was investigated by changing the electronic configurations used in generation. This had the unfortunate effect of enabling almost any desired lattice parameter or bulk modulus to be obtained simply by varying the ionicity of the starting configuration. It was obviously inconvenient for a supposedly *ab initio* method to behave in this manner and the restoration of transferability was the next priority. This was achieved by the application of non-linear core corrections to the metal pseudopotentials. Even though this did not produce an improvement in the accuracy of the predictions I believe there can be little doubt that the core corrected values are correct LDA results. As discussed at the end of chapter 5 the factors influencing this behaviour must lie beyond the ability of LDA to simulate. Effects such as Van der Waal's forces are obvious candidates for this. Even though the physical properties of the oxides were not well reproduced it was still possible to obtain useful information about the electron structure through the charge density patterns. The weakening and eventual reversal of the Cauchy violation is mirrored in the gradual strengthening of the distortion apparent in the oxygen charge cloud. It is not possible to be as categorical as for MgO, but there does seem to be some evidence for a deformable ion effect adding to the breathing shell effect as an important influence to the elastic properties and the Cauchy violation.

REFERENCES

Abarenkov I V and Heine V, 1965, *Phil. Mag.*, **12**, 529.

Agnon A and Bukowinski M S T, 1990, *Geophys. Res. Lett.*, **17**, 1149.

Allan D C and Teter M P, 1987, *Phys. Rev. Lett.*, **60**, 1136.

Anderson O L and Andreatch P, 1966, *J. Am. Ceram. Soc.*, **49**, 404.

Ashcroft N W and Mermin N D, 1976, *Solid State Physics*, Saunders College Publishing, Philadelpia.

Au A Y and Weidner D J, 1986, *Phys. Chem. Miner.*, **13**, 360.

Austin J, Heine V and Sham L J, 1962, *Phys. Rev.*, **127**, 276.

Bachelet G B, Hamann D R and Schlüter M, 1982, *Phys. Rev.* B, **26**, 4199.

Bar-Yam Y and Pantelides S T, 1989, *Phys. Rev.* B, **39**, 3396.

Birch F, 1947, *Phys. Rev.*, **71**, 809.

Bird D M, Clarke L J, King-Smith R D, Payne M C, Štich I and Sutton A P, 1992, *Phys. Rev. Lett.*, **69**, 3785.

Bogardus E H, 1965, J. Appl. Phys., **36**, 2504.

Boyer L L, Mehl M J, Feldman J L, Hardy J R, Flocken J W and Fong C Y, 1985, *Phys. Rev. Lett.*, **54**, 1940.

Car R and Parrinello M, 1985, *Phys. Rev. Lett.*, **55**, 2471.

Carter W J, Marsh S P, Fritz J N and McQueen R G, 1971, in *Accurate Characterization of the High-Pressure Environment*, edited by Lloyd E C, Nat. Bur. Stand. Washington, D.C.

Causa M, Dovesi R, Pisani C and Roetti C, 1986, *Phys. Rev.* B, **33**, 1308.

Ceperley D M and Alder B J, 1980, *Phys. Rev. Lett.*, **45**, 566.

Chang K J and Cohen M L, 1984, *Phys. Rev.* B, **30**, 4774.

Chang Z P and Graham E K, 1977, *J. Phys. Chem. Solids*, **38**, 1355.

Chung D H, 1963, *Phil. Mag.*, **8**, 833.

Chelikowsky J R, King H E, Troullier N, Martins J L and Glinnemann J, 1990, *Phys. Rev. Lett.*, **65**, 3309.

Clarke L J, Štich I and Payne M C, 1992, *Comput. Phys. Commun.*, **72**, 14.

Cohen A J and Gordon R G, 1976, *Phys. Rev.* B, **14**, 4593.

Cohen M H and Heine V, 1961, *Phys. Rev.*, **122**, 1821.

Cohen M L and Bergstresser T, 1966, *Phys. Rev.*, **141**, 789.

Cohen M L and Heine V, 1970, *Solid St. Phys.*, **24**, 37.

Davies G F, 1981, *Phys. Chem. Miner.*, **7**, 246.

De Vita A, Gillan M J, Lin J S, Payne M C, Štich I and Clarke L J, 1992a, *Phys. Rev. Lett.*, **68**, 3319.

De Vita A, Gillan M J, Lin J S, Payne M C, Štich I and Clarke L J, 1992b, *Phys. Rev.* B, **46**, 12964.

Dragoo A L and Spain I L, 1977, *J. Phys. Chem. Solids*, **38**, 705.

Duffy T S and Anderson D L, 1989, *J. Geophys. Res.*, **94**, 1895.

Durand M A, 1936, *Phys. Rev.*, **50**, 449.

Dziewonski A M and Woodhouse J H, 1987, *Science*, **236**, 37.

Farid B and Needs R J, 1992, *Phys. Rev.* B, **45**, 1067.

Fowler P W, Knowles P J and Pyper N C, 1985, *Molec. Phys.*, **56**, 83.

Godby R W, Schlüter M and Sham L J, 1986, *Phys. Rev. Lett.*, **56**, 2415.

Gonze X, Käckell P and Schleffler M, 1990, *Phys. Rev.* B, **41**, 12264.
Hamann D R, Schlüter M and Chiang C, 1979, *Phys. Rev. Lett.*, **43**, 1494.
Hearmon, 1979, in *Landolt-Börnstein: Numerical Data and Functional Relationships in Science and Technology, Group III/11: Crystal and Solid State Physics*, Edited by K-H Hellwege, Springer-Verlag, Berlin.
Heine V, 1970, *Solid St. Phys.*, **24**, 1.
Heine V and Weaire D, 1970, *Solid St. Phys.*, **24**, 249.
Herring C, 1940, *Phys. Rev.*, **57**, 1169.
Hill R, 1952, *Proc. Phys. Soc. [Lond.]* A, **65**, 349.
Hohenberg P and Kohn W, 1964, *Phys. Rev.*, **136**, B864.
Hong H and Yuen D A, 1990, *J. Geophys. Res.*, **95**, 7055.
Ihm J, 1988, *Rep. Prog. Phys.*, **51**, 105.
Ihm J, Zunger A and Cohen M L, 1979, *J. Phys.* C, **12**, 4409.
Isaak D G, Anderson O L and Goto T, 1989, *Phys. Chem. Miner.*, **16**, 704.
Isaak D G, Cohen R E and Mehl M J, 1990, *J. Geophys. Res.*, **95**, 7055.
Jeanloz R and Ahrens T J, 1980, *Geophys. J. R. Astron. Soc.*, **62**, 505.
Johnston D L, Thrasher P H and Kearney R J, 1970, *J. Appl. Phys.*, **41**, 427.
Kerker G P, 1980, *J. Phys.* C, **13**, L189.
King-Smith R D, Payne M C and Lin J S, 1991, *Phys. Rev.* B, **44**, 13063.
Kirkpatrick S, Gelatt C D and Vecchi M P, 1983, *Science*, **220**, 671.
Kleinman L and Bylander D M, 1982, *Phys. Rev. Lett.*, **48**, 1425.
Kohn W and Sham L J, 1965, *Phys. Rev.*, **140**, A1133.
Lin J S, Qteish A, Payne M C and Heine V, 1993, *Phys. Rev.* B, **47**, 4174.
Liu L and Bassett W A, 1972, *J. Geophys. Res.*, **77**, 4934.
Louie S G, Fröyen S and Cohen M L, 1982, *Phys. Rev.* B, **26**, 1738.
Lundqvist S and March N H, 1983, *Theory Of The Inhomogeneous Electron Gas*, Plenum Press, New York.
Mackrodt W C, Harrison N M, Saunders V R, Allan N L, Towler M D, Apra E and Dovesi R, 1992, to be published.
Mao H H and Bell P M, 1979, *J. Geophys. Res.*, **84**, 4533.
Markland K and Mahmoud S A, 1971, *Phys. Scr.*, **3**, 75.
Masters G, Jordan T H, Silver P G and Gilbert F, 1982, *Nature*, **298**, 609.
McCammon C A, Brown T H and Meagher E P, 1991, *Phys. Chem. Miner.*, **17**, 622.
Mehl M J, Cohen R E and Krakauer H, 1988, *J. Geophys. Res.*, **93**, 8009.
Mehl M J, Hemley R J and Boyer L L, 1986, *Phys. Rev.* B, **33**, 8685.
Monkhorst H J and Pack J D, 1976, *Phys. Rev.* B, **13**, 5189.
Nye J F, 1985, *Physical Properties Of Crystals*, Clarendon Press, Oxford.
Pai S Y and Sivertson J M, 1976, *J. Phys. Chem. Solids*, **37**, 17.
Pandey R, Jaffe J E and Kunz A B, 1991, *Phys. Rev.* B, **43**, 9228.
Park K-O and Sivertson J M, 1975, *Phys. Letters* A, **55**, 62.
Parker S C and Wall A, 1991, *Geophys. Res. Lett.*, **18**, 2185.
Payne M C, Joannopoulos J D, Allan D C, Teter M P and Vanderbilt D H, 1986, *Phys. Rev. Lett.*, **56**, 2656.
Pendry J B, 1974, *Low Energy Electron Diffraction*, Academic Press, London.
Perdew J P and Zunger A, 1981, *Phys. Rev.* B, **23**, 5048.
Phillips C S G and Williams R J P, 1965, *Inorganic Chemistry*, Oxford University Press.

Phillips J C and Kleinman L, 1959, *Phys. Rev.*, **116**, 287.
Pyper N C, 1986, *Phil. Trans. Roy. Soc. London*, **A320**, 107.
Qteish A and Needs R J, 1991, *Phys. Rev.* B, **43**, 4229.
Ramchurn S K, Bird D M and Bullett D W, 1990, *J. Phys.: Condens. Matter*, **2**, 7435.
Rappe A M, Rabe K M, Kaxiras E and Joannopoulos J D, 1990, *Phys. Rev.* B, **41**, 1227.
Reuss A, 1929, *Z. angew. Math. Mech.*, **9**, 55.
Ricard Y, Fleitout L and Froidevaux C, 1984, *Ann. Geophys.*, **2**, 267.
Ricard Y, Vigny C and Froidevaux C, 1989, *J. Geophys. Res.*, **94**, 13739.
Richards M A and Hager B H, 1984, *J. Geophys. Res.*, **89**, 5987.
Schlüter M, Chelikowsky J R, Louie S G and Cohen M L, 1975, *Phys. Rev.* B, **12**, 4200.
Schröder U, 1966, *Solid State Commun.*, **4**, 347.
Singh R K and Sanyal S D, 1982, *Phys. Status Solidi* B, **113**, K23.
Slater J C and Kirkwood J G, 1931, *Phys. Rev.*, **37**, 682.
Son P R and Bartels R A, 1972, *J. Phys. Chem. Solids*, **33**, 819.
Spetzler H, 1970, *J. Geophys. Res.*, **75**, 2073.
Štich I, Payne M C, King-Smith R D, Lin J S and Clarke L J, 1992, *Phys. Rev. Lett.*, **68**, 1351.
Susse C, 1961, *J. Nat. Rech. Sci. Lab.*, **54**, 23.
Teter M P, Payne M C and Allen D C, 1989, *Phys. Rev.* B, **40**, 12255.
Thakur K P, 1980, *J. Phys. Chem. Solids*, **41**, 465.
Topp W C and Hopfield J J, 1973, *Phys. Rev.* B, **7**, 1295.
Troullier N and Martins J L, 1990, *Solid State Commun.*, **74**, 613.
Troullier N and Martins J L, 1991, *Phys. Rev.* B, **43**, 1993.
Vassiliou M S and Ahrens T J, 1981, *Geophys. Res. Lett.*, **8**, 729.
Vetter V H and Bartels R A, 1973, *J. Phys. Chem. Solids*, **34**, 1448.
Voigt W, 1928, *Lehrbuch der Kristallphysik*, Teubner, Leipzig.
Walker N J, Saunders G A and Schäl N, 1987, *J. Phys. Chem. Solids*, **48**, 91.
Watson R, 1958, *Phys. Rev.*, **111**, 1108.
Weidner D J and Price G D, 1988, *Phys. Chem. Miner.*, **16**, 42.
Xu Y N and Ching W Y, 1991, *Phys. Rev.* B, **43**, 4461.
Yamashita J and Asano S, 1970, *J. Phys. Soc. Jap.*, **28**, 1143.
Yamashita J and Asano S, 1983, *J. Phys. Soc. Jap.*, **52**, 3506.